
Theses and Dissertations

Spring 2016

Cross section measurement of simultaneously produced $\Upsilon(1S) + J/\Psi$ mesons and upgrade studies for the CMS detector

Kamuran Dilsiz
University of Iowa

Copyright 2016 Kamuran Dilsiz

This dissertation is available at Iowa Research Online: <http://ir.uiowa.edu/etd/3072>

Recommended Citation

Dilsiz, Kamuran. "Cross section measurement of simultaneously produced $\Upsilon(1S) + J/\Psi$ mesons and upgrade studies for the CMS detector." PhD (Doctor of Philosophy) thesis, University of Iowa, 2016.
<http://ir.uiowa.edu/etd/3072>.

Follow this and additional works at: <http://ir.uiowa.edu/etd>



Part of the [Physics Commons](#)

CROSS SECTION MEASUREMENT OF SIMULTANEOUSLY PRODUCED
 $\Upsilon(1S) + J/\psi$ MESONS AND UPGRADE STUDIES FOR THE CMS DETECTOR

by
Kamuran Dilsiz

A thesis submitted in partial fulfillment
of the requirements for the Doctor of
Philosophy degree in Physics
in the Graduate College of
The University of Iowa

May 2016

Thesis Supervisor: Assoc. Prof. Jane M. Nachtman

Copyright by
KAMURAN DILSIZ
2016
All Rights Reserved

Graduate College
The University of Iowa
Iowa City, Iowa

CERTIFICATE OF APPROVAL

PH.D. THESIS

This is to certify that the Ph.D. thesis of

Kamuran Dilsiz

has been approved by the Examining Committee
for the thesis requirement for the Doctor of Philosophy
degree in Physics at the May 2016 graduation.

Thesis Committee: _____
Jane M. Nachtman, Thesis Supervisor

Yasar Onel

Robert L. Merlino

Mary Hall Reno

Kai Yi

To my Father, Yusuf, and Family
For their love and support.

ACKNOWLEDGMENTS

I would like to start with my great appreciation to my supervisor, Prof. Jane Nachtman, for providing me many opportunities to work on this research and supporting me to continue my studies on the CMS experiment. I am deeply grateful for the opportunities that she provided me to continue my research at the Fermi National Accelerator Laboratory during the last two years of my Ph.D.

I would like to greatly thank to Dr. Kai Yi for his mentorship, kindness and support during my study of experimental physics analysis with the CMS collaboration. This work was possible thanks to his support and valuable ideas. I would like to also thank Prof. Yasar Onel for sharing his valuable ideas about the future of experimental High Energy physics and structure of the detectors. I am particularly grateful to my other committee members Prof. Robert L. Merlino and Prof. Mary Hall Reno.

My sincere thanks also goes to Dr. Leonard Spiegel, who provided me an opportunity to join upgrade studies of the CMS pixel detector. My special thanks are extended to my friends and collages: Emrah Tiras, Hasan Ogul, Maksat Haytmuradov and Roberto Rossin.

Last but not least, I wish to express my love and thankfulness to my parents and my brothers and sisters for their support and encouragement in each and every part of my life.

ABSTRACT

A measured cross section of simultaneously produced $Y(1S)$ and J/ψ mesons is performed using 20 fb^{-1} integrated luminosity in proton-proton collisions at $\sqrt{s} = 8 \text{ TeV}$ center of mass energy recorded by the CMS detector. Both mesons are fully reconstructed from their final states, $\mu^+\mu^-$. To extract the signal yield, an extended maximum likelihood fit is used on two (invariant mass of $Y(1S)$ and J/ψ) and three (invariant mass of $Y(1S)$ and J/ψ , $c\tau$) dimensional components. A two-dimensional extended likelihood fit is used for the signal yield of data and a three-dimensional extended likelihood fit is used to know the possibility of displaced J/ψ candidate events arising from a B meson decay. A data embedding method is used to correct the efficiency in the data. The cross section in the fiducial region, defined as $|y| < 2.0$, is determined to be $16.5 \pm 3.6(\text{stat}) \pm 2.6(\text{syst}) \text{ pb}$.

The Silicon Pixel detector plays an important role in identifying secondary vertices and tagging long-lived particles such as b-quarks [1]. Because the silicon pixel detector is close to the interaction point of the CMS detector, it is exposed to a very harsh radiation environment. The silicon sensors of the pixel detector need to be replaced from time to time because of radiation damage. The CMS Phase I upgrade aims to have a sensor design that has a similar or better radiation performance compared with the original construction. To check the quality of wafers to be used in the CMS detector, Sintef did IV (current & voltage) measurements on all sensors of the production wafers and CV (capacitance & voltage) measurement on one diode of each wafer. When we receive production wafers from Sintef, we re-measure a small percentage of the wafers.

Our IV results are very close to Sintef results, with only a 4% disagreement. CV measurements confirm the ~65 V full depletion voltage from the Sintef measurements.

In order to improve the physics measurements capabilities for the harsh radiation environments at Large Hadron Collider (LHC), radiation hard detectors are needed. Secondary Emission Method (SEM) is a technique to measure the energy of particles such as e, n, and p in extreme radiation environments. Secondary Emission Ionization Calorimetry is a new technique for high radiation conditions. We designed two different types of test boards to test Hamamatsu single anode R7761 and multi-anode R5900-00-M16 PMTs and compared average gain values for both SE and PMT modes. We found that both values (SE and PMT) were comparable, which means the test boards that were developed perform very well and they could be used at Fermilab Test Beam Facility or in the CERN H2 beam area for the detection of minimum ionizing and showering particles.

PUBLIC ABSTRACT

A measured cross section of simultaneously produced $Y(1S)$ and J/ψ mesons is performed using 20 fb^{-1} integrated luminosity in proton-proton collisions at $\sqrt{s} = 8 \text{ TeV}$ center of mass energy recorded by the CMS detector. Both mesons are fully reconstructed from their final states, $\mu^+\mu^-$. To extract the signal yield, an extended maximum likelihood fit is used on two (invariant mass of $Y(1S)$ and J/ψ) dimensional components. The cross section in the fiducial region, defined as $|y| < 2.0$, is determined to be $16.5 \pm 3.6(\text{stat}) \pm 2.6(\text{syst}) \text{ pb}$. The silicon pixel detector is close to the interaction point of the CMS detector, so it is exposed to a very harsh radiation environment. The silicon sensors of the pixel detector need to be replaced from time to time because of radiation damage. For the next interaction, a silicon sensor must resist an integrated luminosity of 300 fb^{-1} . The silicon wafers that were made by Sintef were tested to check the capability of the sensors to be used for Phase I upgrade. Due to increasing integrated luminosity at particle accelerators, radiation hard detectors are needed. Secondary Emission Ionization Calorimetry is a new technique for high radiation conditions. The purpose is to design an SE module from a conventional PMT mode for secondary emission ionization calorimetry.

TABLE OF CONTENTS

LIST OF TABLES	ix
LIST OF FIGURES	x
CHAPTER	
1. INTRODUCTION	1
2. A DESCRIPTION OF THE LARGE HADRON COLLIDER, THE CMS DETECTOR AND ITS SUB-DETECTORS	4
2.1 Large Hadron Collider (LHC)	4
2.2 Compact Muon Solenoid (CMS)	6
2.2.1 Electromagnetic Calorimeter	7
2.2.2 Hadronic Calorimeter	8
2.2.3 Muon System	9
2.2.4 Tracking Detectors	13
2.2.5 The CMS Data Acquisition System	15
3. THE STANDARD MODEL (SM) OF PARTICLE PHYSICS AND A BRIEF DESCRIPTION OF QUARKONIUM	17
3.1 The Standard Model (SM) of Particle Physics	17
3.2 A Brief Explanation of Quarkonium	18
4. DOUBLE QUARKONIA	23
4.1 Theoretical Predictions for Double Quarkonia States	23
4.2 Observation and Cross Section of Double J/ψ and Double $\Upsilon(1S)$ at CMS	25
5. $\Upsilon(1S) + J/\psi$ PRODUCTION AND CROSS SECTION MEASUREMENT	28
5.1 Introduction	28
5.1.1 RooFit	29
5.2 Analysis Strategy	30
5.3 Event Selection and Reconstruction	33
5.4 Acceptance and Efficiency	36
5.4.1 Muon Acceptance	36
5.4.2 $\Upsilon(1S)$ and J/ψ Acceptance	38
5.4.3 Event-by-Event Acceptance and Efficiency Corrections	39
5.5 Simultaneously Produced $\Upsilon(1S)$ and J/ψ Events at CMS	42
5.5.1 Maximum Likelihood Fit	46
5.6 Decay Length ($c\tau$) of J/ψ and Υ	59
5.7 Fit Validation	62
5.8 Systematic Uncertainties	64
5.9 Results	74
5.9.1 Cross Section Evaluation	74

6.	CMS FORWARD PIXEL PHASE I UPGRADE SENSOR STUDY	77
	6.1 The CMS Pixel detector.....	77
	6.2 Quality Control on First Production Sensor Wafers.....	82
	6.3 Results.....	110
7.	R&D STUDY FOR SECONDARY EMISSION IONIZATION CALORIMETRY	112
	7.1 Introduction to Secondary Emission Ionization Calorimetry	112
	7.2 Characterization of PMT and SE Modes.....	113
	7.3 Baseboard Operation	116
	7.4 Results.....	118
8.	CONCLUSION.....	123
	REFERENCES	125

LIST OF TABLES

Table

5.1	Datsets, run ranges, and corresponding luminosities.....	33
5.2	Possible pair combination of $Y(1S) + J/\psi$ events with four muons final state.....	33
5.3	Fit parameters and values for the background mass distribution for the high mass and low mass pairs.....	44
5.4	MC fit parameters of J/ψ	47
5.5	MC fit parameters of $Y(1S)$	48
5.6	MC fit parameters of $Y(2S)$	48
5.7	MC fit parameters of $Y(3S)$	49
5.8	The components and yield values for two-dimensional fit.....	52
5.9	The components and yield values for three-dimensional fit.....	58
5.10	The components and yield values for three-dimensional fit without four-muon vertex probability cut.....	59
5.11	Systematic uncertainty due to signal PDF shape.....	66
5.12	Polarization effect for different λ values	68
5.13	Signal yields of three-dimensional fit for simultaneously produced Y and J/ψ MC events. The J/ψ decay length is $450 \mu m$. Non-prompt signal yield was found with and without four-muon vertex probability cut	69
5.14	Total systematic uncertainty with quadratic sum of each component.....	70
6.1	Production batch wafers number that were shipped from Sintef.....	110
7.1	Mean and RMS gain values of R7761 PMTs in different modes.....	120
7.2	Mean and RMS gain values of R5900-00-M16 PMTs in different modes.....	122

LIST OF FIGURES

Figure	
2.1 LHC located on a 27 km circular tunnel.....	4
2.2 Four main detectors of the LHC	5
2.3 Schematic view of the CMS detector	6
2.4 A CMS Electromagnetic Calorimeter.....	7
2.5 One-quarter view of the CMS Hadronic Calorimeter and its subdetectors. The interaction region is in the lower left corner. The scale indicates the pseudorapidity.....	9
2.6 A view of the CMS detector; muon chambers are the outermost detector element.....	10
2.7 One-quarter schematic view of the CMS muon system	11
2.8 Section of a DT cell.....	11
2.9 Schematic view of CSC.....	12
2.10 Two parallel plates of RPCs	13
2.11 One-quarter view of the silicon strip subdetectors	14
2.12 CMS pixel detector	15
2.13 Schematic view of the CMS DAQ system (on the left). Two levels architecture for the triggers (on the right).....	16
3.1 First observation of sequential $\Upsilon(nS)$ candidates that was observed by the CMS collaboration a) Di-muon invariant mass distribution in PbPb data b) Di-muon invariant mass distribution in pp data.....	20
3.2 Dimuon invariant mass and projected decay length of prompt J/ψ in PbPb collisions at 2.76 TeV	21
3.3 Invariant mass distribution of J/ψ with 2.76 TeV center of mass energy. On the left is data from pp collision and on the right is data from the PbPb collision.....	22
4.1 Possible Feynman diagrams for heavy quarkonia events, SPS (on the left) and DPS (on the right).....	23
4.2 Four-dimensional fit for simultaneously produced two J/ψ mesons	26
5.1 Reconstructed single muon acceptance as a function of η^μ vs. p_T^μ . On the left muons from $\Upsilon(1S)$ decay and on the right muons from J/ψ decay	37

5.2	Single muon acceptance map. Muon acceptance was defined taking ratio of reconstructed muons to generated muons as a function of η vs. p_T	38
5.3	$Y(1S)$ and J/ψ acceptance. J/ψ acceptance as a function of $ y $ vs. p_T is on the left. $Y(1S)$ acceptance as a function of $ y $ vs. p_T is on the right	39
5.4	Event-by-event acceptance values were defined using a data embedding method assuming isotropic decay of $Y(1S)$ and J/ψ mesons	41
5.5	Average event-by-event efficiency in bins of a) four muon p_T b) lowest muon p_T c) pile-up defined here as the number of primary vertices reconstructed per event.....	42
5.6	Two-dimensional view of high mass and low mass pairs	43
5.7	The mass distribution for the high and low mass pairs in the four regions	45
5.8	Reconstructed mesons from MC simulation a) $Y(1S)$ b) J/ψ c) $Y(2S)$ d) $Y(3S)$ MC events.....	47
5.9	Extended two-dimensional likelihood fit of simultaneously produced $Y(1S)$ and J/ψ events. $Y(1S)$ candidate on the left and J/ψ candidate on the right. Bottom scales are pull distributions.....	51
5.10	Three-dimensional maximum likelihood fit of $Y(1S) + J/\psi + c\tau$. Top-left: $Y(1S)$ candidate. Top-right: J/ψ candidate. Bottom: Decay length of J/ψ ($c\tau$).....	56
5.11	Three-dimensional maximum likelihood fit without four-muon vertex probability cut. Top-left: $Y(1S)$ candidate. Top-right: J/ψ candidate. Bottom: Decay length of J/ψ ($c\tau$).....	57
5.12	Divided high mass (on the right) and low mass (on the left) pairs into three regions for a definition of the sidebands.....	60
5.13	$c\tau$ for high mass and low mass regions (entire region). Low mass $c\tau$ on the left and high mass $c\tau$ on the right.....	61
5.14	$c\tau$ for high mass and low mass central region. $c\tau$ for J/ψ region [3.0-3.2] on the left and for Y region [9.2-10.5] on the right.....	61
5.15	$c\tau$ for high mass and low mass sidebands. $c\tau$ for J/ψ sideband [3.2-3.4] on the left and for Y sideband [10.5-11.5] on the right.....	62
5.16	$c\tau$ for high mass and low mass sidebands. $c\tau$ for J/ψ sideband [2.8-3.0] on the left and for Y sideband [8.5-9.2] on the right.....	62
5.17	Results of Toy experiments for 10000 generated events.....	63
5.18	Two-dimensional maximum likelihood fit with Gaussian + Voigtian function. $Y(1S)$ (on the left) and J/ψ (on the right).....	65
5.19	Two-dimensional maximum likelihood fit with double crystal ball function with mean and sigma floating. $Y(1S)$ (on the left) and J/ψ (on the right)	65

5.20	Two-dimensional maximum likelihood fit with first order Chebyshev polynomial used on the background. $Y(1S)$ (on the left) and J/ψ (on the right)	66
5.21	Three-dimensional fit on simultaneously produced $Y(1S)$ and J/ψ MC events. Top-left: J/ψ invariant mass MC events. Top-right: $Y(1S)$ invariant mass MC events. Bottom: $c\tau$ of J/ψ when J/ψ decay length is zero and the four-muon vertex probability is greater than 5%.....	71
5.22	Three-dimensional fit on simultaneously produced $Y(1S)$ and J/ψ MC events. Top-left: J/ψ invariant mass MC events. Top-right: $Y(1S)$ invariant mass MC events. Bottom: $c\tau$ of J/ψ when J/ψ decay length is zero and no four-muon vertex probability cut.....	72
5.23	Three-dimensional fit on simultaneously produced $Y(1S)$ and J/ψ MC events. Top-left: J/ψ invariant mass MC events. Top-right: $Y(1S)$ invariant mass MC events. Bottom: $c\tau$ of J/ψ when J/ψ decay length is $450 \mu m$ and the four-muon vertex probability is greater than 5%.....	73
5.24	Three-dimensional fit on simultaneously produced $Y(1S)$ and J/ψ MC events. Top-left: J/ψ invariant mass MC events. Top-right: $Y(1S)$ invariant mass MC events. Bottom: $c\tau$ of J/ψ when J/ψ decay length is $450 \mu m$ and no four-muon vertex probability cut.....	74
6.1	An example of an n-doping (left) and p-doping (right).....	77
6.2	A sample for how a p-n junction semi-conductor works.....	79
6.3	A view of CMS detector, Silicon detector (tracker) in on the left, near the interaction point.....	81
6.4	A silicon pixel detector that shows sensors and readout chips	82
6.5	Sintef 2x8 sensor numbering (on the left). A picture of a wafer (on the right).....	83
6.6	Wafer test setup. Probe station to test silicon wafers and computer to view IV and CV curves and control the probe station.....	84
6.7	IV and CV connections to the probe station. (IV on the left and CV on the right)	85
6.8	Wafer 002, sensors that are good both for FNAL and Sintef	86
6.9	Wafers: 003, 006, 009, 010, sensors that are good both for FNAL and Sintef.....	87
6.10	Sensor that fails FNAL testing, but pass Sintef testing	88
6.11	CV measurement on wafer 009 (on the left). CV measurement with capacitance normalized to 1 after full depletion (on the right).....	88
6.12	CV measurement on one diode (left) and one sensor (right) for FNAL tests.....	89
6.13	Comparison of breakdown voltages of sensors for FNAL and Sintef results	90

6.14	IV curves of the good sensors for the shipment on May 29 th	91
6.15	Inconsistent measurement between FNAL and Sintef. Sensor 3 is bad for Sintef, but it is good for FNAL by our criteria	92
6.16	Breakdown voltage comparison for five production wafers from May 29 th shipment.....	93
6.17	CV curves of FNAL and Sintef, Sintef measures CV on one diode and FNAL measures CV on the first sensor of each wafer.....	94
6.18	IV curves for good sensors of production wafers 022, 106, 109, 120 and 139. B-type and C-type comparison was made between wafers 024 and 139.....	95
6.19	Sensors that are not consistent between FNAL and Sintef result. Sensors that are bad for FNAL but good for Sintef are on the left. Sensors that are good for FNAL but bad for Sintef are on the right.....	96
6.20	Breakdown voltage comparison of production wafers 022, 106,109, 129 and 139 for FNAL and Sintef.....	97
6.21	CV curves of the production wafers 106, 109, 120 and 139	98
6.22	IV curves for good sensors of production wafers 020, 112, 127, 136 and 143	100
6.23	IV curve for the sensors that are good for FNAL but bad for Sintef in third production batch	101
6.24	Breakdown voltage comparison for production wafers 020, 112, 127, 136 and 143	102
6.25	CV curves for production wafers 020, 112, 127, 136 and 143	103
6.26	Sensors that are good for FNAL and Sintef for the fourth production batch. Wafers 206, 214, 222, 227 and 231	105
6.27	Sensors that are good for Sintef but bad for FNAL.....	106
6.28	Sensors that are bad for both Sintef and FNAL. As can be seen, either they are not consistent with the first criteria ($I@100V < 1\mu A$) or they are not consistent with the second criteria ($I@150V < 2 * I@100V$)	107
6.29	Breakdown voltage comparison for production wafers 206, 214, 222, 227 and 231	108
6.30	CV curves of one diode for the Sintef data and one sensor for the FNAL data	109
7.1	Light-tight box located at the University of Iowa PMT test station	115
7.2	Schematic view of the board for Hamamatsu single anode R7761 PMT	117
7.3	Schematic view of the board for Hamamatsu multi anode R5900-00-M16 PMT	118

7.4	PMT and SE (cathode-first dynode shorted mode) gain distributions of Hamamatsu single anode R7761 PMTs at 1500, 1800, 2000 V	119
7.5	SE (cathode deactivated mode) gain distributions of Hamamatsu single anode R7761 PMTs at 1500, 1800, 2000 V	120
7.6	PMT and SE (cathode-first dynode shorted mode) gain distributions of Hamamatsu multi-anode R5900-00-M16 PMTs at 800, 1000, 1200 V.....	121

CHAPTER 1

INTRODUCTION

This Ph.D thesis consists of three studies: the observation and cross section measurement for $\Upsilon(1S) + J/\psi$ mesons, upgrade studies for the CMS pixel detector Phase I, and the characterization of photomultiplier tubes using a novel secondary ionization mode for secondary emission ionization calorimetry.

In the first part of this thesis, we performed a study for the observation of and cross section measurements for simultaneously produced $\Upsilon(1S)$ and J/ψ mesons using LHC pp collision data collected by the CMS detector. The motivation for this study is the observation of two J/ψ mesons found by NA3 collaboration in 1982 [2]. The University of Iowa High Energy physics group started to work on the observation and cross section measurement of double $\Upsilon(1S)$ events in 2014, and this is still an ongoing study. We measure the cross section of simultaneous production of $\Upsilon(1S)$ and J/ψ mesons with 20 fb⁻¹ integrated luminosity from proton-proton collisions at $\sqrt{s} = 8$ TeV recorded by the CMS detector. This study requires four muons in the final states because there are two muons in the final states of both $\Upsilon(1S)$ and J/ψ mesons. However, the total charge must be equal to zero in the final state because the two muons from the decays of $\Upsilon(1S)$ and J/ψ mesons have opposite charge. A two-dimensional extended maximum likelihood fit was used to measure the signal yield of simultaneously produced $\Upsilon(1S)$ and J/ψ mesons. However, it is possible to have displaced J/ψ events from B decay. To eliminate these displaced events, a 5% threshold was used on the four-muon vertex probability. To check for this possibility a three-dimensional maximum likelihood fit was used with the data

taking the decay length of the J/ψ candidate as the third dimension. To define an acceptance region and generate Monte Carlo samples for the muons, a Pythia6 MC generator particle gun is used. However, because the particle gun results can be biased, a data embedding method is used for acceptance and efficiency corrections. Using numerical values of average acceptance and efficiency corrections with two dimensional signal yield, the cross section of simultaneously produced $\Upsilon(1S)$ and J/ψ mesons were measured.

The second part of the thesis consists of upgrade studies of the CMS pixel detector. Due to significant radiation damage during the LHC operating, the pixel tracker needs to be replaced in the near future. For this reason, US has procured new pixel wafers from Sintef. We have tested and compared our results with Sintef results to check the quality control of these wafers. As part of the quality control process, we did IV (current-voltage) and CV (capacitance-voltage) measurements on a fraction of the Sintef wafers.

The third part of this thesis concerns the Secondary Emission (SE) method, which is a novel technique for measuring the energy of particles in extreme radiation environments. Increasing instantaneous luminosity at accelerators, such as the Large Hadron Collider, results in a high radiation environment in the area where detectors are located. For this reason, radiation-hard detectors need to be developed to allow physics measurement capabilities. The goal of this study is to develop a secondary emission ionization calorimeter using a conventional PMT mode. We report the technical design of secondary emission modules and provided the characterization of both SE and PMT modes. In a PMT mode, the current is measured between cathode and anode. However,

the cathode is deactivated or cathode and first dynode are short-circuited and the current is measured between first dynode and anode in an SE mode.

CHAPTER 2

A DESCRIPTION OF THE LARGE HADRON COLLIDER, THE CMS DETECTOR AND ITS SUB-DETECTORS

2.1 Large Hadron Collider (LHC)

The LHC, the most powerful particle physics accelerator in the world, is located at the European particle physics laboratory (CERN) in Geneva, Switzerland. It lies along the Swiss and French border. As can be seen in Figure 2.1, it is located in a circular tunnel that is 27 km long and 100 meters deep [3]. Scientists use this huge accelerator to collide beams of protons, which are accelerated to nearly the speed of light. By using the LHC physicists aim to reproduce the conditions just after the Big Bang and study the interaction of matter in its most fundamental state.



Figure 2.1: LHC located in a 27 km circular tunnel.

Since protons have positive charges, they can be directed by using an appropriate magnetic field. Thousands of particles are produced per interaction. Physicists can identify these particles by their response in detectors. As can be seen in Figure 2.2, the LHC has four main experiments and these experiments are CMS, ATLAS, ALICE, and LHC-B. Of these, CMS and ATLAS are the largest and general-purpose detectors. ALICE and LHC-B are specific experiments for heavy ion physics and B physics, respectively.

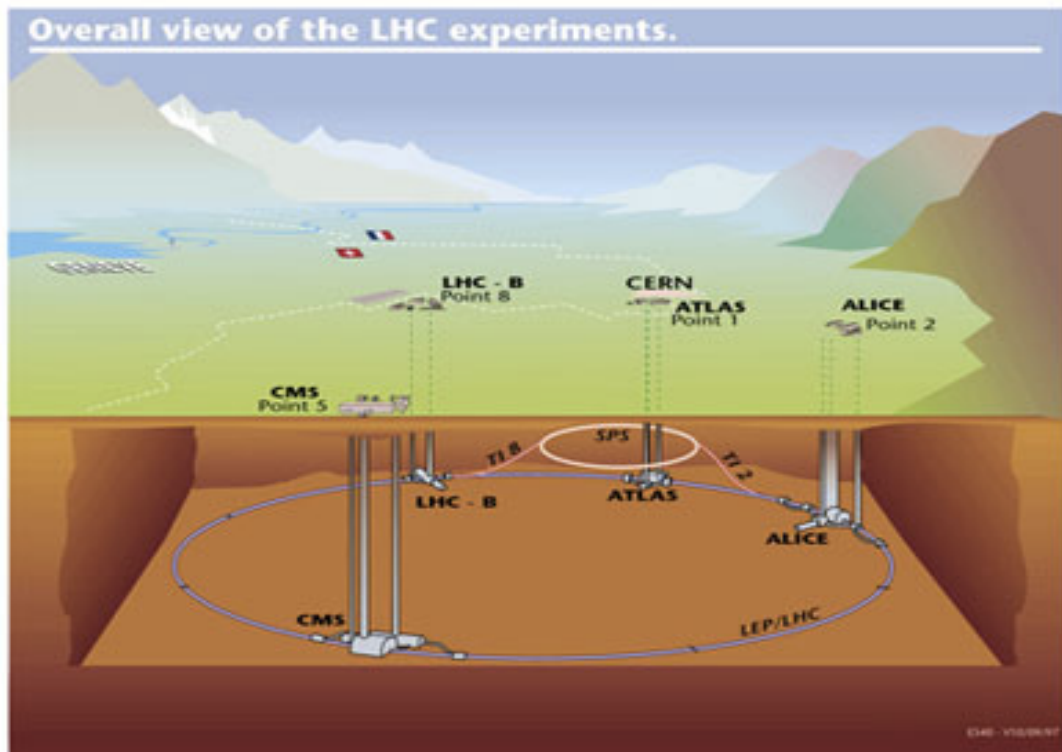


Figure 2.2: Four main detectors of the LHC.

2.2 Compact Muon Solenoid (CMS)

The CMS detector is a general purpose detector that is located on the LHC. It is 22 meters long, 15 meters in diameter, and weighs 12500 tons [4]. The CMS detector identifies particles and measures their energies and momenta. At the center of the CMS detector, there is an interaction point where proton-proton collisions occur. A 13 meter long and 5.9 meter wide superconducting solenoid produces a 3.8 T magnetic field which bends charged particles and allows measurements of their momentum in the tracking detectors [4]. The solenoid is surrounded by a return yoke in which muon chambers are interspersed [4]. In addition to the superconducting solenoid, as can be seen in Figure 2.3, the CMS detector has an electromagnetic calorimeter, a hadronic calorimeter, a muon system, and a silicon tracking system. Each subdetector covers a pseudorapidity range of $\eta = -\ln[\tan(\theta/2)]$ where θ is polar angle with respect to the beam direction [5].

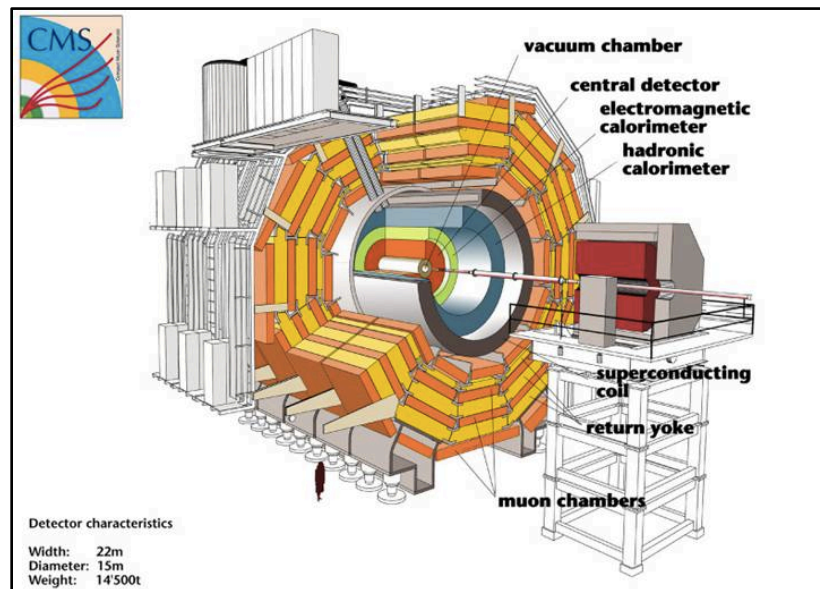


Figure 2.3: Schematic view of the CMS detector.

2.2.1 Electromagnetic Calorimeter

The CMS detector measures the energy from proton-proton collisions with its subdetectors. The electromagnetic calorimeter measures the energy of electrons and photons as they deposit energy in the electromagnetic calorimeter. The electromagnetic calorimeter has a pseudorapidity range $|\eta| < 3$ and includes barrel and endcap subdetectors [4]. Both subdetectors consist of crystals that are made from lead tungstate (PbWO_4). Lead tungstate was chosen as it can resist high levels of radiation and has a fast response time. The crystals measure the energy of the particles that interact inside the detector [4]. Avalanche photo-diodes are used to read out light in the barrel region of the electromagnetic calorimeter and vacuum phototriodes (VPT) are used for the endcap regions [6]. Figure 2.4 shows a schematic view of the CMS electromagnetic calorimeter.

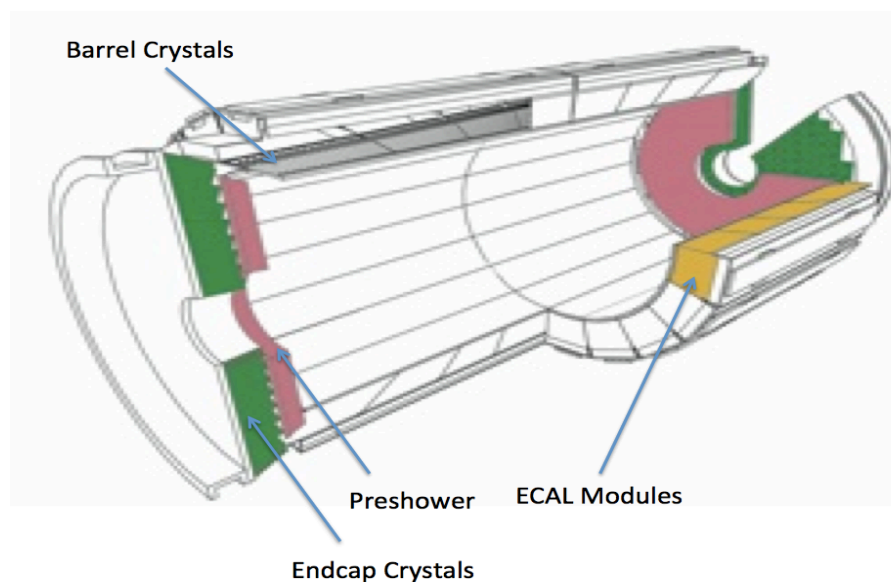


Figure 2.4: A CMS Electromagnetic Calorimeter [4].

2.2.2 Hadronic Calorimeter

The hadronic calorimeter is another subdetector of the CMS and it measures the energy of hadrons. The hadronic calorimeter detects both charged and neutral hadrons. After a proton-proton collision, new particles emerge from the decay of the particles that come out from the collision. The hadronic calorimeter has alternative absorber layers and scintillators to detect and capture hadrons. It is divided into four parts: hadronic forward (HF), hadronic barrel (HB), hadronic outer (HO), and hadronic endcap (HE).

HF is made up of quartz fibers embedded in a steel absorber that is 165 cm long [7]. There are two HFs, one on each side of the CMS detector, which are sensitive to forward particles coming from the collision at low angles with respect to the beam line. The distance of each HF to the interaction point is about 11.2 meters and the HF has a pseudorapidity range of $3.0 < |\eta| < 5.0$ [7,8].

HB and HE are sampling calorimeters and they are made of several layers of dense absorbers and plastic scintillator tiles [7]. The HB has innermost and outermost plates that are made of stainless steel; it has 32 towers and a pseudorapidity range of $|\eta| < 1.4$. The HE consists of 14 towers and has a pseudorapidity range of $1.3 < |\eta| < 3.0$ [8]. HO is usually called as HO-B and it's made of the same scintillator material as HB [7]. The HO is located outside the coil to absorb particles not stopped by HB [7]. The HO consists of 100 mm thick scintillators. It has a pseudorapidity range of $|\eta| < 1.26$ [8,9]. Figure 2.5 shows CMS Hadronic calorimeter and its subdetectors.

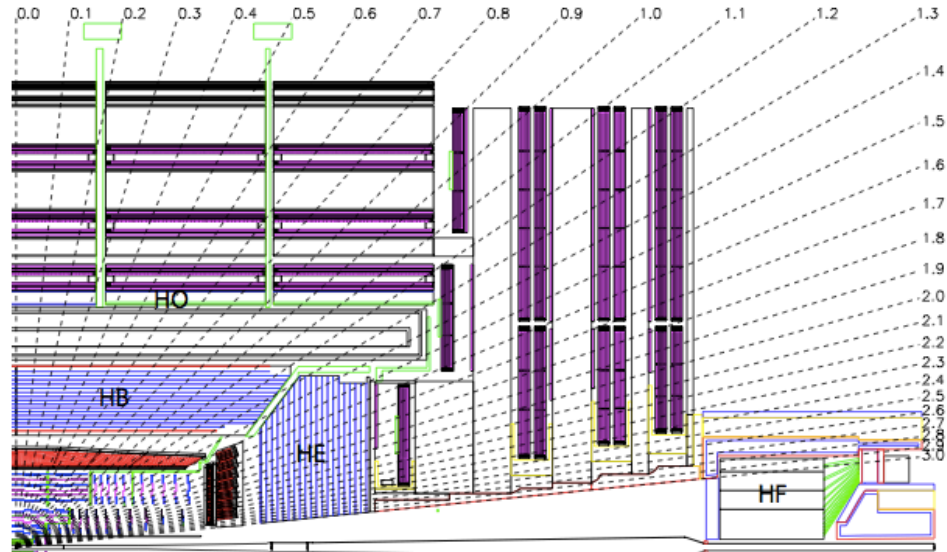


Figure 2.5: One-quarter view of the CMS Hadronic Calorimeter and its subdetectors. The interaction region is in the lower left corner. The scale indicates the pseudorapidity [7].

2.2.3 Muon System

Muons are charged leptons like electrons but more massive. They can be produced from the decay of many elementary particles such as the Higgs boson. Since they are heavier than electrons, they can go long distances through matter. One of the most important functions of the CMS detector is to detect muons. These are identified and measured by a combination of the tracker and the muon systems.

The muon system of the CMS is used for triggering on muons, identifying muons, and measuring the momentum of muons [5]. Muons must have a sufficient momentum to traverse the calorimeters and the muon system. As can be seen in Figure 2.6, the muon system is the outermost layer of the CMS detector and consists of three different types of chambers [6]. These are drift tube (DT) chambers, cathode strip chambers (CSCs), and resistive plate chambers (RPCs). The chambers provide inputs to the first level (L1)

trigger system of the CMS detector. In total, the muon system has 250 drift tubes (DTs), 540 cathode strip chambers (CSCs), and 610 resistive plate chambers (RPCs) [10].

As can be seen in Figure 2.7, DT chambers are in the barrel part of the detector, where muon rate is the smallest [4]. The CSCs are located in the endcaps that have a higher muon rate than the barrel part [4]. RPCs are located both in the barrel and endcap regions of the CMS detector.

DT chambers cover a pseudorapidity range of $|\eta| < 1.2$. DT chambers are divided into 12 ϕ -segments where ϕ is the azimuthal angle and these segments are from four stations that have different radii, interspersed between plates of the magnetic flux return yoke [5]. As can be seen in Figure 2.8, the DTs consist of drift cells. The size of the cells is $42 \times 13 \text{ mm}^2$, and a $50 \mu\text{m}$ diameter gold-plated stainless-steel anode wire, which operates at $\sim 3600 \text{ V}$, is located at the center of each cell [5].

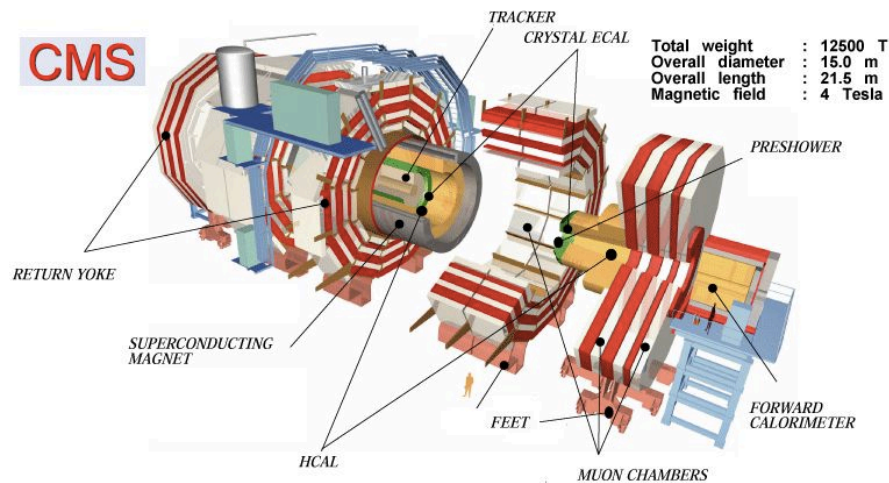


Figure 2.6: A view of the CMS detector; muon chambers are the outermost detector element.

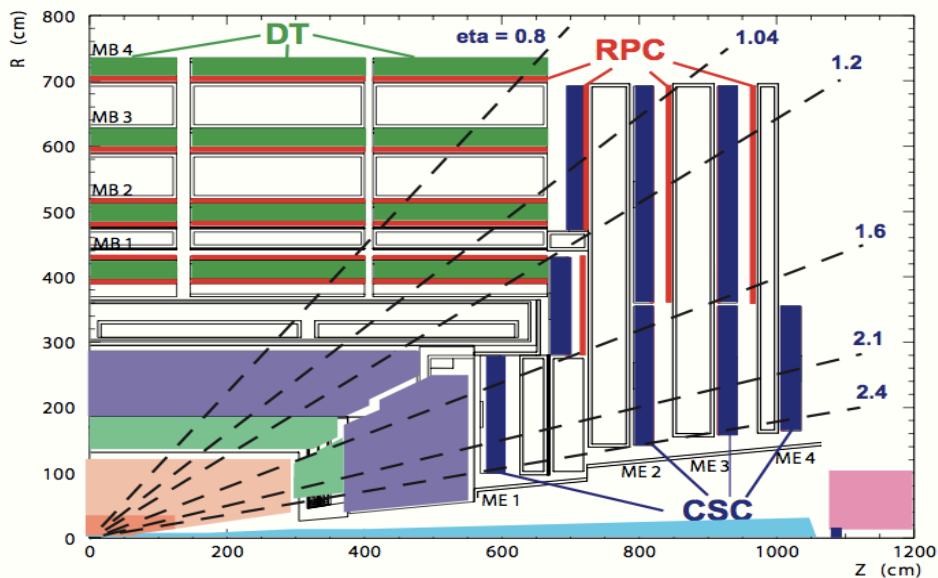


Figure 2.7: One-quarter schematic view of the CMS muon system [11].

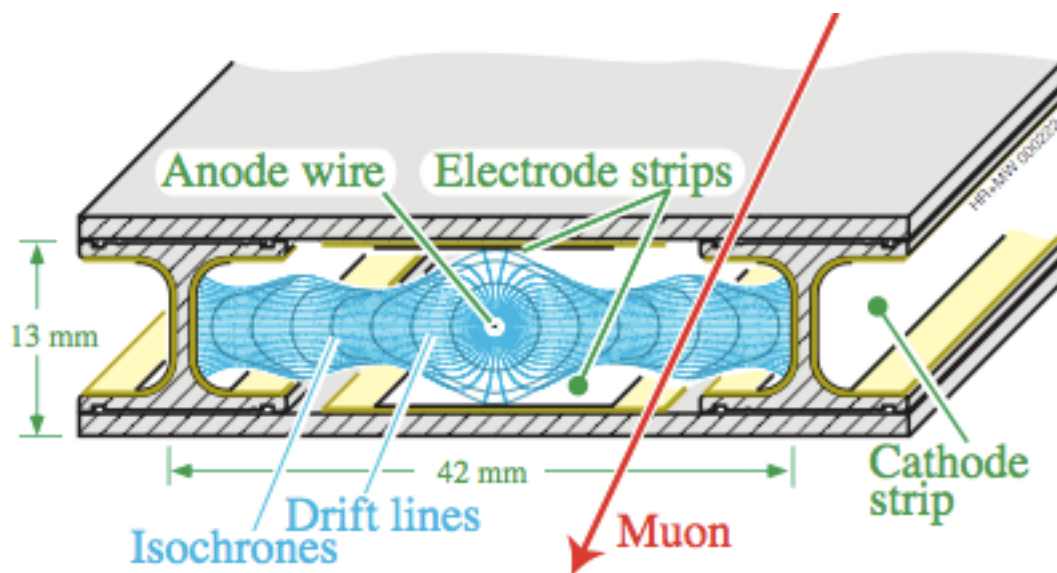


Figure 2.8: Section of a DT cell [8].

The CSCs are located in the endcap region of CMS, which has a higher muon rate and more background flux than the barrel part [4]. This region also has a strong and non-

uniform magnetic field [5]. CSCs have a fast response time and can tolerate the non-uniform magnetic field. Each CSC measures muon position in r - ϕ coordinates and collectively cover the pseudorapidity region $0.9 < |\eta| < 2.4$ [9]. CSCs have arrays of positively charged (anode) wires crossed with negatively charged cathode strips, all within a gas volume. Figure 2.9 shows a schematic view of the CSCs. The muons that pass through CSCs knock out electrons from the gas atoms and this leads to a large number of electrons at the anode wires. At the same time, positive ions move towards the cathode inducing charge pulses in the strips, which are at right angles to the wire direction.

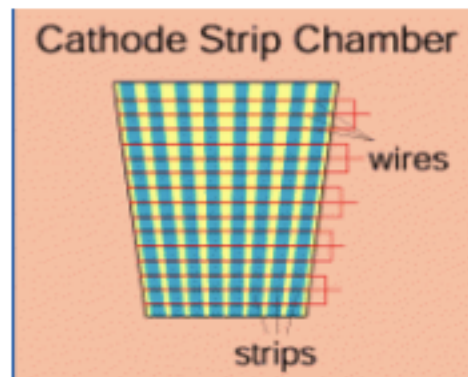


Figure 2.9: Schematic view of CSC [12].

The RPCs are located both in the barrel and endcap regions of the CMS detector. RPCs have a fast and independent trigger that has a looser p_T threshold over the pseudorapidity range $|\eta| < 1.6$ [5]. The RPC trigger system is parallel to the triggers of the DT chambers and CSCs. As can be seen in Figure 2.10, the RPCs consist of two parallel plates, which are made of a high resistivity plastic material. These plates, a positively

charged anode and a negatively charged cathode, are separated by a gas volume. When a muon passes through the RPCs, electrons are knocked out of gas atoms and these electrons hit other atoms causing an avalanche of electrons. Hits from the muon chambers are used as input to the L1 trigger and to measure muon momentum.

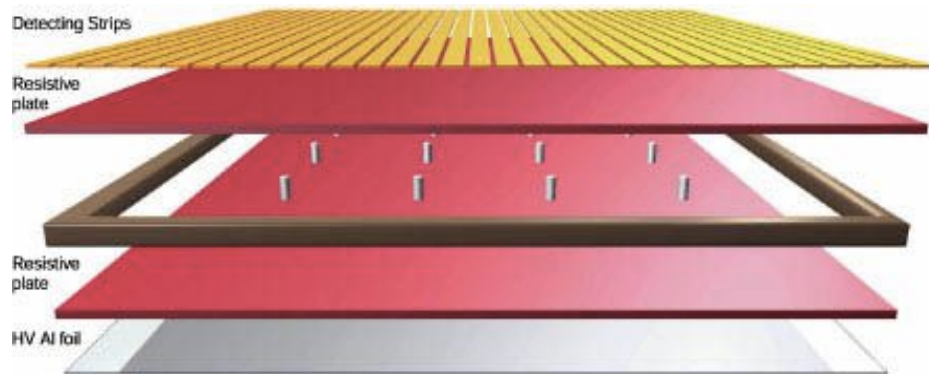


Figure 2.10: Two parallel plates of RPCs [13].

2.2.4 Tracking Detectors

A tracking detector is one of the CMS subdetectors. After a proton-proton collision at the interaction point, secondary particles enter the tracker. The tracker measures the curves of the charged particles as they are bent by the magnetic field [6]. The momentum and charge of the particle can be determined by their radius of curvature.

The tracker has a cylindrical shape that is 5.4 meters in length and 2.4 meters in diameter [6]. It is divided into two detectors which use silicon as the active medium. These are the pixel detector and the strip detector [4].

The silicon strip tracker is 5.4 meters in length and its diameter is 2.4 meters [4]. It has four subdetectors: the inner barrel (TIB), the inner disk (TID), the outer barrel

(TOB), and the tracker endcaps (TECs) [14]. The TIB has four layers with a cylindrical shape, the TOB has a six layers tracker, the TID has three disks on each sides and the TECs have nine disks [14]. Figure 2.11 shows the subdetectors of the silicon strip detector. The thick blue lines show double-sided modules and the thin red lines show single-sided modules.

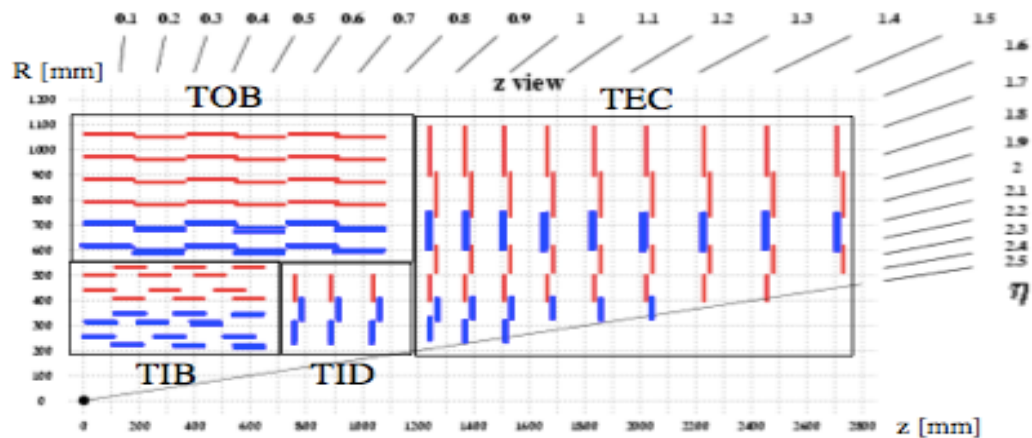


Figure 2.11: One-quarter view of the silicon strip subdetectors [14].

The pixel system of the CMS detector provides up to three hits per track, which enables identification of secondary vertices and tagging of long-lived particles such as b-quarks, which plays an important role in searching for Higgs or SUSY particles [1]. In addition, the pixel system plays a role in distinguishing long-lived particles from the large background of light quark and gluon jets [15].

Figure 2.12 shows a view of the CMS pixel detector. As can be seen in the figure, it consists of three barrels and two disks (on each side). The barrel layers are at $R = 4.4, 7.3, 10.2$ cm respectively. The layers consist of 48 million pixels, 11520 ROCs, and 1120

readout links [1]. Two disks are located on each side of the pixel detector. The distance between the sides and interaction point is about $\pm 34.5, \pm 46.5$ cm [4]. Both disks include 18 million pixels, 4320 ROCs, and 192 readout links [1]. A more detailed description of silicon detector is given in Chapter 6.

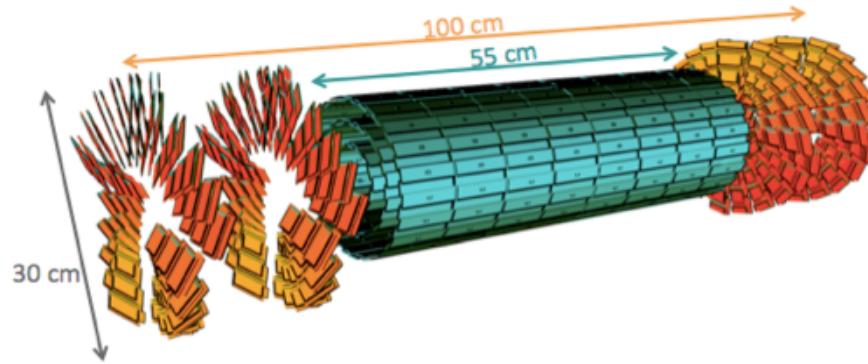


Figure 2.12: CMS pixel detector [1].

2.2.5 The CMS Data Acquisition System

After each bunch crossing at the LHC, the CMS detector starts to collect the data. About one million proton-proton interactions occur per second inside the CMS detector when it performs at its peak. However, data from these events cannot be read and analyzed easily because there may be low energy glancing collisions rather than energetic collisions and there is too much data to keep all of it. For this reason, the CMS detector has triggers that provide a way to choose interesting events and reduce the rate of data saved. Data processed by the triggers is collected and stored on computer disks to be analyzed.

The CMS detector has a two-level trigger system. The Level-1 (L1) trigger selects information from the muon detectors and the calorimeters and has an acceptance rate of

100 kHz [16]. The L1 trigger has about 500 readout systems [17]. The High Level Trigger (HLT) has a smaller acceptance rate and reduces the L1 rate to 1 kHz [17].

Figure 2.13 shows the architecture of the CMS Data Acquisition System (DAQ). Multiple units on the CMS DAQ store data in deep buffers and read out the front end electronics of the detector [17]. Using a switch network with external flow control, the buffers are delivered to the processors in the HLT farm [15]. The CMS DAQ also has a control and monitor system that is responsible for the configuration and control elements in the system.

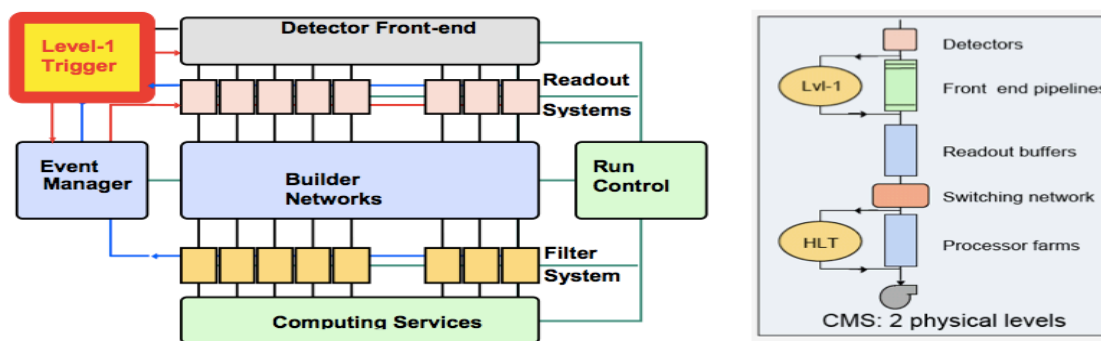


Figure 2.13: Schematic view of the CMS DAQ system (on the left). Two levels architecture for the triggers (on the right) [18].

CHAPTER 3

THE STANDARD MODEL (SM) OF PARTICLE PHYSICS AND A BRIEF DESCRIPTION OF QUARKONIUM

3.1 The Standard Model (SM) of Particle Physics

Elementary particle physics is often considered to have started with the discovery of the electron by J.J Thomson in 1897 and it has developed with the discovery of other particles such as photons, mesons, and neutrinos [19]. It is one of the most important fields for understanding the nature of the universe. Elementary particles and the forces that interact between them are fundamental to the universe. They are described with the standard model (SM) of the particle physics.

The SM [19] is the most successful and comprehensive theory of elementary particles and the forces interacting between these particles. It has been developed for many years and the discovery of new particles such as the top quark, tau neutrino and Higgs boson confirmed the reliability of the SM.

In the SM elementary particles consist of quarks, leptons and mediators [19]. There are six quarks. These are up(u), down(d), strange(s), charm(c), bottom(b), and top(t) quarks [19]. There are also anti-particles of these six quarks, which are called anti-quarks. Both quarks and anti-quarks have three colors, so there are 36 quarks in total [19]. Leptons are spin-half elementary particles that cannot be broken into smaller particles. There are 12 leptons in total (leptons and their anti-leptons). These are electrons, muons, taus and their neutrinos. Mediators are force carriers. These are gluons, W and Z bosons, and photons.

There are four fundamental forces in the universe. These are strong force, electromagnetic force, weak force and gravity. These fundamental forces are included in the SM except for gravity. Electromagnetic force provides the interaction between charged things. It has infinite range like gravity, but it is stronger than both gravity and the weak force. The exchange particle in electromagnetic force is the photon which has zero mass and travels at the speed of light. Weak force has a very short range. Its strength is lower than electromagnetic force but higher than gravity. The exchange particles for weak force are W^\pm and Z bosons. The strong force allows interaction between hadrons. This interaction is provided by exchange particles called gluons [19].

The SM claims that elementary particles have no mass in reality. This assertion has brought the question that could have not explained until Higgs boson, which provides mass to all the particles, was discovered in 2012 [20]. However, the discovery of Higgs boson did not solve the issue exactly because it was not obvious if this discovered boson was the one that claimed by the SM model or the boson claimed by other models. In order to solve this issue, the CMS and ATLAS collaborations measured the properties of this boson. Both collaborations reported that the discovered Higgs boson is the SM Higgs boson [21]. However, there are still questions that the SM cannot explain, such as why there are not as many anti-particles as particles in the universe? It also cannot explain Dark Matter [20].

3.2 A Brief Explanation of Quarkonium

Quarkonium, the bound state of a quark and its anti-quark, has been considered in investigations of new phenomena in particle physics. Both Y and J/ψ mesons are

examples of quarkonia since both can be produced from one quark and one anti-quark as shown below:

$$b\bar{b} \rightarrow Y \text{ (bottomonium)}, \quad c\bar{c} \rightarrow J/\psi \text{ (charmonium)}$$

The CMS collaboration made a search for three Y states (1S, 2S and 3S) in pp and PbPb collisions [22]. The first observation of sequential Y suppression in PbPb and pp datasets was reported using integrated luminosities of $150 \mu\text{b}^{-1}$ and 230nb^{-1} , respectively, in 2011 [23]. Y states can be identified by their dimuon decays and events can be selected with a trigger requiring two muon candidates in the muon detectors. Then, using an extended un-binned maximum likelihood fit on the invariant mass spectrum of muons, $Y(nS)$ yields can be measured.

Figure 3.1 shows the dimuon invariant mass distributions for $Y(nS)$ candidates that were observed by the CMS detector in 2011 [23]. An extended un-binned maximum likelihood fit is used on dimuon invariant mass distributions requiring the p_T of each single muon greater than $4 \text{ GeV}/c$. The solid curves show signal + background and dashed curves show only background. A Crystal Ball function is used to fit the signal and a second order polynomial is used to fit the background [23]. As can be seen, the $Y(1S)$ candidate is at $x = 9.46 \text{ GeV}/c^2$, $Y(2S)$ is at $x = 10.05 \text{ GeV}/c^2$ and $Y(3S)$ is at $x = 10.4 \text{ GeV}/c^2$. For the PbPb data $Y(3S)$ candidate does not have a clear peak, but this peak is clear in pp data as shown in Figure 3.1 (b).

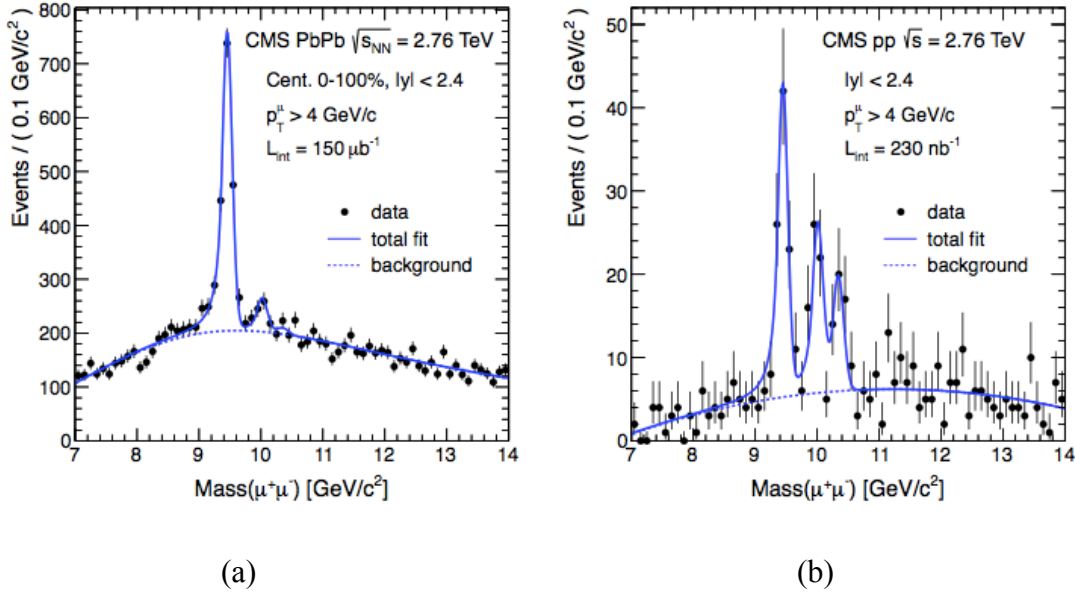


Figure 3.1: First observation of sequential $Y(nS)$ candidates that was observed by the CMS collaboration a) Di-muon invariant mass distribution in PbPb data b) Di-muon invariant mass distribution in pp data [23].

The charmonium is the bound state of a charm quark and its anti-quark. J/ψ , $\psi(2S)$ and ψ' are examples of charmonia. The J/ψ meson has a rest mass of $3.0969 \text{ GeV}/c^2$. It was discovered by the Stanford Linear Accelerator Center and Brookhaven National Laboratory in 1974 [24]. The CMS collaboration has studied charmonium states in pp and PbPb collisions. The contribution of non-prompt J/ψ from B meson decay to J/ψ cross section is not negligible in the LHC experiments. The CMS experiment separates non-prompt J/ψ from prompt J/ψ both in pp collisions, which have 7-8 TeV energy, and PbPb collisions, which have 2.76 TeV energy [25].

Figure 3.2 shows simultaneously fitted J/ψ invariant mass with the proper decay length. This data sample was collected by the CMS detector with an energy of 2.76 TeV PbPb collision using $7 \mu\text{b}^{-1}$ and $150 \mu\text{b}^{-1}$ integrated luminosity from 2010 and 2011 [26].

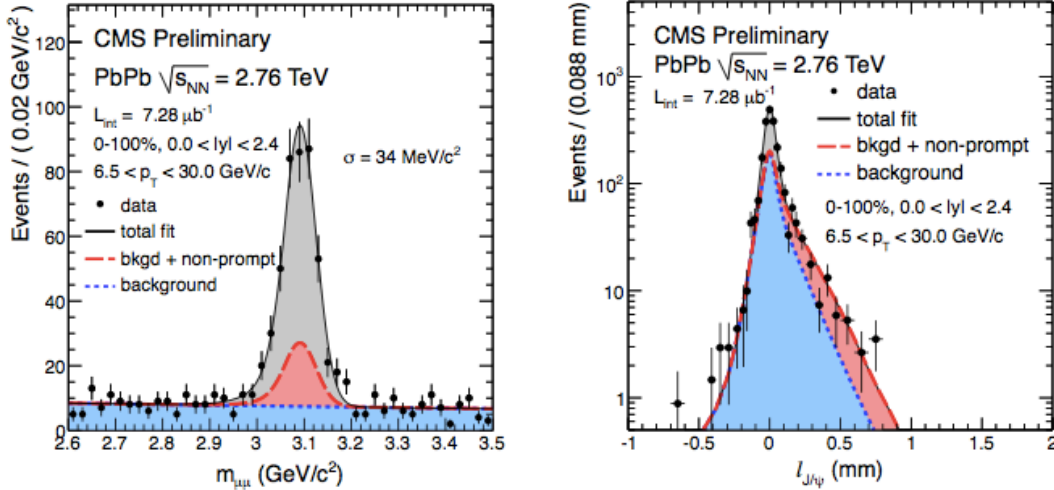


Figure 3.2: Dimuon invariant mass and projected decay length of prompt J/ψ in PbPb collisions at 2.76 TeV [26].

A two-dimensional unbinned maximum likelihood fit to the invariant mass of the prompt J/ψ is shown in Figure 3.2. Here, the black circles show the data and the dotted blue line shows the background which is from different contributions. The dashed red lines show the contribution from the non-prompt J/ψ , and the solid black line is the total fit (total background + signal) [26]. The signal model is fitted with a Crystal Ball function and an exponential function is used to fit the background [27]. The proper decay length [25] is used to distinguish the prompt J/ψ candidate from the non-prompt J/ψ candidate. The decay length is defined as:

$$\ell_{J/\psi} = L_{xy} \frac{m_{J/\psi}}{p_T} \quad (1)$$

$$L_{xy} = \frac{\tilde{u}^T \sigma^{-1} \tilde{x}}{\tilde{u}^T \sigma^{-1} \tilde{u}} \quad (2)$$

where:

$\ell_{J/\psi}$: Proper decay length of J/ψ .

L_{xy} : Proper transverse decay length in the laboratory rest frame.

\vec{x} : Vector both in dimuon vertex and collision vertex.

\check{u} : Unit vector of the J/ψ p_T .

σ : Sum of the primary and secondary vertex covariance matrices.

The J/ψ meson is the ground state of charmonium production and the $\psi(2S)$ is excited state of charmonium production. The CMS collaboration measured the invariant mass of $\mu^+\mu^-$ pairs in pp and 0-20% center PbPb collisions as show in Figure 3.3. The J/ψ invariant mass is about $3.09 \text{ GeV}/c^2$ and the $\psi(2S)$ invariant mass is about $3.68 \text{ GeV}/c^2$. In this figure, the signal yield is defined with one Gaussian and one Crystall Ball function and the background is defined by Chebychev polynomials [28].

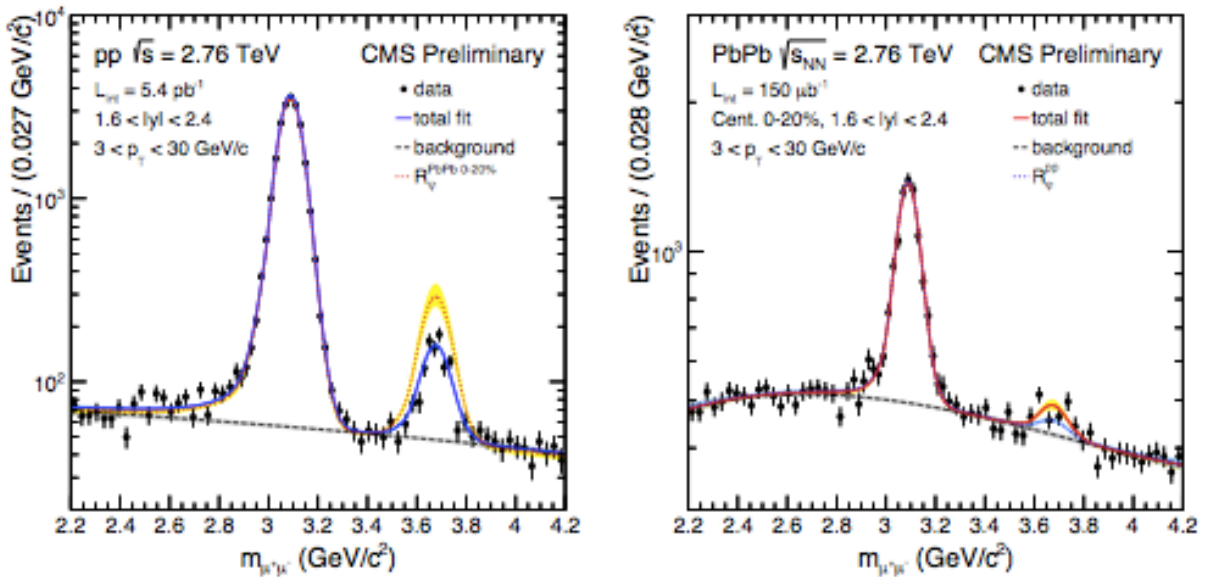


Figure 3.3: Invariant mass distribution of J/ψ with 2.76 TeV center of mass energy. On the left is data from pp collision and on the right is data from the PbPb collision [28].

CHAPTER 4

DOUBLE QUARKONIA

4.1 Theoretical Predictions for Double Quarkonia States

Double Parton Scattering (DPS) and Single Parton Scattering (SPS) are two possible mechanisms for double quarkonia production. In a pp collision, SPS is defined as the interaction of one parton with another parton and DPS is defined as the interaction of two partons with other two partons [29]. In general, these two mechanisms have been used for cross section predictions. Figure 4.1 shows possible Feynman diagrams for DPS and SPS mechanisms.

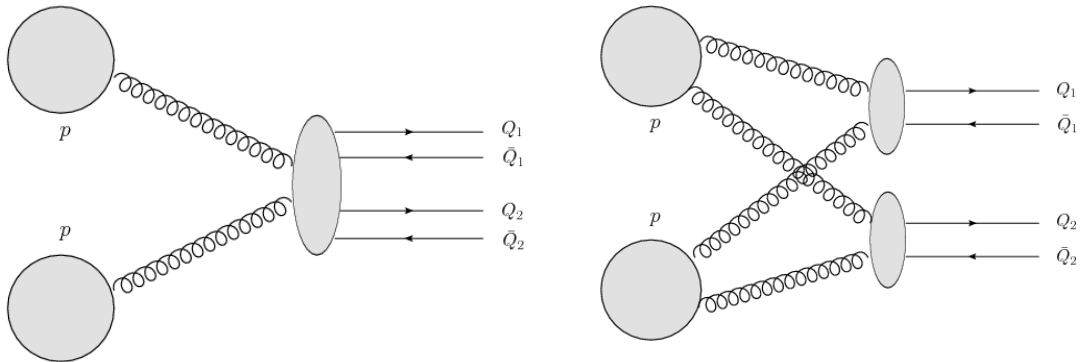


Figure 4.1: Possible Feynman diagrams for heavy quarkonia events, SPS (on the left) and DPS (on the right) [30].

When two hard partonic processes occur in hadron collision, we can define the DPS model for these two hadrons as the product of two single hadrons with SPS cross

sections normalized by an effective cross section as shown below [31].

$$\sigma_{DPS}^{xy} = \frac{m}{2} \frac{\sigma_{SPS}^x \sigma_{SPS}^y}{\sigma_{eff}} \quad (3)$$

where x and y are two particles in the process and the non-single diffraction (NSD) $\sigma_{eff} = 14.5$ mb for the CDF and D0 experiments. However, $\sigma_{eff} = 51$ mb at LHC. This is higher than the CDF and D0 NSD values [31]. One study of double parton scattering as a source of quarkonia pairs [31] showed the cross section results for $Y(1S) + J/\psi$ at 7 TeV in the LHCb detector.

$$\sigma_{DPS}^{Y(1S)+J/\psi} = 75 \text{ pb} \quad (4)$$

$$\sigma_{SPS}^{Y(1S)+J/\psi} = 2 \text{ pb} \quad (5)$$

In addition to $Y(1S) + J/\psi$, the study included cross section results for double J/ψ and double Y productions. The SPS and DPS results for these three quarkonia events are related each other as shown below:

$$\sigma_{SPS}^{J/\psi+J/\psi} = 4 \text{ nb}; \sigma_{DPS}^{J/\psi+J/\psi} = 2 \text{ nb} \quad (6)$$

$$\sigma_{SPS}^{Y(1S)+Y(1S)} = 8.7 \text{ pb}; \sigma_{DPS}^{Y(1S)+Y(1S)} = 0.4 \text{ pb} \quad (7)$$

$$\sigma_{SPS}^{Y(1S)+J/\psi} < \sigma_{SPS}^{Y(1S)+Y(1S)} < \sigma_{SPS}^{J/\psi+J/\psi} \quad (8)$$

$$\sigma_{DPS}^{Y(1S)+Y(1S)} < \sigma_{DPS}^{Y(1S)+J/\psi} < \sigma_{DPS}^{J/\psi+J/\psi} \quad (9)$$

Another theoretical prediction [32] for $Y(1S) + J/\psi$ showed that $\sigma_{DPS}^{Y(1S)+J/\psi} = 12.5$ pb at 8 TeV in the LHCb. In the absence of available calculations specific to CMS, we will rely on the LHCb calculations and the above relationships to attempt to understand $Y(1S) + J/\psi$ at CMS.

4.2 Observation and Cross Section of Double J/ψ and Double $Y(1S)$ at CMS

Due to high flux of incoming partons at LHC, there is a high probability for having more than one parton in a pp bunch crossing [33]. Since it is hard to address multi-parton scattering contributions, QCD predictions and experimental studies are needed [34]. The double J/ψ study concerns two J/ψ mesons originating from a common vertex and provides general insight about particle production during the pp collision at LHC [35].

The cross section of two simultaneously-produced J/ψ mesons was measured by the CMS collaboration with pp collisions at 7 TeV center-of-mass energy in 2011 [35]. This study motivates us to study $Y(1S) + J/\psi$ production and attempt to measure the cross section. In this study, the main focus is the invariant mass of two muons from the decay of J/ψ mesons. An extended maximum likelihood fit is used on the invariant mass of the oppositely charged muons that results from J/ψ decay. Since there is a possibility that J/ψ events come from B meson decay, the decay length of the J/ψ and significance of separation between the two J/ψ candidates are also important parts of this study to eliminate the background from non-prompt J/ψ candidates.

Figure 4.2 demonstrates a four dimensional maximum likelihood fit for two simultaneously produced J/ψ mesons. A double Gaussian function was used to define signal shape and a 3rd order Chebyshev polynomial was used to define purely combinatorial components. For the decay length of J/ψ , a double Gaussian function was used for prompt candidate and an exponential function convolved with a single Gaussian function was used for non-prompt candidate [35]. The significance of distance between two J/ψ candidates was defined with a single Gaussian function convolved with an

exponential function for the prompt and non-prompt components. Using an extended maximum likelihood fit, a signal yield of 446 ± 23 events was found and the total cross section was calculated as $\sigma = [1.49 \pm 0.07(stat) \pm 0.13(syst)]$ nb [33]. The differential cross section in bins of $|\Delta y|$ was calculated and the cross section was found to be sensitive to the DPS contribution from prompt double J/ψ production [35].

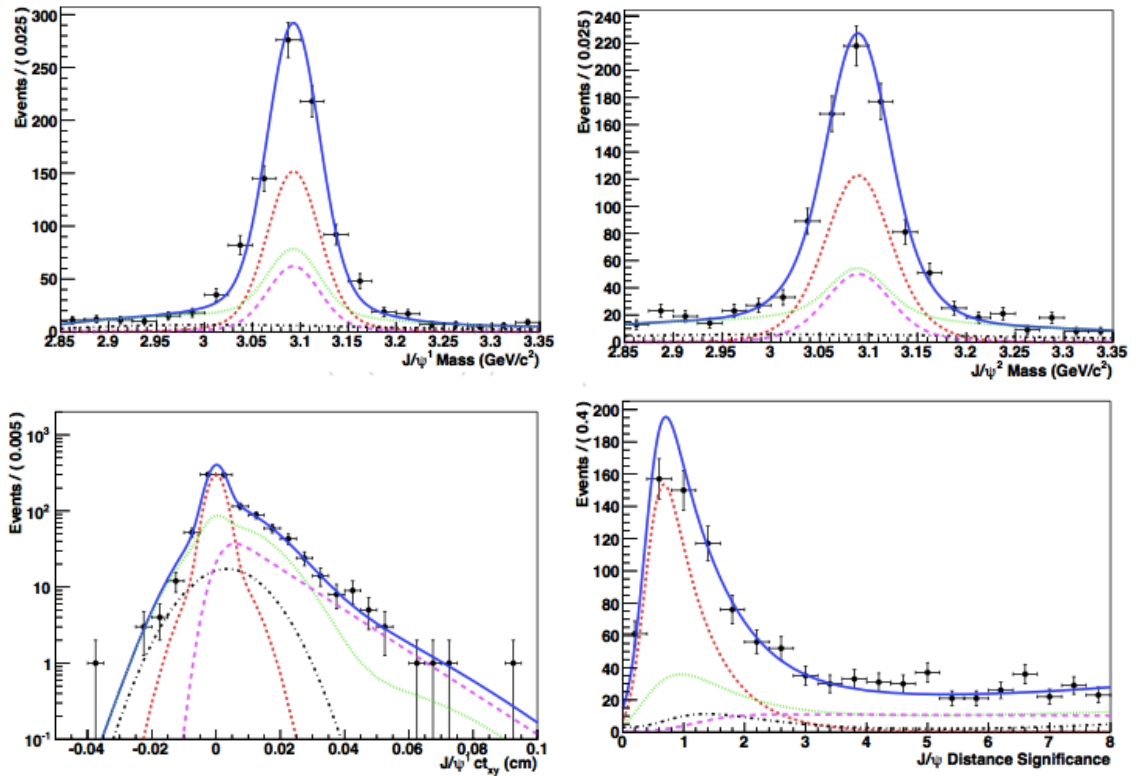


Figure 4.2: Four-dimensional fit for simultaneously produced two J/ψ mesons [35].

Another interesting study that motivates us to study $Y(1S) + J/\psi$ production and cross section measurement is the observation and cross section measurement of double $Y(1S)$ production. This study is being performed by the University of Iowa High Energy

Physics group and is an ongoing project. The goal of this study is to observe and measure the cross section of two simultaneously produced $\Upsilon(1S)$ mesons.

Establishing the signal and measuring the cross section of double quarkonia production may give insight into the SPS and DPS contributions and contribute to our understanding of QCD. These measurements also have value as precursors to searches for new states in the dimuon pair mass spectrum; proving our ability to accurately reconstruct these predicted states gives confidence in our ability to find something new.

CHAPTER 5

$Y(1S) + J/\psi$ PRODUCTION AND CROSS SECTION MEASUREMENT

5.1 Introduction

The first observation of double quarkonia production was at the NA3 experiment, with the observation of two J/ψ mesons in 1982 [2]. Subsequently, this observation was confirmed by the CMS [36] and ATLAS [37] collaborations. $Y(1S) + J/\psi$ production is a double quarkonia process because it consists of $(b\bar{b} \rightarrow Y)$ and $(c\bar{c} \rightarrow J/\psi)$.

In general, the model-dependent studies have assumed SPS and DPS models, which are two possible mechanisms for double quarkonia production, in order to define a specific region for the cross section measurement. Instead of using SPS and DPS, we used a data embedding method both to correct the measurement for efficiency and to minimize the model dependence of the cross section.

In this study, we used a particle gun to produce Monte Carlo simulation samples for Y and J/ψ mesons. These Monte Carlo samples are used to fix the shape of the dimuon invariant mass that is used for calculation of the cross section. An extended maximum likelihood fit was used to measure the signal yield based on two event variables, the mass of the J/ψ and $Y(1S)$ candidates. A third variable, the decay length of the J/ψ mesons, was used to ensure that the possibility of selecting displaced J/ψ events was minimized.

5.1.1 RooFit

In order to handle the large quantities of data collected by LHC detectors, a scientific software framework called root [38] was developed to be used for statistical analysis and data storage. This program was written based on C++ and python and is used within CMSSW, the software framework for the CMS detector [38].

In this analysis, we used RooFit [37] which is a software library of root and a particle physics data analysis tool. It is used to model expected distributions of events in physics analysis [39]. Using RooFit, we performed un-binned likelihood fits to generated plots and Monte Carlo samples. To define a model, RooFit uses mathematical distributions such as Gaussian, Crystal Ball, Voigtian, etc as probability density functions (pdfs) [39].

The Gaussian model [40] is a continuous function that can be used for very large numbers of events, and is commonly used in both the natural and social sciences. The Crystal Ball model is a probability density function that is commonly used to model various lossy processes in High Energy Collider Physics [41]. It is the combination of a Gaussian function with a power-law tail on each end of the distribution. A voigtian function is a continuous probability density function consisting of a Gaussian function convolved with a Breight-Wigner function. Mathematical descriptions for a Gaussian (10) [40], Crystal Ball (11) [41] and Breight-Wigner (12) [40] functions are given below:

$$f_g(x) = \frac{1}{\sqrt{2\pi\sigma^2}} e^{-\frac{(x-a)^2}{2\sigma^2}} \quad (10)$$

where α and σ represent the mean and standard deviation respectively.

$$f(x, \alpha, n, \bar{x}, \sigma) = e^{-\frac{1}{2}\left(\frac{x-\bar{x}}{\sigma}\right)^2} \text{ when } \frac{x-\bar{x}}{\sigma} > -\alpha$$

$$= \left(\frac{n}{|\alpha|}\right)^n e^{-\frac{|\alpha|^2}{2}} \left(\frac{n}{|\alpha|} - |\alpha| - \frac{x-\bar{x}}{\sigma}\right)^{-n} \text{ when } \frac{x-\bar{x}}{\sigma} < -\alpha \quad (11)$$

where \bar{x} and σ represent the mean and standard deviation of the Gaussian core, n is the exponent of the tail and $-\alpha$ is the abscissa at which the Gaussian core and the tail are joined.

$$f(E) = \frac{\Gamma/\pi}{(E-M)^2 + \Gamma^2} \quad (12)$$

where M is the mean and Γ is proportional to the width of the distribution.

In this study, a Crystal Ball function was used to define the signal shape and a Voigtian + Gaussian function was used to measure the systematical uncertainty due to the signal shape. A second order chebyshev polynomial was used to define the background shape for $Y + \mu^+\mu^-$ and $J/\psi + \mu^+\mu^-$ pairs. A generic pdf was used to define the shape of background for non-resonant $\mu^+\mu^- + \mu^+\mu^-$ pairs.

5.2 Analysis Strategy

In this analysis, we observed simultaneously produced $Y(1S)$ and J/ψ mesons and measured the total production cross section using data recorded by the CMS detector at $\sqrt{s} = 8$ TeV during 2012. Two different triggers were used to filter the data and select the expected events from the large CMS dataset. These triggers are generally used for muon physics analysis labeled `HLT_Dimuon_JPsi_Muon_v*` and `HLT_Dimuon_Upsilon_Muon_v*` in CMS. The detailed description for the triggers are given in Section 5.3.

While selecting events, we require four muons with zero total charge because both $Y(1S)$ and J/ψ mesons have two muons with opposite charges in their final states.

Backgrounds in our analysis come from accidental combinations of $\mu^+\mu^-$ pairs, Drell_Yan events which pass the trigger requirements and offline selection cuts, and J/ψ candidates from B meson decays. In the SM, there is no displaced particle that decays to Y, so the contribution of non-prompt Y mesons candidates is negligible. However, non-prompt J/ψ meson background is found in the dimuon data, arising from B meson decays.

In order to quantify background, we used two and three-dimensional fits to the dimuon invariant masses for the candidate $Y(1S)$ and J/ψ mesons. The goal for the two dimensional fit is to look at the simultaneously-produced $Y(1S)$ and J/ψ candidates and measure the signal and background contributions. We defined the two-dimensional fit with eight different components. These were $Y(1S)$ and J/ψ signal candidates and non-resonant pairs in the $Y(nS)$ and J/ψ mass regions. In such a fit, the component that consists of $Y(1S)$ and J/ψ candidates together becomes the signal component and the rest becomes the background. The goal of the three-dimensional fit is to ensure that there are no displaced J/ψ events from B decay; the decay length of J/ψ is the third dimension.

To correct the muon reconstruction efficiencies, we used a data embedding method to minimize the model dependence of the cross section determination. MC samples were produced using a Pythia6 MC generator (particle gun). After simultaneously produced $Y(1S)$ and J/ψ mesons were observed, we calculated the production cross section of these two mesons with the following formula:

$$\sigma(pp \rightarrow Y(1S) + J/\psi + X) = \frac{N_{Y(1S)+J/\psi}}{\epsilon_i a_i \cdot BF(Y(1S) \rightarrow \mu^+ \mu^-) \cdot BF(J/\psi \rightarrow \mu^+ \mu^-) \cdot L} \quad (13)$$

where:

- $N_{Y(1S)+J/\psi}$: Two dimensional signal yield which provides number of events for simultaneously produced $Y(1S)$ and J/ψ .
- a_i : Acceptance for an event i for simultaneously produced $Y(1S)$ and J/ψ mesons. The acceptance was found using an event-by-event data embedding method.
- ϵ_i : Efficiency of $Y(1S) + J/\psi$ events for the event i . This is also defined with an event-by-event data embedding method.
- L : Total effective luminosity.
- BFs : Branching fractions of $Y(1S)$ and J/ψ mesons decaying to muon pairs. These values were taken from Particle Data Group (PDG) [42].

The data in this analysis was obtained from proton-proton collisions at 8 TeV in the LHC, recorded by the CMS detector. A JSON file is a short Java Script Object used within CMS to give a well-defined dataset and access the data easily. In this study, we used the JSON file that is commonly used for muon physics analysis. We used Muonia datasets and calculated luminosities using the `pixelLumiCalc.py` script. The data and corresponding luminosities are tabulated in Table 5.1.

In order to identify an acceptance region, we generated Monte Carlo samples for $Y(nS)$ and J/ψ mesons using a particle gun. The particle gun is a Pythia6 Monte Carlo generator and we used the particle ID of $Y(nS)$ and J/ψ mesons and the muons to generate Monte Carlo events for single $Y(1S)$, $Y(2S)$, $Y(3S)$, and J/ψ . Both $Y(nS)$ and J/ψ mesons were generated and reconstructed in `CMSSW_5_3_7_patch5` release with the global tag `START53V_18`.

Table 5.1: Datasets, run ranges, and corresponding luminosities.

Datasets	Run range	Effective Lumi	Delivered Lumi
/Muonia/Run2012A-22Jan2013-v1/AOD	190456-193621	0.924fb^{-1}	0.965fb^{-1}
/Muonia/Run2012B-22Jan2013-v1/AOD	193834-196531	4.829fb^{-1}	4.925fb^{-1}
/Muonia/Run2012C-22Jan2013-v1/AOD	198022-203742	7.310fb^{-1}	7.430fb^{-1}
/Muonia/Run2012D-22Jan2013-v1/AOD	203777-208686	7.576fb^{-1}	7.718fb^{-1}
Sum		20.639fb^{-1}	21.038fb^{-1}

5.3 Event Selection and Reconstruction

One possible decay mode for $Y(1S)$ and J/ψ mesons is both mesons decaying to muon pairs. For this reason, we must have four muons in the final states and the total charge must be equal to zero for reconstruction of the $Y(1S)$ and J/ψ candidates. Since we will have two muons from the decay of both the $Y(1S)$ and J/ψ mesons, we sorted the pairs into three combinations as shown in Table 5.2. As can be seen in the table, one of the combinations is eliminated because of the charge requirement.

Table 5.2: Possible pair combination of $Y(1S) + J/\psi$ events with four muons final state.

First Pair	Second Pair	Charge of 1 st pair	Charge of 2 nd pair
$\mu_1\mu_2$	$\mu_3\mu_4$	+ -	- +
$\mu_1\mu_3$	$\mu_2\mu_4$	+ -	- +
$\mu_1\mu_4$	$\mu_2\mu_3$	++	--

The following selection criteria was used for reconstruction:

- We defined muon pairs as high mass and low mass pairs. The high mass pair includes $Y(1S)$ candidates and the low mass pair includes J/ψ candidates.
- $|\eta| < 2.4$ for each muon since muon chambers are located in the barrel and endcap regions of the CMS detector ($-2.5 < \eta < 2.5$).
- Used “new soft muon ID”. The definition of new muon ID applies several requirements on the muon track, which are listed below:
 - The transverse and longitudinal impact parameters are respectively $d_{xy} < 0.3$ cm, $d_z < 20$ cm with respect to primary vertex;
 - The track must match at least one stub in the muon chambers.
 - The track must have at least six hits in the silicon strip detector and at least one hit in the pixel detector.
 - The track must pass a quality requirement which rejects outliers.

Further requirements are applied on the reconstruction of the di-muon and four-muon vertices and invariant masses.

- The probability of four muons originating from the same vertex (four-muon vertex probability) must be greater than 5%.
- Possibility of two muons origination from the same vertex (dimuon vertex probability with confidence level) must be greater than 0.5%. This is a trigger requirement for dimuons.
- The event must be selected by the `HLT_Dimuon_JPsi_Muon_v*` or `HLT_Dimuon_Upsilon_Muon_v*` triggers. The requirements of these two trigger paths can be summarized as:

- Two muons with opposite charge.
 - No requirement on minimum muon transverse momentum.
 - The pseudorapidity of the muons has to be in the interval $[-2.5, 2.5]$.
 - The invariant mass of the di-muon pair is required to be in the interval $[2.8 \text{ GeV}, 3.35 \text{ GeV}]$ and $[8.5 \text{ GeV}, 11.5 \text{ GeV}]$ for the J/ψ and Υ paths respectively.
- The two muons forming the offline Υ candidate must be the same pair that fired the Υ trigger. A further requirement of a third muon is applied such that the triplet is contained in a cone of $\Delta R = 2$ (Trigger requirement).
 - To have $\Upsilon(1S)$ or J/ψ candidate from the combination of muons, we expect that two muons that result from $\Upsilon(1S)$ and J/ψ have a mass value that is close to mass value of $\Upsilon(1S)$ or J/ψ mesons. However, it is possible that the mass of dimuon pair will be different than $\Upsilon(1S)$ or J/ψ mass. If there are two or more muon pairs with this condition (one pair mass is close to the mass of $\Upsilon(1S)$ or J/ψ and the other pair mass is very different than the mass of $\Upsilon(1S)$ or J/ψ), the pairs which have a very different mass must be excluded from the reconstructed data events. Otherwise, these pairs will cause double events (one correct and one not-correct combination). To avoid double counting, we calculated the d variable as shown in equation 14. Here, the combination that has minimum value of d was selected.

$$d^2 = (M_{\mu_1\mu_2} - M_{\Upsilon})^2 + (M_{\mu_3\mu_4} - M_{J/\psi})^2 \quad (14)$$

Here, $M_{\mu_1\mu_2}$ and $M_{\mu_3\mu_4}$ are the mass value of muon pairs from selected data events and M_{Υ} and $M_{J/\psi}$ are the mass value of Υ and J/ψ mesons ($9.46 \text{ GeV}/c^2$ and $3.09 \text{ GeV}/c^2$ respectively).

More selection criteria were used for the transverse momentum of muons, Υ and J/ψ mesons based on detector acceptance as discussed in Sections 5.4.1 and 5.4.2.

5.4 Acceptance and Efficiency

The CMS detector has a cylindrical shape that defines an acceptance region for muons. Therefore, a muon must have a certain transverse momentum to reach the muon chambers of the CMS detector in a magnetic field of 3.8 T. In order to understand what kinematic cuts must be used on the muons, $\Upsilon(1S)$ and J/ψ mesons, we checked the muon acceptance, $\Upsilon(1S)$ acceptance, and J/ψ acceptance in the CMS detector.

5.4.1 Muon Acceptance

We used a Pythia6 particle gun MC generator to study muon acceptance, defining the acceptance region based on studies of simulated $\Upsilon(1S)$ and J/ψ mesons decaying to muon pairs. $\Upsilon(1S)$ and J/ψ MC events were generated requiring the pseudorapidity range of the CMS detector ($|\eta| < 2.4$) for the muons. Figure 5.1 is a two-dimensional histogram showing the detector acceptance of muons resulting from $\Upsilon(1S)$ and J/ψ mesons. In this figure the x-axis is the pseudorapidity range and the y-axis is the muon transverse momentum. We then match the reconstructed muons to the generated muons according to the requirements below:

$$\delta R = \sqrt{\delta\phi^2 + \delta\eta^2} < 0.1 \quad (15)$$

$$\frac{|p_T^{gen} - p_T^{reco}|}{p_T^{gen}} < 0.1 \quad (16)$$

where, $\delta\phi = \phi_{reco} - \phi_{gen}$ and $\delta\eta = \eta_{reco} - \eta_{gen}$.

We looked at the ratio between reconstructed muons and generated muons as shown in Figure 5.2. As can be seen in the figure, the muons have low detectability in the high eta region and low p_T region. Looking at the acceptance map in Figure 5.2, we require p_T^μ to be greater than a certain transverse momentum for different eta regions. We did not use any selection criteria for muon transverse momentum in the generated level; however, we used the following selection criteria in the reconstruction level based on acceptance greater than 50%.

- If $|\eta^\mu| < 0.8$, then $p_T^\mu > 3$ GeV/c
- If $0.8 < |\eta^\mu| < 1.6$, then $p_T^\mu > 3 \rightarrow 2$ GeV/c (p_T^μ linearly decreases from 3 to 2 GeV/c)
- If $1.6 < |\eta^\mu| < 2.4$, then $p_T^\mu > 2$ GeV/c.

These selection criteria were used on the data to decrease the possibility of bias in the yield.

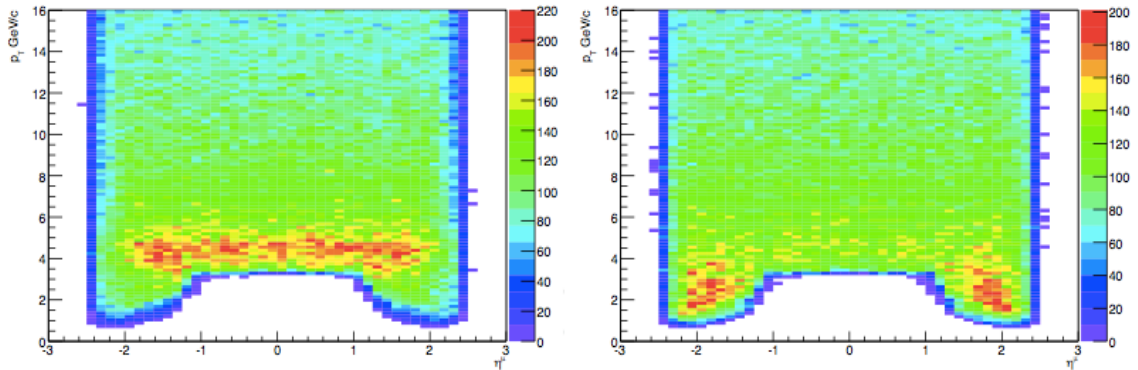


Figure 5.1: Reconstructed single muon acceptance as a function of η^μ vs. p_T^μ . On the left muons from $Y(1S)$ decay and on the right muons from J/ψ decay.

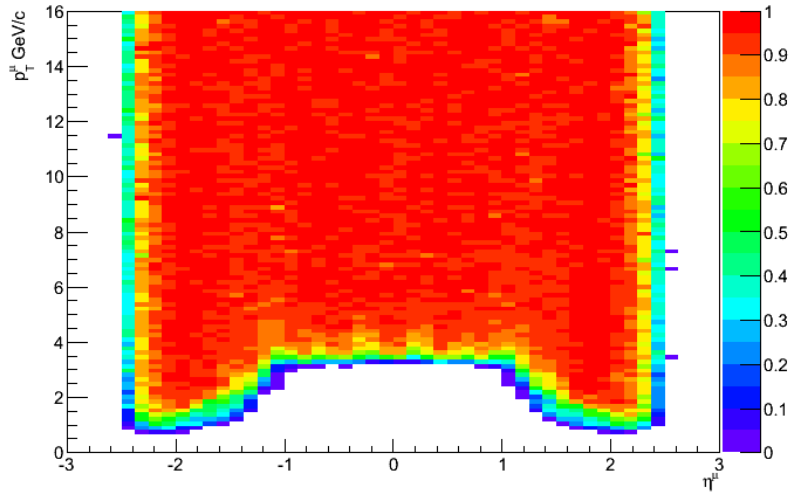


Figure 5.2: Single muon acceptance map. Muon acceptance was defined taking ratio of reconstructed muons to generated muons as a function of η vs. p_T .

5.4.2 $\Upsilon(1S)$ and J/ψ Acceptance

As mentioned in Section 5.4.1, the muon acceptance shows what kinematic cuts need to be used on the muons. Similarly, it may also be necessary to use selection criteria on the transverse momentum of the $\Upsilon(1S)$ and J/ψ mesons. For this reason, we examined the acceptance of $\Upsilon(1S)$ and J/ψ mesons to determine what kinematic cuts need to be used on the data for these mesons.

Figure 5.3 shows two-dimensional $\Upsilon(1S)$ and J/ψ acceptance histograms as a function of p_T^{meson} and $|y_{meson}|$. For muons that result from $\Upsilon(1S)$ and J/ψ mesons, we used the same cuts that were discussed in Section 5.4.1. As shown in Figure 5.3 (right), we do not need to use any cuts on $p_T^{\Upsilon(1S)}$ because the $\Upsilon(1S)$ meson is accepted by the detector for each $p_T^{\Upsilon(1S)}$ and $|y|$ bins. However, as shown in Figure 5.3 (left), there are

some points where the detector does not accept the J/ψ mesons completely. To eliminate these regions, we must use the following criteria on $p_T^{J/\psi}$ for different rapidity regions.

- If $|y^{J/\psi}| \leq 0.8$, then $p_T^{J/\psi} > 6.5$ GeV/c.
- If $0.8 < |y^{J/\psi}| \leq 1.4$, then $p_T^{J/\psi} > 6.5 \rightarrow 4$ GeV/c ($p_T^{J/\psi}$ linearly decreases from 6.5 to 4 GeV/c).
- If $1.4 < |y^{J/\psi}| \leq 2.0$, then $p_T^{J/\psi} > 4$ GeV/c.

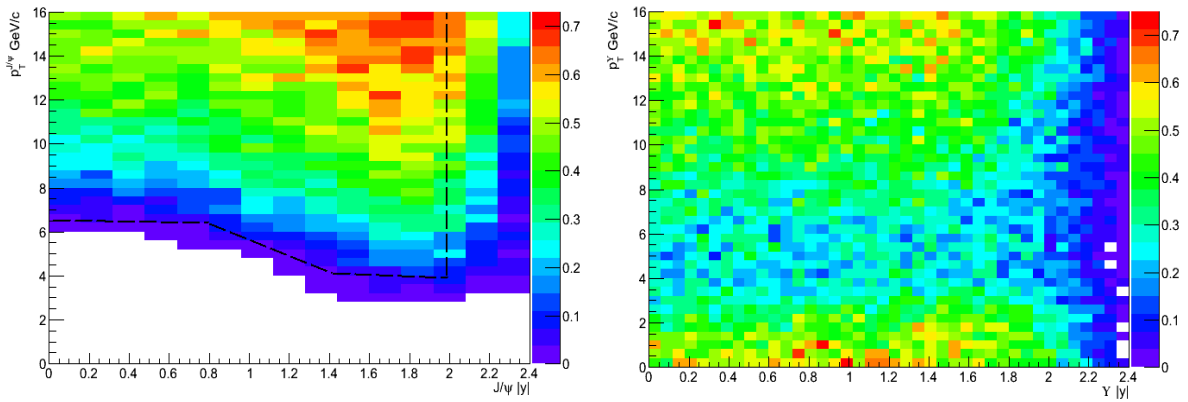


Figure 5.3: $\Upsilon(1S)$ and J/ψ acceptance. J/ψ acceptance as a function of $|y|$ vs. p_T is on the left. $\Upsilon(1S)$ acceptance as a function of $|y|$ vs. p_T is on the right.

5.4.3 Event-by-Event Acceptance and Efficiency Corrections

In the previous section, we looked at the detector acceptance of muons, $\Upsilon(1S)$ and J/ψ mesons since the CMS detector has a cylindrical shape and requires a minimum momentum for a muon to reach the muon chambers of the detector. To calculate the cross section of simultaneously produced $\Upsilon(1S)$ and J/ψ , we can use the acceptance values of each bin from the previous section. However, these results may be biased since we used a particle gun to produce the events, while in the data, the four muons from the J/ψ and

$Y(1S)$ mesons are correlated. For this reason, we prefer to use an event-by-event data embedding method to correct the data with efficiency.

For this acceptance study, we used the data as the starting point; applying the selection criteria (η and p_T cuts) described in the previous sections, yielded 585 events. We select the three momenta of both the $Y(1S)$ and J/ψ mesons (p_x, p_y, p_z) for each event and put them into a particle gun sample fixing the mass of $Y(1S)$ and J/ψ to $9.46 \text{ GeV}/c^2$ and $3.09 \text{ GeV}/c^2$ respectively. We simulate each event 10000 times requiring isotropic decay of the $Y(1S)$ and J/ψ mesons. We use same selection criteria as the data to check how many of these simulated events passed the selection criteria. We define acceptance for each event as the number of simulated events that pass the selection criteria divided by total number of simulated events as shown in Equation 17.

$$a_i = \frac{N_i^{passed}}{N_i^{total}} \quad (17)$$

where:

- a_i : Acceptance for an event i .
- N_i^{passed} : Number of resulting muons that pass muon acceptance criteria (number of simulated events that passed selection criteria).
- N_i^{total} : Number of trials for the event that we calculate acceptance for (total number of simulated events. Each event is simulated 10K times).

We plotted event-by-event acceptance values in Figure 5.4 for $Y(1S) + J/\psi$ events.

To calculate the cross section based on the formula in Equation 13, we need to find the acceptance for the $Y(1S)$ and J/ψ mesons. In addition to the event-by-event acceptance, we also need to find the efficiency of $Y(1S)$ and J/ψ . This is also must be found using an event-by-event data embedding method. To do this, we repeatedly

substituted the measured four momenta of muons from selected data events into a generated MC event, which is then subject to the complete CMS detector simulation and reconstruction chain. We used same selection criteria described in Section 5.3.

For each of the reconstructed candidate data events, we generated 1000 different substituted events to see how often four of the muons reach the muon chambers of the CMS detector. The efficiency correction for a selected event was determined as the number of substituted events that pass the selection criteria divided by the total substituted events. Figure 5.5 shows the average event-by-event efficiency in bins of four muon p_T , lowest muon p_T and Pile-Up which is defined as the number of primary vertices reconstructed per event. As can be seen in the figure, the average efficiency changes with p_T and Pile-Up as expected. We take the average value of event-by-event acceptance and efficiency to calculate the cross section of $\Upsilon(1S) + J/\psi$ as explained in Section 5.9.

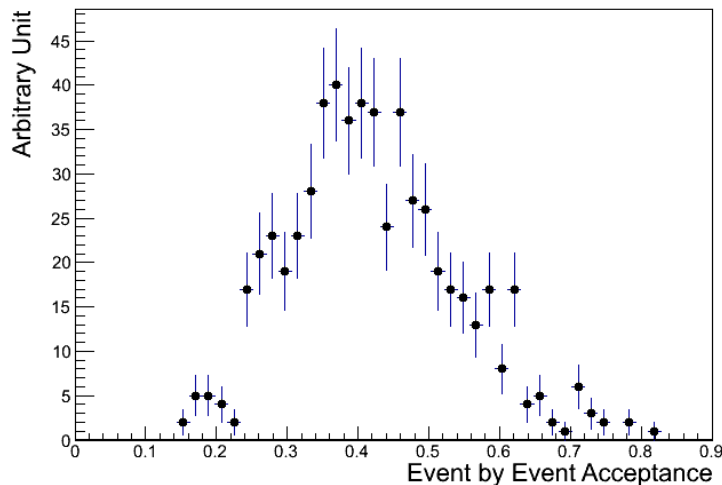


Figure 5.4: Event-by-event acceptance values were defined using a data embedding method assuming isotropic decay of $\Upsilon(1S)$ and J/ψ mesons.

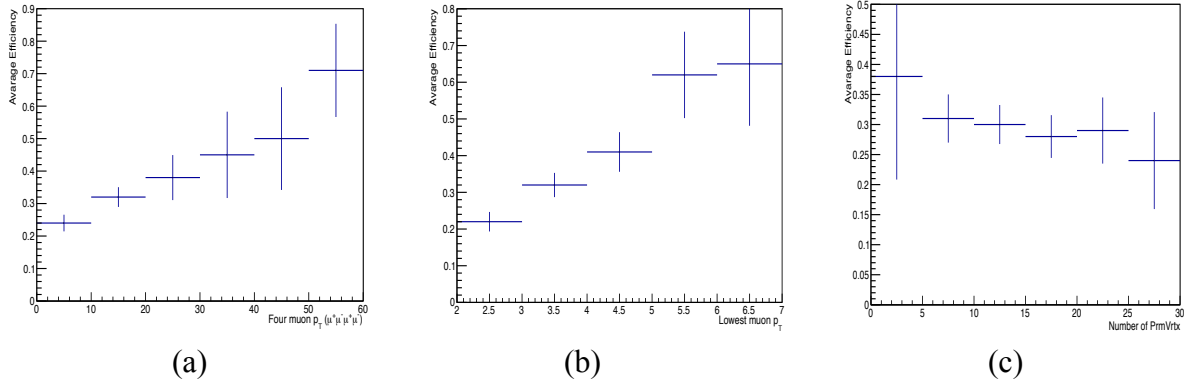


Figure 5.5: Average event-by-event efficiency in bins of a) four-muon p_T b) lowest muon p_T c) pile-up defined here as the number of primary vertices reconstructed per event.

5.5 Simultaneously Produced $Y(1S)$ and J/ψ Events at CMS

Next, we return to our four-muon dataset, where the four muons are divided into high mass and low mass pairs. The low mass pair, $m(\mu^+\mu^-)_l$, includes J/ψ candidates and the high mass pair, $m(\mu^+\mu^-)_h$, includes $Y(1S)$ candidates. Figure 5.6 shows the high mass and low mass pairs and the background for the selected $Y(1S)+J/\psi$ candidate events. As shown in the figure, there are four components in the data sample. The first component is the signal events of $Y(1S)+J/\psi$, which can be seen at the intersection of the $Y(1S)$ and J/ψ mass values. The second component is $Y(1S) + \mu^+\mu^-$ events which are all points at $m(\mu^+\mu^-)_h = 9.46$ and $m(\mu^+\mu^-)_l$ can be any mass except that of the J/ψ . The third component is $J/\psi + \mu^+\mu^-$ events which are all points at $m(\mu^+\mu^-)_l = 3.09$ and $m(\mu^+\mu^-)_h$ at any mass value except that of the $Y(1S)$. The fourth component is $\mu^+\mu^- + \mu^+\mu^-$ events, which are all the remaining points excluding dimuon pairs at the mass values of the J/ψ or $Y(1S)$ masses. While looking at two-dimensional and three-dimensional fits of simultaneously produced $Y(1S)$ and J/ψ events, we must consider

those four components. The first component ($Y(1S)+J/\psi$) is the signal events and the others are background components.

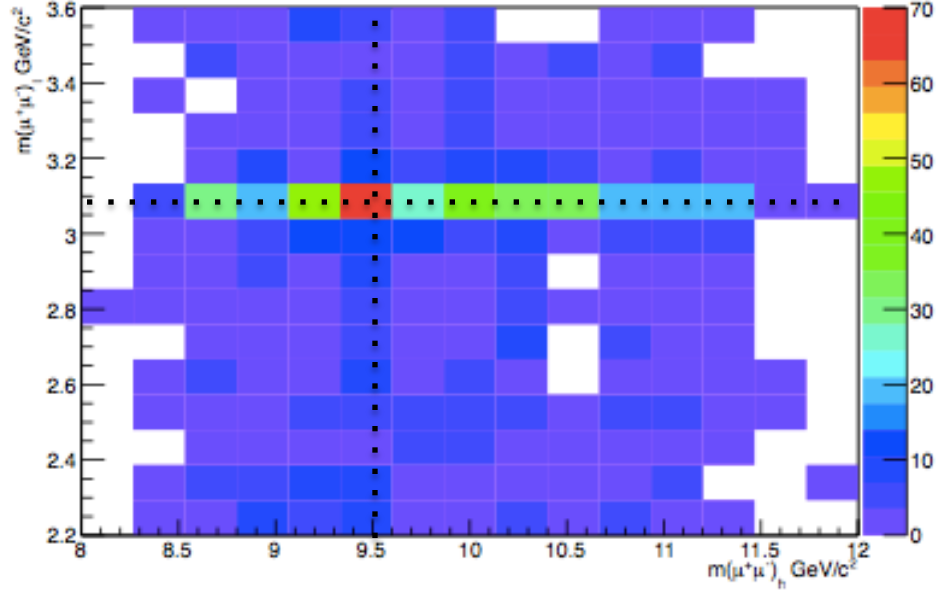


Figure 5.6: Two-dimensional view of high mass and low mass pairs.

Because the $\mu^+\mu^- + \mu^+\mu^-$ component is both at higher and lower masses than the Y and J/ψ , we divide this component into four regions to fit the Background distribution in order to find the background component in the signal region. The first region is $8.5 < (\mu^+\mu^-)_h < 9.2$ and $1.1 < (\mu^+\mu^-)_l < 2.9$. The second region is $10.6 < (\mu^+\mu^-)_h < 11.5$ and $1.1 < (\mu^+\mu^-)_l < 2.9$. The third region is $10.6 < (\mu^+\mu^-)_h < 11.5$ and $3.2 < (\mu^+\mu^-)_l < 3$. The fourth region is $8.5 < (\mu^+\mu^-)_h < 9.2$ and $3.2 < (\mu^+\mu^-)_l < 3.6$. These numbers are input to our signal fit. Figure 5.7 shows the mass distribution for the high and low mass pairs in the four regions. We fit the dimuon mass distributions to extract the $\mu^+\mu^-$ background component in our signal region. A generic pdf such as $C_0 + C_1 * m(\mu^+\mu^-)_h +$

$C_2 * m(\mu^+ \mu^-)_l$ was used to fit these distributions. Fit parameters of these distributions are given in Table 5.3.

Table 5.3: Fit parameters and values for the background mass distribution for the high mass and low mass pairs.

Fit Parameters	Fit Value
C_0	9.998×10^{-1}
C_1	-8.081×10^{-2}
C_2	1.510×10^2

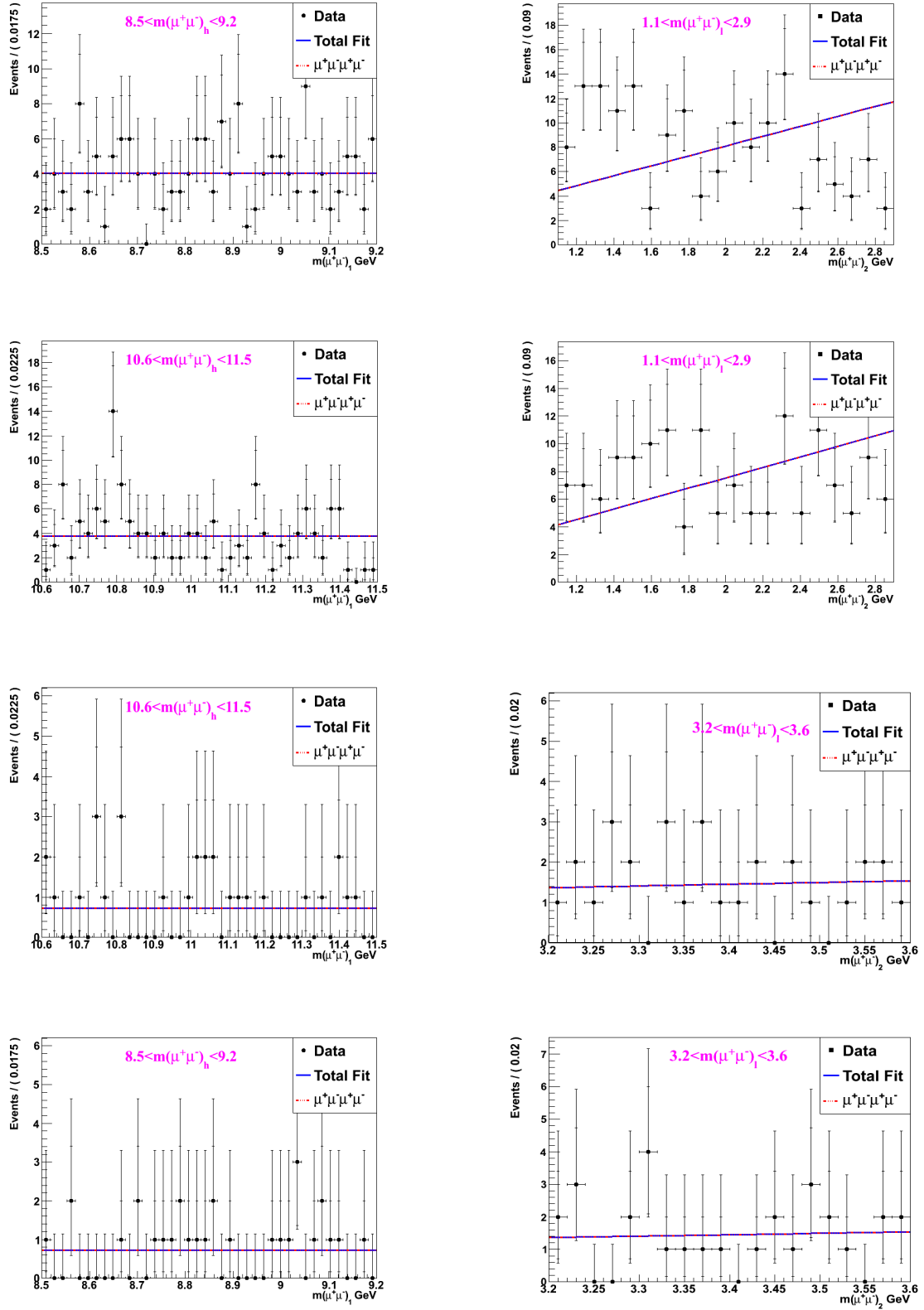


Figure 5.7: The mass distribution for the high and low mass pairs in the four regions.

5.5.1 Maximum Likelihood Fit

To understand the signal peak after CMS detector reconstruction, we used the Pythia6 particle gun to produce 500,000 J/ψ and $\Upsilon(nS)$ events. As we used selection criteria in the data, we also used some selection criteria to find the invariant mass of $\Upsilon(nS)$ and J/ψ for Monte Carlo samples. The following selection criteria were used on the muon pairs of $\Upsilon(nS)$ and J/ψ decays.

- Due to detector acceptance, each muon must have a certain transverse momentum for different eta regions as shown below.
 - ✓ If $|\eta^\mu| < 0.8$, then $p_T^\mu > 3$ GeV/c
 - ✓ If $0.8 < |\eta^\mu| < 1.6$, then $p_T^\mu > 3 \rightarrow 2$ GeV/c (p_T^μ linearly decreases from 3 to 2 GeV/c)
 - ✓ If $1.6 < |\eta^\mu| < 2.4$, then $p_T^\mu > 2$ GeV/c.
- $|\eta| < 2.4$ for each muon.
- The dimuon vertex probability must be greater than 0.5%.
- The muons in each decays must have opposite charge with total charge equal to zero.

We then fit the dimuon mass distribution with the double crystal ball function. Figure 5.8 shows the one-dimensional fit of the $\Upsilon(nS)$ and J/ψ Monte Carlo events. Tables 5.4, 5.5, 5.6, and 5.7 show the fit parameters and fit values for MC events (see Section 5.1.1 equation 11 for explanation of these parameters).

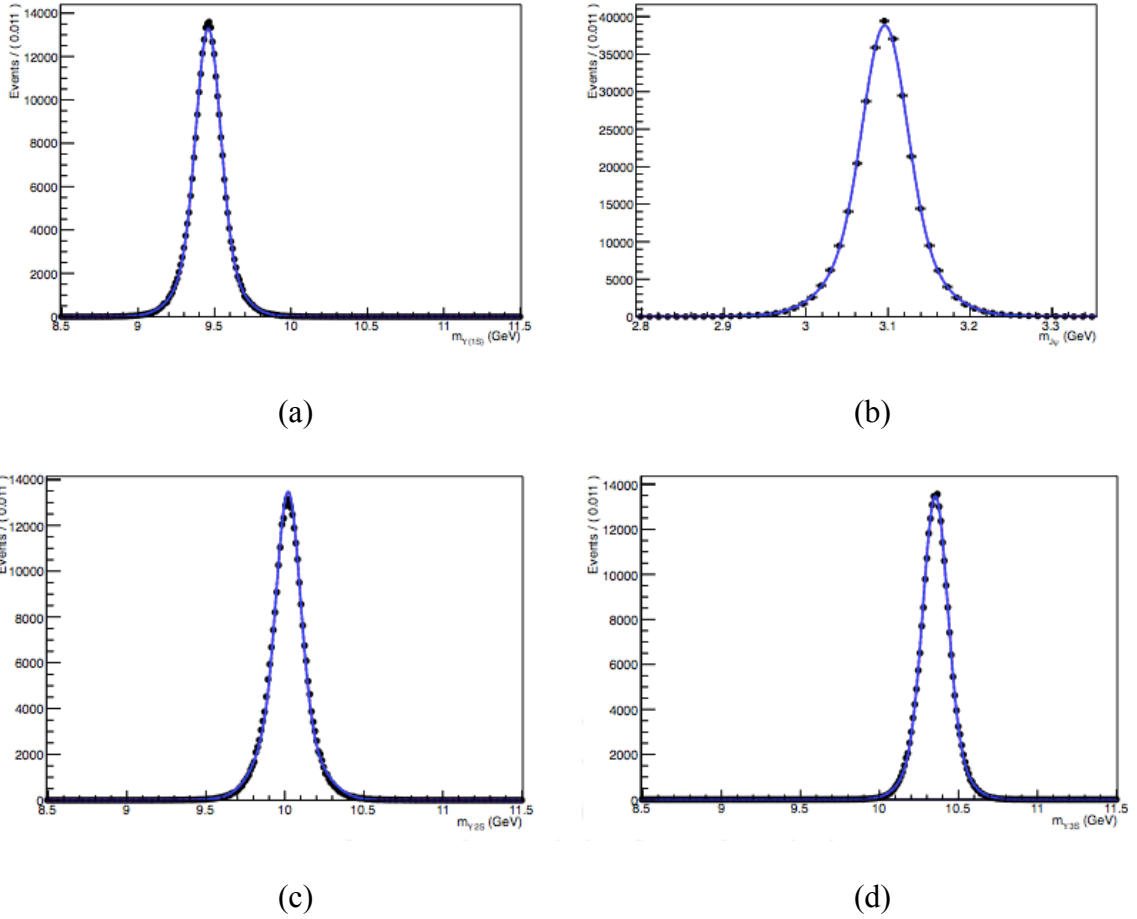


Figure 5.8: Reconstructed mesons from MC simulation a) $\Upsilon(1S)$ b) J/ψ c) $\Upsilon(2S)$ d) $\Upsilon(3S)$ MC events.

Table 5.4: MC fit parameters of J/ψ .

Parameter's Name	Fit Value
Mean1 and Mean2 Double Crystal Ball	3.09 GeV/c^2
Sigma 1	0.03 GeV/c^2
Sigma 2	0.05 GeV/c^2
n_1	3.90
n_2	5.00
Alpha 1	1.70
Alpha 2	-2.10

Table 5.5: MC fit parameters of $\Upsilon(1S)$.

Parameter's Name	Fit Value
Mean1 and Mean 2 Double Crystal Ball	9.46 GeV/c ²
Sigma 1	0.07 GeV/c ²
Sigma 2	0.20 GeV/c ²
n_1	5.00
n_2	5.00
Alpha 1	1.60
Alpha 2	5.00

Table 5.6: MC fit parameters of $\Upsilon(2S)$.

Mean1 and Mean 2 Double Crystal Ball	10.02 GeV/c ²
Sigma 1	0.08 GeV/c ²
Sigma 2	0.20 GeV/c ²
n_1	4.40
n_2	4.40
Alpha 1	1.60
Alpha 2	2.50

Table 5.7: MC fit parameters of $Y(3S)$.

Parameter's Name	Fit Value
Mean1 and Mean 2 Double Crystal Ball	10.40 GeV/c ²
Sigma 1	0.08 GeV/c ²
Sigma 2	0.20 GeV/c ²
n_1	7.00
n_2	1.40
Alpha 1	4.90
Alpha 2	3.02

After characterizing the signal shape for the invariant mass of the $Y(nS)$ and J/ψ mesons, we look at simultaneously produced $Y(1S)$ and J/ψ mesons using a two-dimensional extended likelihood fit on the data. As stated in section 5.3, we divided muons into six components and required one muon pair to have greater mass than the other. In this case, the high mass component includes the $Y(1S)$ candidate and the low mass component includes the J/ψ candidate. To clarify $Y(1S)$ and J/ψ candidates into these pairs, we required the high mass region to be between 8.5 GeV/c² and 11.5 GeV/c² and the low mass region to be between 2.8 GeV/c² and 3.4 GeV/c². To increase significance (σ) and decrease background, we included $Y(2S)$ and $Y(3S)$ candidates into the fit. Using a two-dimensional maximum likelihood fit on high mass and low mass pairs, we determined the signal yield of simultaneously produced $Y(1S)$ and J/ψ events ($Y(1S) + J/\psi$). We defined the total maximum likelihood probability density function (pdf) for two-dimensional fit as follows:

$$\begin{aligned}
\mathcal{L} = & N_{Y(1S)+J/\psi} [C.B(M_{\mu\mu}^1) * C.B(M_{\mu\mu}^2)] + N_{Y(1S)+\mu\mu} [C.B(M_{\mu\mu}^1) * Poly(M_{\mu\mu}^2)] \\
& + N_{J/\psi+\mu\mu} [C.B(M_{\mu\mu}^2) * Poly(M_{\mu\mu}^1)] + N_{Y(2S)+J/\psi} [C.B(M_{\mu\mu}^1) * C.B(M_{\mu\mu}^2)] \\
& + N_{Y(2S)+\mu\mu} [C.B(M_{\mu\mu}^1) * Poly(M_{\mu\mu}^2)] + N_{Y(3S)+J/\psi} [C.B(M_{\mu\mu}^1) * C.B(M_{\mu\mu}^2)] \\
& + N_{Y(3S)+\mu\mu} [C.B(M_{\mu\mu}^1) * Poly(M_{\mu\mu}^2)] + N_{\mu\mu+\mu\mu} [C_0 + C_1*(M_{\mu\mu}^1) + C_2*(M_{\mu\mu}^2)]
\end{aligned} \tag{18}$$

where:

- $N_{Y(1S)+J/\psi}$: Number of signal yield for the two-dimensional fit; simultaneously produced $Y(1S)$ and J/ψ mesons.
- $N_{Y(1S)+\mu\mu}$: Number of $Y(1S)$ candidates with non-resonant $\mu^+\mu^-$ pair.
- $N_{J/\psi+\mu\mu}$: Number of J/ψ candidates with non-resonant $\mu^+\mu^-$ pair.
- $N_{Y(2S)+J/\psi}$: Number of $Y(2S) + J/\psi$ candidates .
- $N_{Y(2S)+\mu\mu}$: Number of $Y(2S)$ candidates with non-resonant $\mu^+\mu^-$ pair.
- $N_{Y(3S)+J/\psi}$: Number of $Y(3S) + J/\psi$ candidates.
- $N_{Y(3S)+\mu\mu}$: Number of $Y(3S)$ candidates with non-resonant $\mu^+\mu^-$ pair.
- $N_{\mu\mu+\mu\mu}$: Number of non-resonant $\mu^+\mu^- + \mu^+\mu^-$ pair. $C_0 + C_1*(M_{\mu\mu}^1) + C_2*(M_{\mu\mu}^2)$ is a generic pdf to define background. Here, $M_{\mu\mu}^1$ is the high mass pair and $M_{\mu\mu}^2$ is the low mass pair.

As shown in the total pdf of the two-dimensional likelihood fit, a double Crystal Ball function was used to fit the signal yield and a second order Chebyshev polynomial was used to fit the non-resonant parts of the high mass and the low mass pairs. Using the fit parameters in Table 5.3, we used a generic pdf to fit the background shape for non-resonant muon pairs. We fixed the shape of the signal using Monte Carlo fit parameters

of the $\Upsilon(nS)$ and J/ψ mesons as given in Tables 5.4, 5.5, 5.6 and 5.7. We fit the data with a two-dimensional extended likelihood fit, as shown in Figure 5.9. This fit gives $\Upsilon(1S) + J/\psi$ signal yield, which is Tabulated in table 5.8 with other fit values. As shown in the table, the signal yield for $\Upsilon(1S) + J/\psi$ is $64 \pm 14(\text{stat})$.

In order to check if the fit is good, we looked at the pull distribution of two-dimensional fit as shown in Figure 5.9 (the rectangle shapes underneath of the figure). For a good fit, the pull value must not be higher than 5σ . We defined the pull distribution as the ratio of the difference between the data and the fit to the error between them, as shown below:

$$\text{Pull} = \frac{\text{Data-Fit}}{\text{Error}} \quad (19)$$

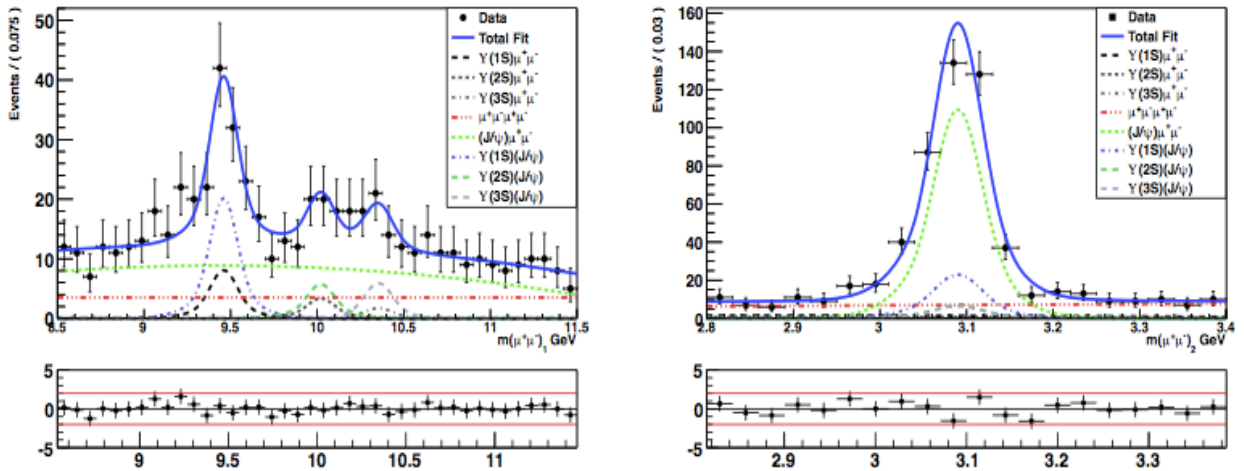


Figure 5.9: Extended two-dimensional likelihood fit of simultaneously produced $\Upsilon(1S)$ and J/ψ events. $\Upsilon(1S)$ candidate on the left and J/ψ candidate on the right. Bottom scales are pull distributions.

Table 5.8: The components and yield values for two-dimensional fit.

Two dimensional component's name	Yield \pm Error
Number of events for $\Upsilon(1S) + J/\psi$ (Signal Yield)	64 ± 14
Number of events for $\Upsilon(1S) + \text{non-resonant } \mu\mu$ pairs	26 ± 10
Number of events for $J/\psi + \text{non-resonant } \mu\mu$ pairs	306 ± 29
Number of events for $\Upsilon(2S) + J/\psi$	19 ± 11
Number of events for $\Upsilon(2S) + \text{non-resonant } \mu\mu$ pairs	11 ± 8
Number of events for $\Upsilon(3S) + J/\psi$	18 ± 10
Number of events for $\Upsilon(3S) + \text{non-resonant } \mu\mu$ pairs	5 ± 6
Number of non-resonant events	141 ± 18

To calculate the signal significance, we perform two separate un-binned maximum likelihood fits on the data; a fit with a hypothesis of signal + background and a background only fit. The signal-hypothesis (L_s) fit is the same as the extended two-dimensional likelihood fit done previously, using the same eight defined components. ($\Upsilon(1S) + J/\psi, \Upsilon(1S) + \mu^+\mu^-, J/\psi + \mu^+\mu^-, \mu^+\mu^- + \mu^+\mu^-, \Upsilon(2S) + \mu^+\mu^-, \Upsilon(3S) + \mu^+\mu^-, \Upsilon(2S) + J/\psi, \Upsilon(3S) + J/\psi$).

The second fit is the null-hypothesis (background only) fit. To examine the null-hypothesis (L_0), we excluded the signal candidate ($\Upsilon(1S) + J/\psi$) events in order to see the difference between the fractions of the two hypotheses. For this reason, this fit only consists of the last seven components. These are $\Upsilon(1S) + \mu^+\mu^-, J/\psi + \mu^+\mu^-, \mu^+\mu^- + \mu^+\mu^-, \Upsilon(2S) + \mu^+\mu^-, \Upsilon(3S) + \mu^+\mu^-, \Upsilon(2S) + J/\psi$, and $\Upsilon(3S) + J/\psi$. We found the signal fractions for both of the hypotheses using RooFit. Using Wilk's theorem [43], the signal significance was calculated as follows:

$$Significance = \sqrt{2 * \ln \frac{L_0}{L_s}} = 4.4\sigma \quad (20)$$

In CMS analyses, the threshold of significance to be considered as evidence of a process is 3σ while 5σ is considered observation.

An important issue for this signal is to confirm that both J/ψ and Υ candidates originate from the same interaction. This analysis is based on a 5% four-muon vertex probability cut. This vertex cut minimizes the possibility of displaced J/ψ events from B decay. After using this selection cut, we have to make sure that there are no displaced J/ψ events in the reconstructed data events. We can check this possibility adding another parameter into the fit. Since B has a lifetime (τ), we can look at the decay length ($c\tau$) of the J/ψ candidate because our J/ψ candidate must have a different lifetime than the displaced J/ψ events from B decay. In order to do this, we performed a three-dimensional extended likelihood fit on the data taking the decay length ($c\tau$) of J/ψ as third dimension. For three-dimensional fit, we used a double crystal ball function on the signal candidates and a Chebyshev polynomial for the non-resonant parts of the high mass and low mass pairs. For the third dimension ($c\tau$), we used a double Gaussian and exponential function where the double Gaussian of $c\tau$ defines the prompt component and the exponential of $c\tau$ defines the non-prompt component. The prompt component is the signal that we are looking for and the non-prompt component is a background process for the J/ψ candidate coming from B meson decay. The total pdf for the three-dimensional extended likelihood fit was defined as below:

$$\begin{aligned}
\mathcal{L} = & N_{Y(1S)+J/\psi+c\tau}^{prompt} [C.B(M_{\mu\mu}^1) * C.B(M_{\mu\mu}^2) * G(c\tau)] + N_{Y(1S)+J/\psi+c\tau}^{non-prompt} [C.B(M_{\mu\mu}^1) * C.B(M_{\mu\mu}^2) * expo(c\tau)] \\
& + N_{Y(1S)+\mu\mu+c\tau}^{prompt} [C.B(M_{\mu\mu}^1) * Poly(M_{\mu\mu}^2) * G(c\tau)] + N_{Y(1S)+\mu\mu+c\tau}^{non-prompt} [C.B(M_{\mu\mu}^1) * Poly(M_{\mu\mu}^2) * expo(c\tau)] \\
& + N_{J/\psi+\mu\mu+c\tau}^{prompt} [C.B(M_{\mu\mu}^2) * Poly(M_{\mu\mu}^1) * G(c\tau)] + N_{J/\psi+\mu\mu+c\tau}^{non-prompt} [C.B(M_{\mu\mu}^2) * Poly(M_{\mu\mu}^1) * expo(c\tau)] \\
& + N_{Y(2S)+J/\psi+c\tau}^{prompt} [C.B(M_{\mu\mu}^1) * C.B(M_{\mu\mu}^2) * G(c\tau)] + N_{Y(2S)+J/\psi+c\tau}^{non-prompt} [C.B(M_{\mu\mu}^1) * C.B(M_{\mu\mu}^2) * expo(c\tau)] \\
& + N_{Y(2S)+\mu\mu+c\tau}^{prompt} [C.B(M_{\mu\mu}^1) * Poly(M_{\mu\mu}^2) * G(c\tau)] + N_{Y(2S)+\mu\mu+c\tau}^{non-prompt} [C.B(M_{\mu\mu}^1) * Poly(M_{\mu\mu}^2) * expo(c\tau)] \\
& + N_{Y(3S)+J/\psi+c\tau}^{prompt} [C.B(M_{\mu\mu}^1) * C.B(M_{\mu\mu}^2) * G(c\tau)] + N_{Y(3S)+J/\psi+c\tau}^{non-prompt} [C.B(M_{\mu\mu}^1) * C.B(M_{\mu\mu}^2) * expo(c\tau)] \\
& + N_{Y(3S)+\mu\mu+c\tau}^{prompt} [C.B(M_{\mu\mu}^1) * Poly(M_{\mu\mu}^2) * G(c\tau)] + N_{Y(3S)+\mu\mu+c\tau}^{non-prompt} [C.B(M_{\mu\mu}^1) * Poly(M_{\mu\mu}^2) * expo(c\tau)] \\
& + N_{\mu\mu+\mu\mu+c\tau}^{prompt} [(C_0 + C_1 * (M_{\mu\mu}^1) + C_2 * (M_{\mu\mu}^2)) * G(c\tau)] + N_{\mu\mu+\mu\mu+c\tau}^{non-prompt} [(C_0 + C_1 * (M_{\mu\mu}^1) + C_2 * (M_{\mu\mu}^2)) * expo(c\tau)]
\end{aligned} \tag{21}$$

where:

- $N_{Y(1S)+J/\psi+c\tau}$: This is our signal candidate and $c\tau$ defined the decay length of the J/ψ candidate. We used a double crystal ball function for the signal candidate (the high mass and the low mass pairs). A double Gaussian function was used for $c\tau$.
- $N_{Y(1S)+\mu\mu+c\tau}$: Number of $Y(1S)$ + non-resonant $\mu\mu$ pairs.
- $N_{J/\psi+\mu\mu+c\tau}$: Number of J/ψ + non-resonant $\mu\mu$ pairs.
- $N_{Y(2S)+J/\psi+c\tau}$: Number of $Y(2S)$ + J/ψ candidates.
- $N_{Y(2S)+\mu\mu+c\tau}$: Number of $Y(2S)$ + non-resonant $\mu\mu$ pairs.
- $N_{Y(3S)+J/\psi+c\tau}$: Number of $Y(3S)$ + J/ψ candidates.
- $N_{Y(3S)+\mu\mu+c\tau}$: Number of $Y(3S)$ + non-resonant $\mu\mu$ pairs.
- $N_{\mu\mu+\mu\mu+c\tau}$: The number of non-resonant $\mu\mu$ + $\mu\mu$ pairs.
- Poly: Second order Chebyshev polynomial for the non-resonant part of the data.
- G: Double Gaussian function used on the decay length of the J/ψ candidate.

- $C_0 + C_1*(M_{\mu\mu}^1) + C_2*(M_{\mu\mu}^2)$: A generic pdf to define background for $\mu^+\mu^- + \mu^+\mu^-$ pairs.

Figure 5.10 shows the three-dimensional maximum likelihood fit for $Y(1S) + J/\psi + c\tau$. As can be seen in the figure, the data in the three-dimensional fit is identical to the data in the two-dimensional fit. Table 5.9 shows the fit parameters and fit values for the three-dimensional fit. As can be seen in the table, the number of signal event for the non-prompt component is equal to $5 \pm 4(stat)$, which means there are very few displaced J/ψ events from B decay. The number of events for signal candidates is 60 with 14 statistical error. This signal yield is very close to the signal yield of the two-dimensional fit. This is the expected result because the signal yield of the prompt component must be equal to the signal yield of the two-dimensional fit between error bars.

If we remove the vertex probability cut on the data, the exponential part of $c\tau$ will produce a tail as shown in Figure 5.11. This corresponds to events in the non-prompt signal component, which could indicate possible displaced J/ψ events from B decay. The requirement that the vertex probability is greater than 5% minimizes this possibility as shown in Table 5.9 (non-prompt signal yield is almost zero).

As shown in Table 5.10, the fit yields non-prompt events when we remove the vertex probability cut on the data. We expect that the signal yield of the prompt component should not change significantly when the vertex requirement is removed. A comparison of Tables 5.9 and 5.10 shows this is to be the case.

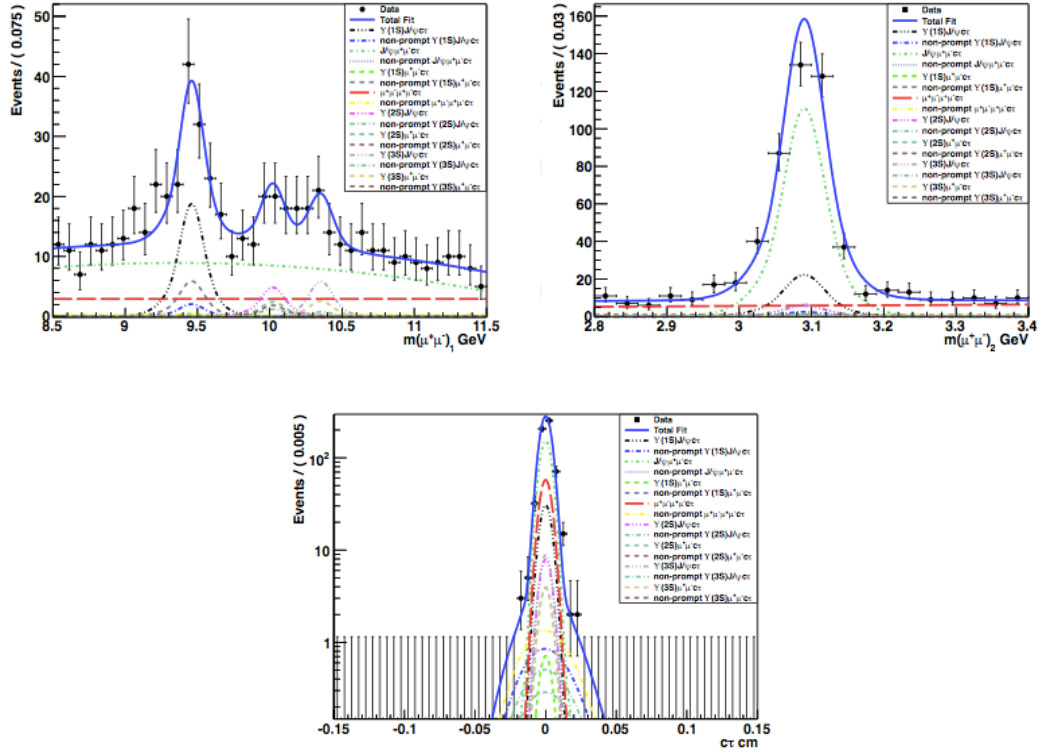


Figure 5.10: Three-dimensional maximum likelihood fit of $Y(1S) + J/\psi + c\tau$. Top-left: $Y(1S)$ candidate. Top-right: J/ψ candidate. Bottom: Decay length of J/ψ ($c\tau$).

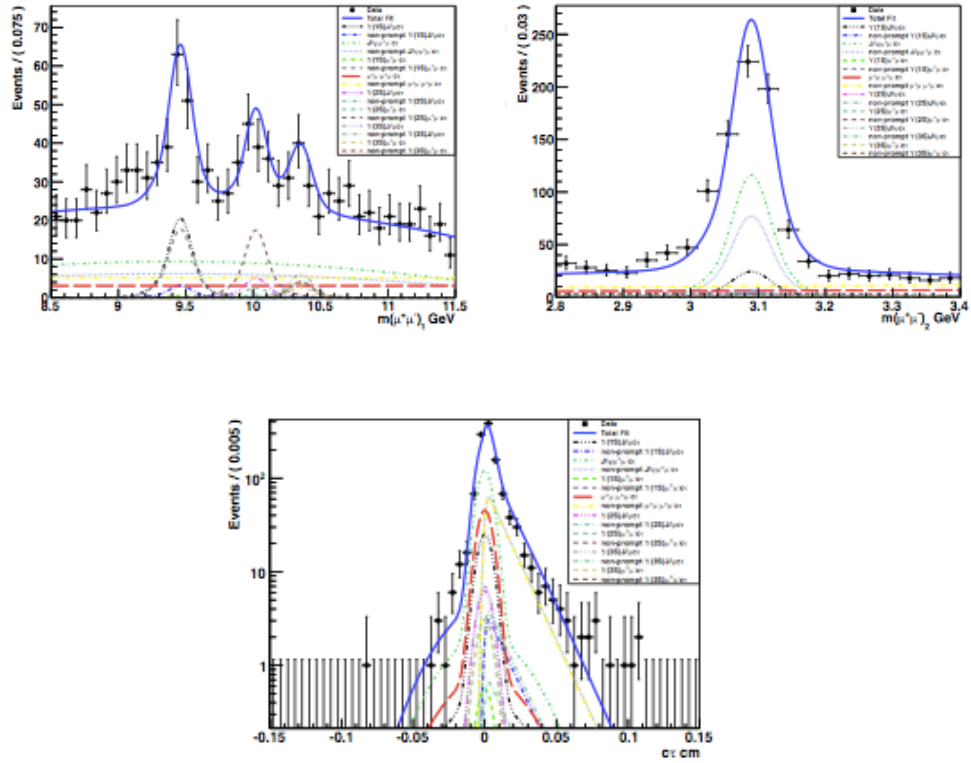


Figure 5.11: Three-dimensional maximum likelihood fit without four-muon vertex probability cut. Top-left: $\Upsilon(1S)$ candidate. Top-right: J/ψ candidate. Bottom: Decay length of J/ψ ($c\tau$).

Table 5.9: The components and yield values for three-dimensional fit.

	Three-Dimensional Component	Yield \pm Error
Prompt	$Y(1S) + J/\psi + c\tau$	60 ± 14
	$Y(1S) + \mu\mu + c\tau$	1 ± 7
	$J/\psi + \mu\mu + c\tau$	269 ± 20
	$Y(2S) + J/\psi + c\tau$	16 ± 11
	$Y(3S) + J/\psi + c\tau$	17 ± 10
	$Y(2S) + \mu\mu + c\tau$	18 ± 6
	$Y(3S) + \mu\mu + c\tau$	12 ± 8
	$\mu\mu + \mu\mu + c\tau$	114 ± 17
Non-prompt	$Y(1S) + J/\psi + c\tau$	5.0 ± 4.0
	$Y(1S) + \mu\mu + c\tau$	24 ± 9
	$J/\psi + \mu\mu + c\tau$	0.0 ± 7.0
	$Y(2S) + J/\psi + c\tau$	4 ± 3
	$Y(3S) + J/\psi + c\tau$	2 ± 3
	$Y(2S) + \mu\mu + c\tau$	6 ± 7
	$Y(3S) + \mu\mu + c\tau$	0 ± 6
	$\mu\mu + \mu\mu + c\tau$	10 ± 7

Table 5.10: The components and yield values for three-dimensional fit without four-muon vertex probability cut.

	Three-Dimensional Component	Yield \pm Error
Prompt	$Y(1S) + J/\psi + c\tau$	41 ± 19
	$Y(1S) + \mu\mu + c\tau$	30 ± 13
	$J/\psi + \mu\mu + c\tau$	362 ± 36
	$Y(2S) + J/\psi + c\tau$	23 ± 15
	$Y(3S) + J/\psi + c\tau$	23 ± 13
	$Y(2S) + \mu\mu + c\tau$	18 ± 12
	$Y(3S) + \mu\mu + c\tau$	10 ± 9
	$\mu\mu + \mu\mu + c\tau$	244 ± 28
Non-prompt	$Y(1S) + J/\psi + c\tau$	28 ± 19
	$Y(1S) + \mu\mu + c\tau$	55 ± 13
	$J/\psi + \mu\mu + c\tau$	266 ± 35
	$Y(2S) + J/\psi + c\tau$	7 ± 13
	$Y(3S) + J/\psi + c\tau$	18 ± 12
	$Y(2S) + \mu\mu + c\tau$	51 ± 13
	$Y(3S) + \mu\mu + c\tau$	8 ± 8
	$\mu\mu + \mu\mu + c\tau$	171 ± 23

5.6 Decay Length ($c\tau$) of J/ψ and Y

Since this analysis requires simultaneously produced $Y(1S)$ and J/ψ mesons, we required 5% probability cut for the four muons point to the same vertex and looked at decay length of J/ψ which is simultaneously produced with $Y(1S)$ using three dimensional un-binned maximum likelihood fit as explained in previous section (Section 5.5). To define combinatorial background components, the $c\tau$ distribution for the mass

sidebands of the Υ and J/ψ mass regions were examined. For this test, we divided the high mass and low mass pairs into three regions as shown in Figure 5.12. We defined sidebands for the J/ψ mass regions as [2.8-3.0], [3.0-3.2],[3.2-3.4] and for the Υ mass regions as [8.5-9.2],[9.2-10.5],[10.5-11.5].

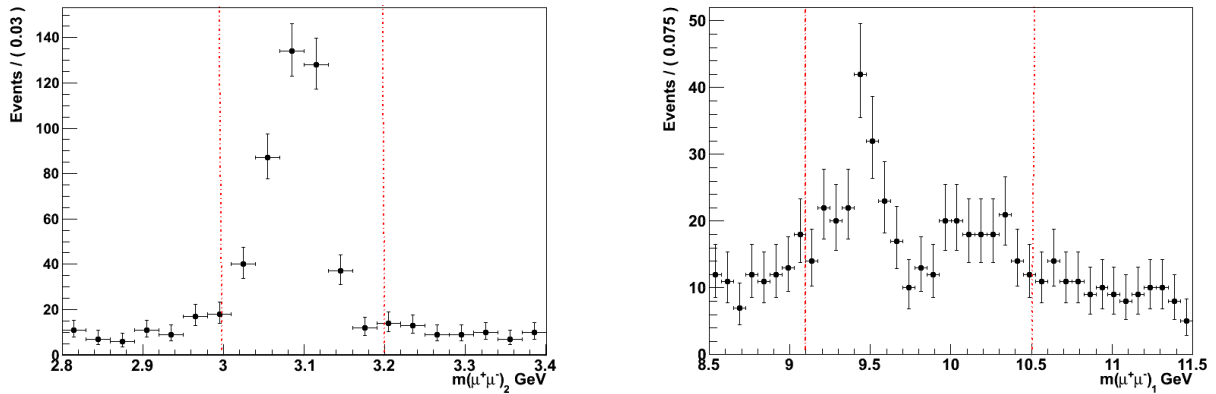


Figure 5.12: Divided high mass (on the right) and low mass (on the left) pairs into three regions for a definition of the sidebands.

The decay lengths of the high mass and low mass pairs for the entire mass window is shown in Figure 5.13. Figures 5.14, 5.15 and 5.16 show the decay lengths for the defined regions. As shown in Figure 5.14, there are more events for the signal region of Υ and J/ψ [3.0-3.2], [9.2-10.5] as expected. However, the statistics in the sidebands [2.8-3.0],[3.2-3.4],[8.5-9.2],[10.5-11.5] are too low to draw a solid conclusion as shown in Figures 5.15 and 5.16.

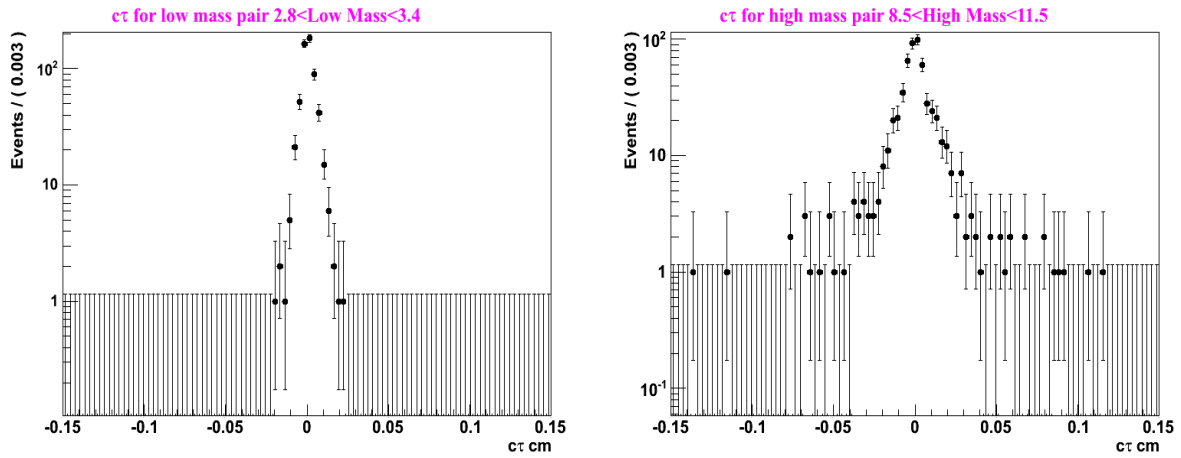


Figure 5.13: $c\tau$ for high mass and low mass regions (entire region). Low mass $c\tau$ on the left and high mass $c\tau$ on the right.

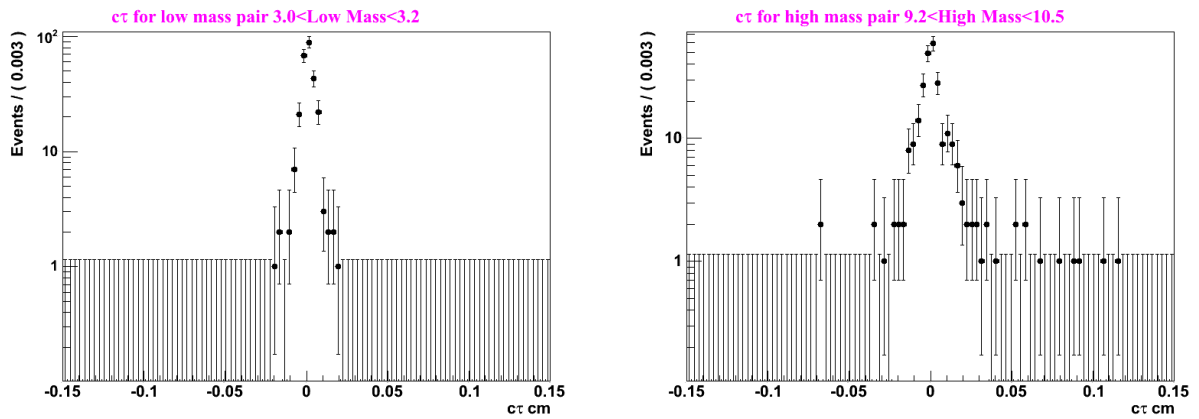


Figure 5.14: $c\tau$ for high mass and low mass central region. $c\tau$ for J/ψ region [3.0-3.2] on the left and for Υ region [9.2-10.5] on the right.

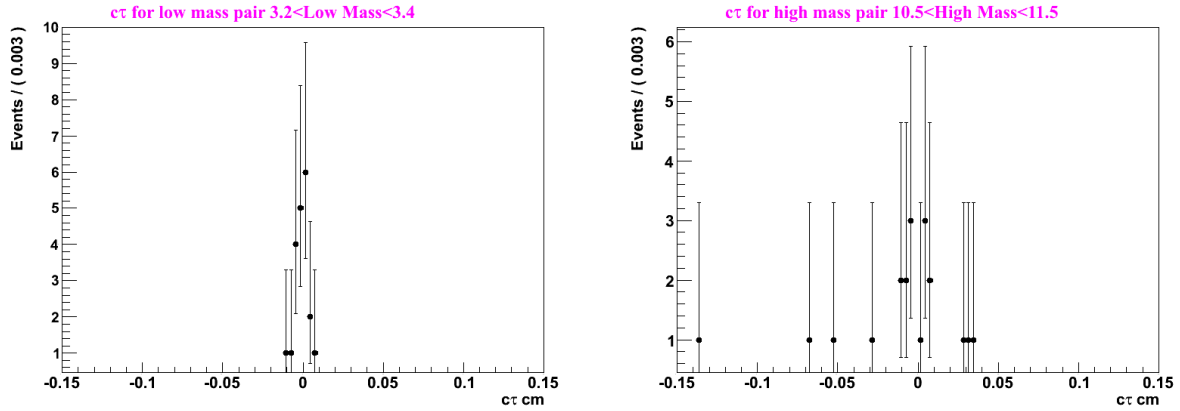


Figure 5.15: $c\tau$ for high mass and low mass sidebands. $c\tau$ for J/ψ sideband [3.2-3.4] on the left and for Y sideband [10.5-11.5] on the right.

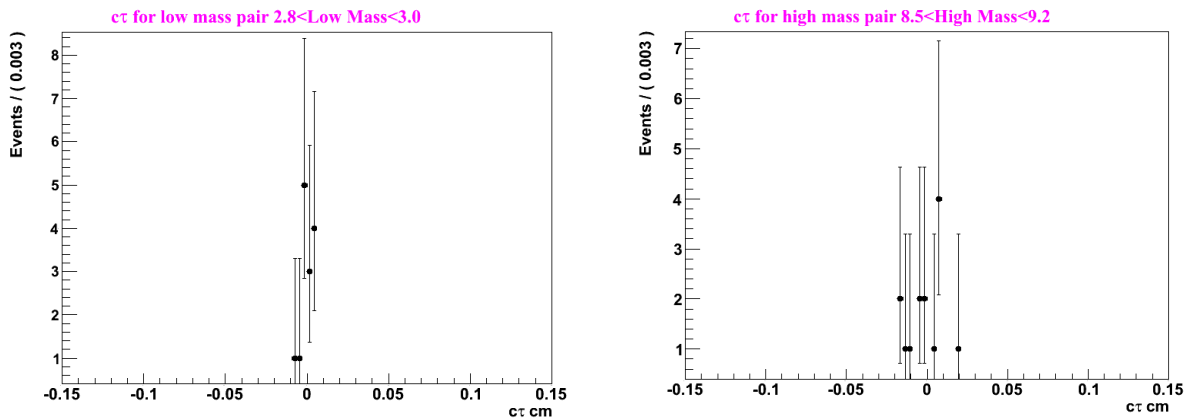


Figure 5.16: $c\tau$ for high mass and low mass sidebands. $c\tau$ for J/ψ sideband [2.8-3.0] on the left and for Y sideband [8.5-9.2] on the right.

5.7 Fit Validation

In order to validate the two-dimensional fit results, we checked the pull distributions from toy MC experiments. We generated 10,000 simulated samples from the probability density functions of all components and produced two-dimensional likelihood

fits from the toy Monte Carlo events. Results of the Toy experiments for 10,000 generated events are shown in Figure 5.17.

As can be seen in the figure, the signal yield pull distribution (top-left) is consistent with zero and signal width (sigma) is equal to 1. The distribution on top-right shows the signal yield distribution and this is equal to two-dimensional signal yield (64). The distribution on bottom-left shows the statistical uncertainty for the signal yield as returned by the toy experiments. As shown on the distribution, the statistical uncertainty is 13 which is almost the same as the statistical uncertainty of two-dimensional fit (14). Finally, the plot on bottom-right shows the negative log-likelihood distribution returned by the extended likelihood fit for the 10,000 toy experiments.

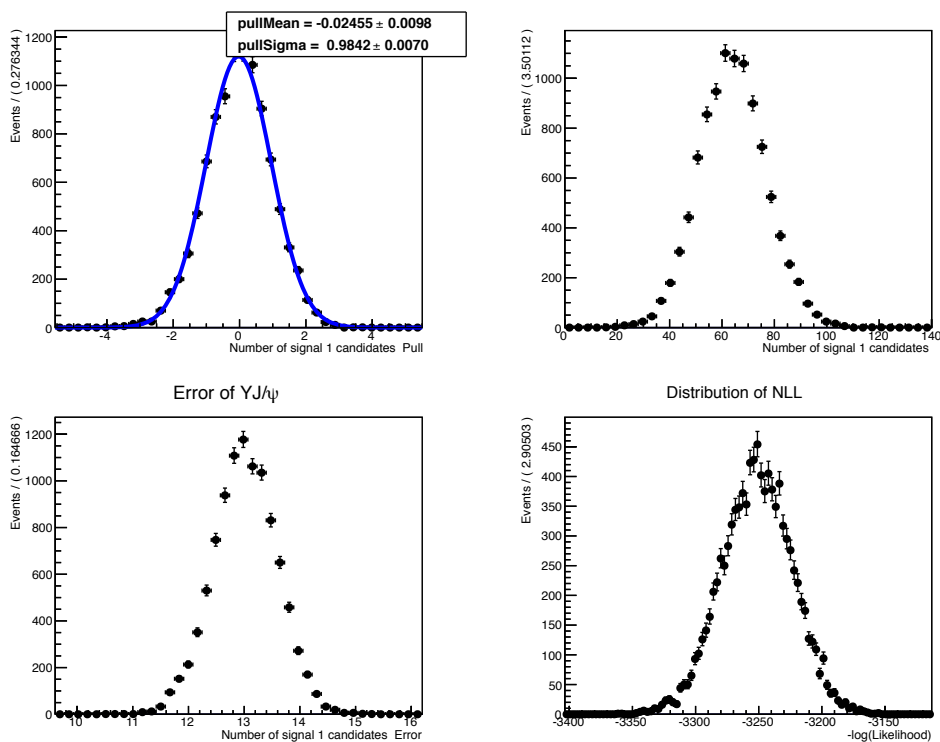


Figure 5.17: Results of Toy experiments for 10000 generated events.

5.8 Systematic Uncertainties

We have considered several sources of systematic uncertainties on the cross section measurement. The main systematic uncertainties come from signal and background pdf shapes, branching fractions, integrated luminosity, and polarization. We performed the fit using different signal and background pdf shapes: single Gaussian + Voigtian function on the signal and first order Chebyshev polynomial on the background, and double Crystal Ball with the mean and sigma allowed to float. In the analysis, we used double Crystal Ball with a fixed mean and sigma. Figure 5.18 shows the two-dimensional extended maximum likelihood fit of simultaneously produced $\Upsilon(1S)$ and J/ψ with a Gaussian + Voigtian function for the signal. The signal yield of this fit is 61, which is less than our analysis result, a two-dimensional fit using a double crystal ball with fixed mean and sigma. We calculated the uncertainty by taking relative difference of two signals yield. Figure 5.19 shows the two-dimensional extended maximum likelihood fit of simultaneously produced $\Upsilon(1S)$ and J/ψ with double crystal ball function with mean and sigma floating. The signal yield of this fit is 67 which is more than default fit yield. We tabulated the uncertainty due to the signal shape in Table 5.11. As can be seen in the table, the total systematic uncertainty due to pdf shape is 5%, which is the uncertainty for each variation on the signal pdf.

$$Uncertainty = \frac{64-61}{64} = 5\% \text{ (Gaussian + Voigtian PDF shape)} \quad (22)$$

$$Uncertainty = \frac{67-64}{64} = 5\% \text{ (Double Crystal Ball float mean and sigma)} \quad (23)$$

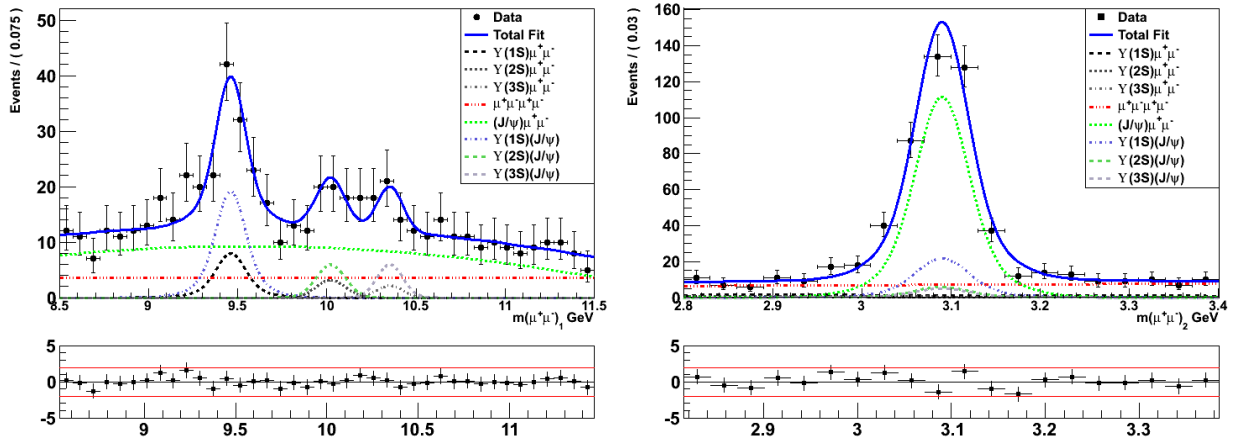


Figure 5.18: Two-dimensional maximum likelihood fit with Gaussian + Voigtian function. $Y(1S)$ (on the left) and J/ψ (on the right).

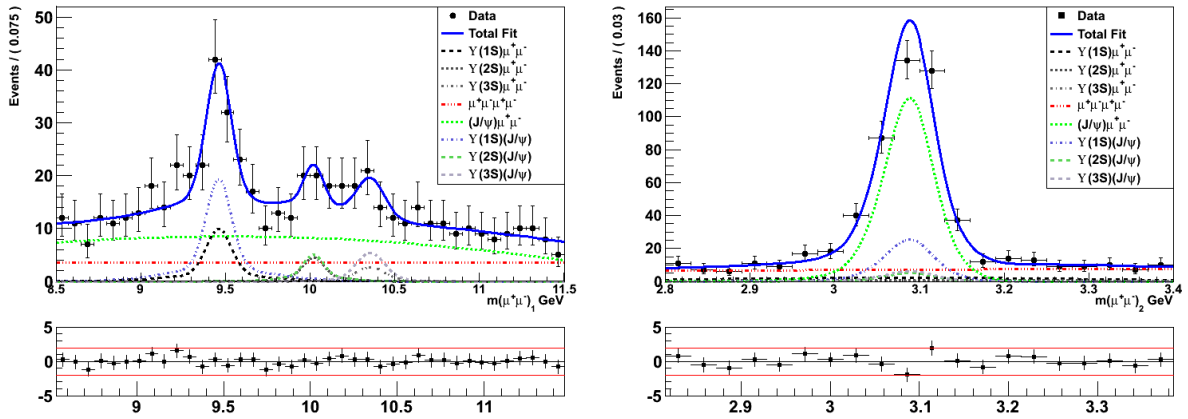
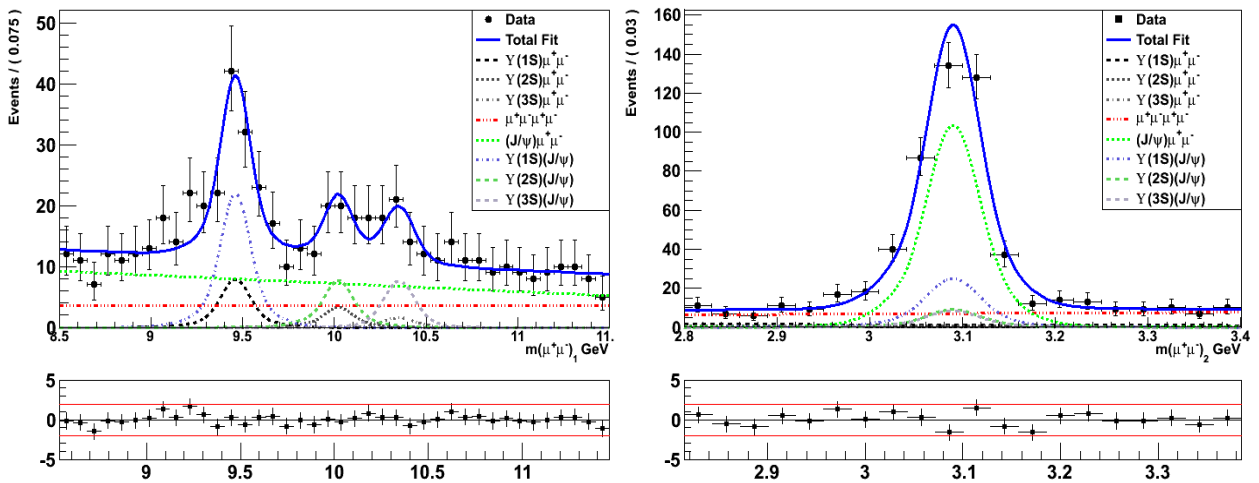


Figure 5.19: Two-dimensional maximum likelihood fit with double crystal ball function with mean and sigma floating. $Y(1S)$ (on the left) and J/ψ (on the right).

Table 5.11: Systematic uncertainty due to signal PDF shape.

PDF shape	Signal Yield	Systematic Error (%)
Double Crystal ball with fixed mean and sigma	64	Our analysis result
Single Gaussian + Voigtian	61	5
Double Crystal ball with float mean and sigma	67	5
Uncertainty of total PDF shape		5

**Figure 5.20:** Two-dimensional maximum likelihood fit with first order Chebyshev polynomial used on background. $Y(1S)$ (on the left) and J/ψ (on the right).

Next we looked at the uncertainty due to background pdf. Figure 5.20 shows the two-dimensional extended maximum likelihood fit for the background shape modeled by a first order Chebyshev polynomial. In this case, the signal yield is 70 (compared to 64), so the estimated systematic uncertainty due to the background shape is 9%. To find the

systematic uncertainty due to the branching fractions we used the PDG values [42]. The uncertainties on branching fractions for $Y \rightarrow \mu^+\mu^-$ and $J/\psi \rightarrow \mu^+\mu^-$ are 0.005% and 0.033% respectively. As they are very small compared to other uncertainties, they are negligible. The systematic uncertainty due to integrated luminosity is measured by CMS Collaboration in 2013 and found to be 2.5% [44].

To calculate the corrected signal yield, we assumed zero polarization. However, we must check the effect of polarization on the muon angular distribution. To check this effect, we looked at the acceptance with polarization using data embedding method as we did previously. We used equation 24 to look at the polarization.

$$I = 1 + \lambda \cos^2\theta \quad (24)$$

where θ is the angle between μ direction in the rest frame and $Y(1S)$ or J/ψ in the lab frame. Same as previous polarization studies [45,46] at the CMS, we changed the polarization parameter λ from -1 to 1 for extreme polarization scenarios. $\lambda = 0$ case corresponds to an isotropic decay while $\lambda = \pm 1$ corresponds to 100% longitudinal decay. For this reason, we select different values for λ as shown in Table 5.12. We used these values in the isotropic decay of $Y(1S)$ and J/ψ mesons for event-by-event acceptance as discussed in Section 5.4.3. Then, we corrected the data with the new acceptance values and found a new corrected yield. We found the systematic uncertainty due to polarization taking the relative difference of corrected yield with and without polarization. We assume that $Y(1S)$ and J/ψ mesons are unpolarized, so the cross section is expected to change from -23% to 16% for extreme polarization scenarios. Therefore, polarization has to be considered when interpreting the result.

Table 5.12: Polarization effect for different λ values.

λ_1	+1	0.5	-0.5	-1
λ_2	+1	0.5	-0.5	-1
Change (%)	16	7	-12	-23

This analysis is based on events that pass a 5% probability cut for the four-muon vertex. To assess what fraction of the long-lived dimuons survive the 5% cut, we generated MC events using Pythia8 MC generator with the physics process $H \rightarrow Y(1S) + J/\psi$. Since this process provides simultaneously produced $Y(1S)$ and J/ψ events, we can use a three-dimensional maximum likelihood fit on these events, and vary the lifetime of the J/ψ . First, we generated MC events with J/ψ has zero lifetime. Then, we changed J/ψ 's decay length to $450 \mu\text{m}$ since lifetime of B meson is $\sim 1.5 \text{ ps}$. We used a three-dimensional maximum likelihood fit on simultaneously produced $Y(1S)$ and J/ψ MC events with and without the four-muon vertex probability cut. We assign the vertex probability cut efficiency for the prompt dimuon component and the fraction of non-prompt components which could leak into prompt component. Table 5.13 shows the non-prompt signal yield of J/ψ with and without vertex probability cut. Figures 5.21, 5.22, 5.23, and 5.24 show three-dimensional fits for J/ψ decay length is $0 \mu\text{m}$ and $450 \mu\text{m}$ with and without four-muon vertex probability cut.

The MC yield for J/ψ has zero lifetime found to be 1.4×10^4 (with four-muon vertex probability cut) and 1.5×10^4 (without four-muon vertex probability cut). The vertex probability cut efficiency for prompt dimuon component can be defined taking the ratio of these yields as shown in equation below.

$$\text{Vertex probability cut efficiency for prompt dimuon component} = \frac{1.4 \times 10^4}{1.5 \times 10^4} = 93\% \quad (25)$$

Table 5.13: Signal yields of three-dimensional fit for simultaneously produced Y and J/ψ MC events. The J/ψ decay length is $450 \mu\text{m}$. Non-prompt signal yield was found with and without four-muon vertex probability cut.

Decay length (μm)	Non-prompt signal yield with 5% vertex probability cut	Non-prompt signal yield with no vertex probability cut
450 μm	1.6×10^3	1.3×10^4

Using signal yields shown in Table 5.13, the fractions of non-prompt components which leak into the prompt components for J/ψ decay length of $450 \mu\text{m}$ was measured as below:

$$J/\psi\text{'s decay length is } 450 \mu\text{m} = \frac{1.6 \times 10^3}{1.3 \times 10^4} = 12\% \quad (26)$$

We calculated the total systematic uncertainty by taking the sum in quadratic of each component given in Table 5.14.

Table 5.14: Total systematic uncertainty with quadratic sum of each component.

Component	Systematic Error (%)
Possible leakage of J/ψ from non-prompt component	12
Background PDF shape	9
Signal PDF shape	5
Integrated Luminosity	2.5
Total	16

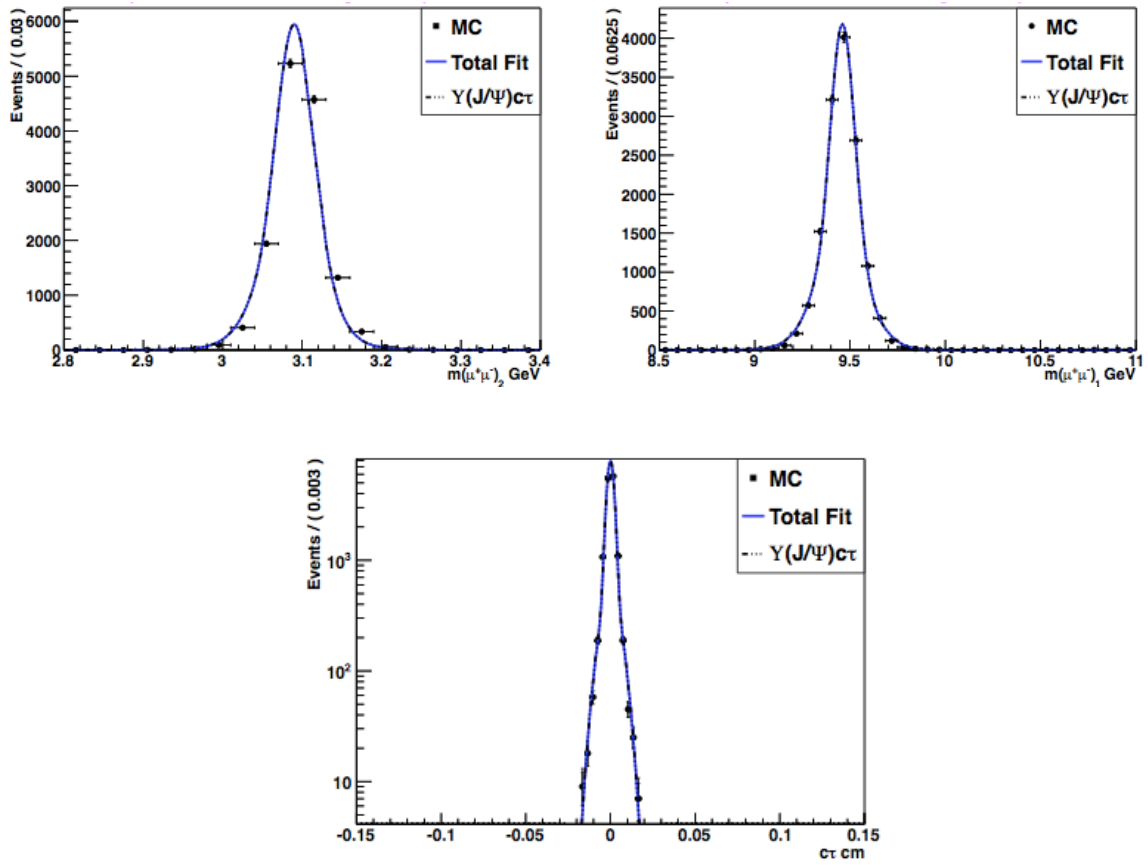


Figure 5.21: Three-dimensional fit on simultaneously produced $Y(1S)$ and J/ψ MC events. Top-left: J/ψ invariant mass MC events. Top-right: $Y(1S)$ invariant mass MC events. Bottom: $c\tau$ of J/ψ when J/ψ decay length is zero and the four-muon vertex probability is greater than 5%.

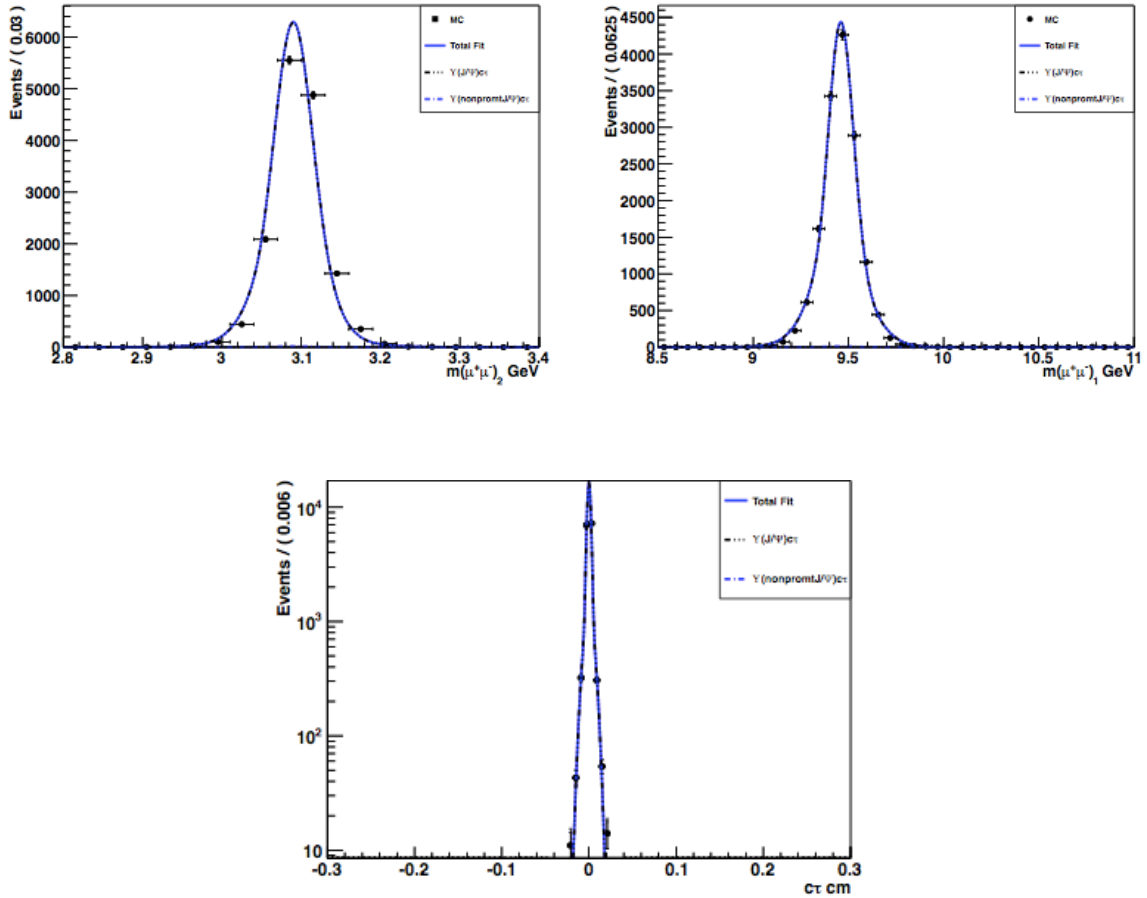


Figure 5.22: Three-dimensional fit on simultaneously produced $Y(1S)$ and J/ψ MC events. Top-left: J/ψ invariant mass MC events. Top-right: $Y(1S)$ invariant mass MC events. Bottom: $c\tau$ of J/ψ when J/ψ decay length is zero and no four-muon vertex probability cut.

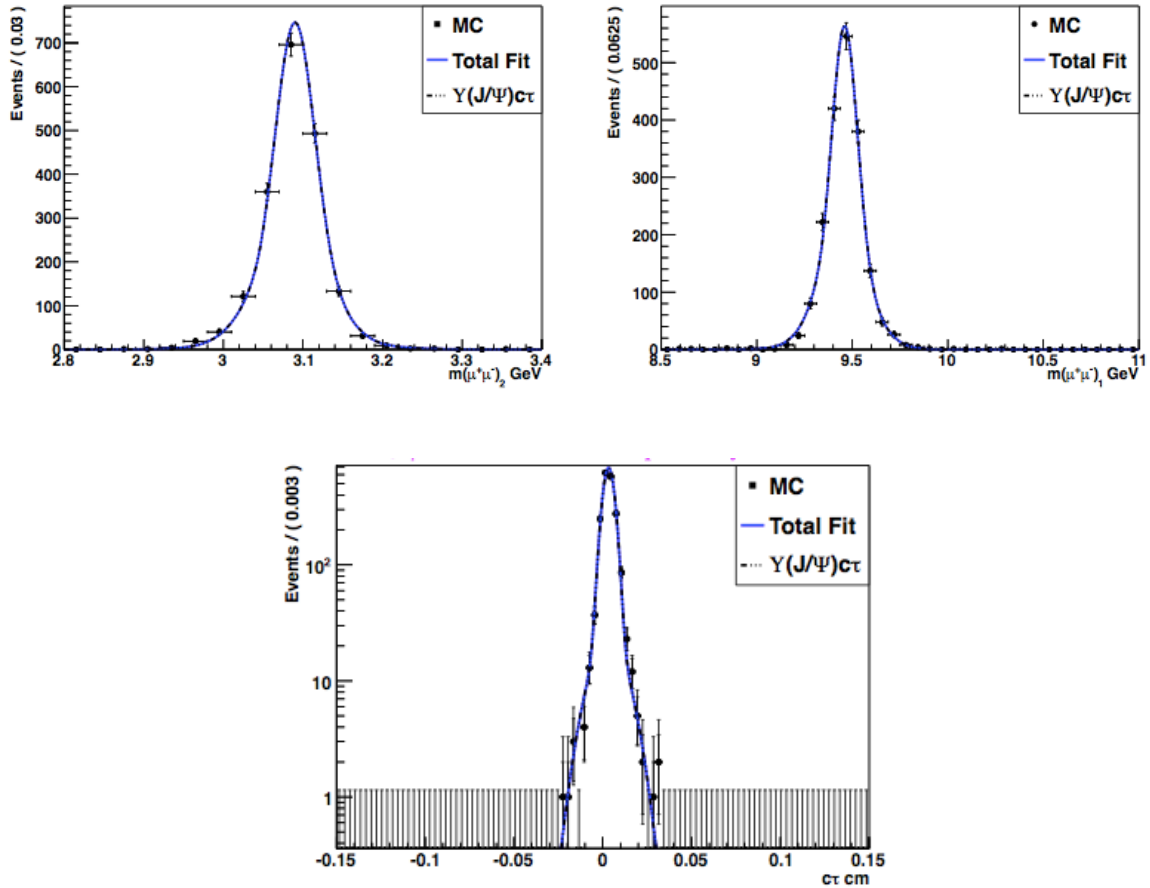


Figure 5.23: Three-dimensional fit on simultaneously produced $\Upsilon(1S)$ and J/ψ MC events. Top-left: J/ψ invariant mass MC events. Top-right: $\Upsilon(1S)$ invariant mass MC events. Bottom: $c\tau$ of J/ψ when J/ψ decay length is $450 \mu\text{m}$ and four muon vertex probability is greater than 5%.

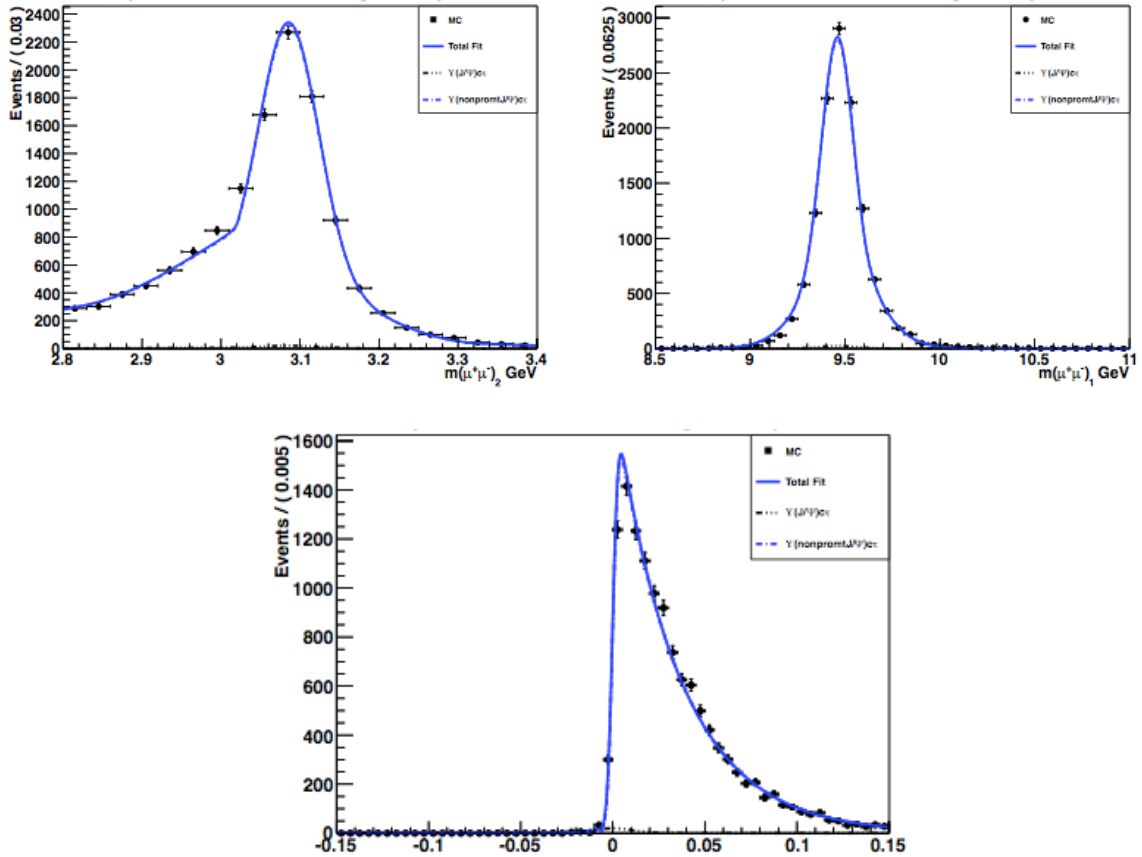


Figure 5.24: Three-dimensional fit on simultaneously produced $Y(1S)$ and J/ψ MC events. Top-left: J/ψ invariant mass MC events. Top-right: $Y(1S)$ invariant mass MC events. Bottom: $c\tau$ of J/ψ when J/ψ decay length is $450 \mu\text{m}$ and no four muon vertex probability cut.

5.9 Results

5.9.1 Cross Section Evaluation

In particle physics, the cross section defines the possibility of two particles colliding and reacting in a certain way. In this section, we will use the average acceptance and efficiency values to correct the two-dimensional signal yield. We found 44% average acceptance and 29% average efficiency using event-by-event acceptance and efficiency corrections as discussed in Section 5.4.3. The branching fraction of the $Y(1S)$ decays to

muon pairs is 2.48% [42] and branching fraction of the J/ψ decays to muon pairs is 5.961% [42]. Using these numerical values, we can calculate the cross section with the following equation.

$$\sigma(pp \rightarrow Y(1S) + J/\psi + X) = \frac{N_{Y(1S)+J/\psi}}{a \cdot \epsilon \cdot BF(Y(1S) \rightarrow \mu^+ \mu^-) \cdot BF(J/\psi \rightarrow \mu^+ \mu^-) \cdot L} = 16.5 \text{ pb}. \quad (27)$$

where:

- $N_{Y(1S)+J/\psi}$: Two-dimensional signal yield of $Y(1S) + J/\psi$.
- a : Numerical value of average acceptance.
- ϵ : Numerical value of average efficiency.
- BFs : Branching fraction of $Y(1S)$ and J/ψ mesons.
- L : Total effective luminosity which is calculated by PixelLumiCalc.py.

Assuming $Y(1S)$ and J/ψ candidates are un-polarized, the total cross section in the defined fiducial region, $|y| < 2.0$, was found as below with the statistical and systematical errors.

$$\sigma = 16.5 \pm 3.6(stat) \pm 2.6(syst) \text{ pb}. \quad (28)$$

As a cross-check, we can use equation 3 in Section 4.1 to estimate the $Y(1S) + J/\psi$ cross section from the single J/ψ and single $Y(1S)$ cross section measurements at the CMS assuming they are produced uncorrelated (DPS). To define the DPS cross section of two particles in a model-independent way, we simply get the product of two single particles with the SPS cross section normalized by an effective cross section as shown below:

$$\sigma_{DPS}^{xy} = \frac{m}{2} \frac{\sigma_{SPS}^x \sigma_{SPS}^y}{\sigma_{eff}} \quad (29)$$

In this equation m is a combinatorial factor. For indistinguishable final states $m = 1$ and for distinguishable final states $m = 2$. Since we have distinguishable final states, m must be 2 for our case. Since there are not any public results for the cross section of single Υ and single J/ψ at 8 TeV, we will use the cross section results for 7 TeV center-of-mass energy. The cross section of single $\Upsilon(1S)$ at 7 TeV is 340 nb [47] and the cross section of single J/ψ at 7 TeV is 1200 nb [48]. The numerical value of effective cross section (σ_{eff}) can be obtained as a factor of minbias in an inelastic proton-proton collision at LHC [31,49]. The estimated cross section ($\sigma_{DPS(\Upsilon(1S)+J/\psi)}$) can be found as follow:

$$\sigma_{DPS}^{\Upsilon(1S)+J/\psi} = \frac{m (340 \times 1200) nb}{2 \times 51 mb} = 8 pb \quad (30)$$

As can be seen, this estimated cross section is close to our measured cross section ($16.5 \pm 3.6(stat) \pm 2.6(syst) pb$).

CHAPTER 6

CMS FORWARD PIXEL PHASE I UPGRADE SENSOR STUDY

6.1 The CMS Pixel Detector

Silicon (Si), an element with atomic number 14, is a simple semiconductor material. In order to modulate the electrical conductivity of a semi-conductor, an intentional doping introduces impurities into a pure semi-conductor. In doping, a small amount of impurity is added into a Si crystal. Boron (B) and Phosphorus (P) are the generally used elements to create p and n doping in Si. For an n-doping, the doping occur with an element that has 5 electrons in the last orbit [50]. These elements are P, As, Sb. Here the 5th valance electron is weakly bound. As shown in Figure 6.1 (left), P has an extra electron and this electron can use the holes in neighbor atoms and modulates an electrical conductivity. Here, the doping atom is called a donor. For p-doping, the doping occurs with an element with three electrons in the last orbit [50]. These elements are B, Al, Ga. There is a lack of electron, *ie.*, one valance bond remains open and the bond attracts electrons from the neighbor atoms. Here, the doping atom is called an acceptor. Figure 6.1 (right) shows the chemical bonds of B with Si [51].

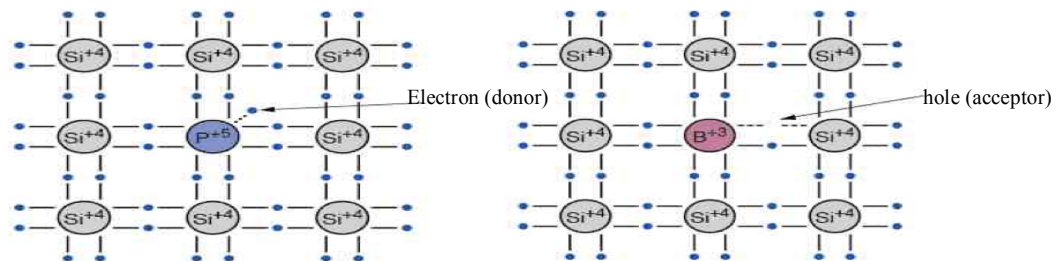


Figure 6.1: An example of an n-doping (left) and p-doping (right) [51].

A silicon pixel sensor is a p-n junction semi-conductor material [52,53]. A p-n junction material is the connection of p-type and n-type materials. In a p-n junction material, the n region carries more electrons (negative charge) while the p region carries more holes (positive charge). A p-n junction material allows the current to flow in one direction. The voltage is used on the p-side of the junction causing electrons to pass to the p-side leaving holes in the n-side. Increasing voltage allows more electrons to pass to the p-side until positive and negative charges balance, creating a depletion region. The voltage at which the depletion region was created is called the depletion voltage [53]. Figure 6.2 shows a sample for a p-n junction semi-conductor. As can be seen, a depletion region (blue and red regions) was created with the increasing voltage. If a voltage V is applied on a p-n junction material, the total current that flows through the junction is defined with the equation below [51].

$$I = I_0 \cdot \left[\exp\left(\frac{eV}{kT}\right) - 1 \right] \quad (31)$$

where I_0 is the saturation reverse current.

When a semi-conductor material is reverse biased, this will cause a current that is called the reverse saturation current [54]. This current is dominated by thermally generated electron and hole pairs and the pairs cannot recombine and are separated due to electric field. Therefore, a current, which is called leakage current, will leak due to the drift of electrons and holes [51]. This leakage current can result noise inside the detector. In order to limit the noise induced by the leakage current, the sensor temperature is kept below -5°C [15]. The maximum reverse bias that can be applied to a p-n junction is called breakdown voltage. A further increase in voltage will cause a rapid increase of the current [54]. The breakdown happens mainly because of an avalanche effect.

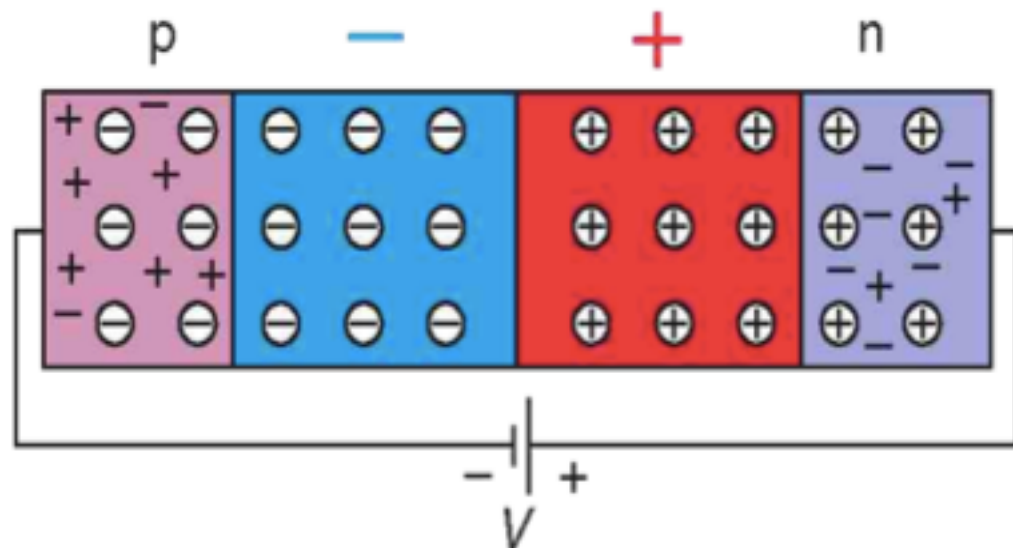


Figure 6.2: A sample for how a p-n junction semi-conductor works [51].

The pixel system of the CMS detector measures up to three hits per track, which play a role in identifying secondary vertices. This allows tagging of long-lived particles such as b-quarks which are important in searching for Higgs or SUSY particles [1]. In addition, it can be used to distinguish long-lived particles from a large background of light quark and gluon jets [15].

At the time of the original CMS Technical Proposal, three different materials were proposed to use for the pixel sensors. These were diamond, gallium arsenide (GaAs), and silicon. Because GaAs and diamond were believed to keep their radiation performance after intense neutron radiation, they are considered to be radiation hard. To check capability of these materials to be used for pixel detector, many detailed irradiation studies have been performed. Results of these studies showed that GaAs can have significant and unacceptable signal loss since it allows fluences of neutrons and it is sensitive to charged hadrons. Diamond resisted at least 10^{15} pion/cm², so using diamond

as a base material would provide an advantage because of its radiation hardness. However, replacing damaged readout chips would be expensive if diamond would be considered as a base material. In order to take advantage of the radiation hardness of diamond, a procedure must be found to replace damaged readout chips on the detectors. It is much less expensive to replace silicon; for this reason, silicon was chosen as the baseline material for the CMS pixel system [15]. Silicon experiences an increasing bulk leakage current, which leads to high noise and power dissipation and increases depletion voltage due to an effective p-doping. Proton-proton collisions inside the CMS detector lead to radiation damage in the silicon. This damage causes trapping of charges, which can manifest itself as a change in the doping. The leakage current can be reduced by keeping the detectors at appropriate temperatures below 0°C.

Figure 2.12, in Chapter 2 Section 2.2.4, shows a view of the CMS pixel detector. As can be seen in the figure, it has three-barrel layers and two end-cap disks (two disks on either side of the interaction point) [1]. The barrel layers have a diameter of 4.4, 7.3, 10.2 cm respectively. All three layers consist of 48 million pixels, 11520 ROCs, and 1120 readout links [1]. Two disks are located on each side of the pixel detector. The distance between the disks and interaction point is about ± 34.5 , ± 46.5 cm [4]. The disks include 18 million pixels, 4320 ROCs, and 192 Readout links [1].

Figure 6.3 shows an overall view of the CMS detector. The pixel detector is located close to the beam interaction point and this is subject to a very harsh radiation environment. This radiation environment causes damage to the pixel sensors and limits their lifetime. The radiation environment around the interaction point will reduce the performance and lifetime of the sensors.

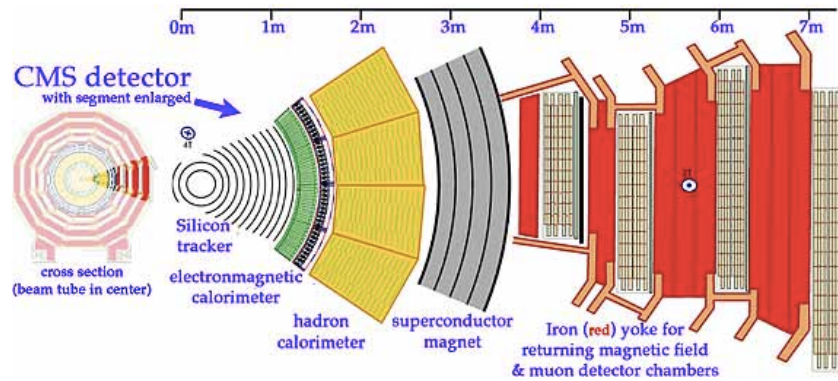


Figure 6.3: A view of CMS detector, Silicon detector (tracker) is on the left, near the interaction point.

Silicon sensors have n-pixels on an n-type substrate, which leads to a double sided processing that results in yield issues for the thin wafers that are used. The sensors are $250\ \mu\text{m}$ thick and wafers are thinned to this thickness before processing [15]. Figure 6.4 shows a picture of silicon sensor on the CMS pixel detector. The n-side of a wafer consists of charge collecting pixels that are covered by n-implants, grounded with readout chips. The p-side is the back-side of a wafer and this side of the wafer has several guard rings and these guard rings drop bias voltage to readout chip potential preventing any possible breakdown [15].

The readout chips of the pixel detector are the most expensive part of the detector. For this reason, sensor testing is done before sensors are attached to the readout chips. The most common method for testing sensors is to measure the IV (current & voltage) and CV (capacitance & voltage) curves.

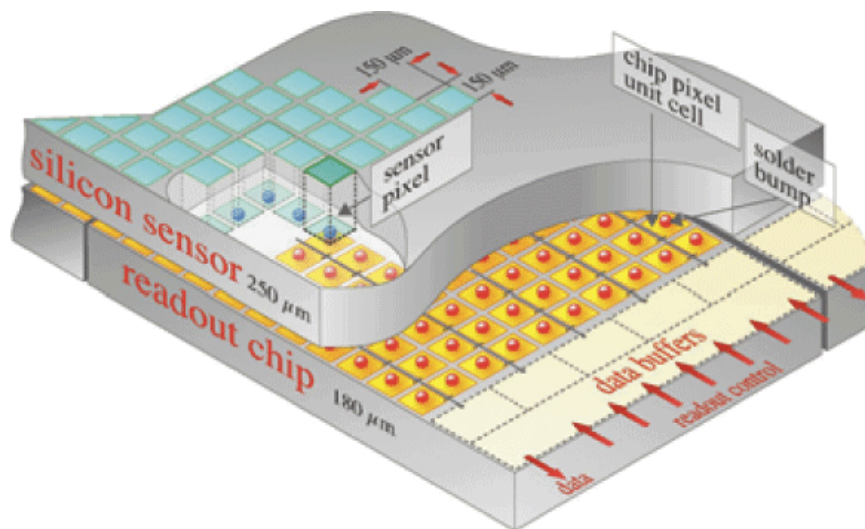


Figure 6.4: A silicon pixel detector that shows sensors and readout chips [15].

6.2 Quality Control on First Production Sensor Wafers

Due to the harsh radiation environment, the silicon sensors of the CMS Pixels Detector need to be replaced from time to time. The goal of the Phase 1 upgrade is to have a sensor design with improved radiation performance. For the next phase of LHC operations, a silicon sensor must resist at least an integrated luminosity of 300 fb^{-1} . The upgraded pixel detector will consist of four barrels layers and three disks on either side of the interaction point [1]. The barrels of the upgraded pixel will consist of four layers in the lengths of 3.9 cm and 16 cm from the innermost layer to outermost layer [1]. The barrels will also include 120 modules with 80 million pixels. In order to provide an easy replacement, the three pixel disks will be located on each side of the barrel with two concentric rings [1]. In order to replace with the old silicon sensors, new silicon wafers were fabricated by Sintef. We purpose to check the capability of these wafers to be used for the forward pixel system upgrade.

The foundation of scientific and industrial research (Sintef), one of the largest and independent research organization, was established at the Norwegian Institute of Technology in Trondheim. It was founded in 1950 and involved in research and development activities and supports more than 2000 companies all over the world. The silicon wafers were fabricated by this company and we tested these wafers at the Silicon Detector Facility center (SiDet), which is located at Fermi National Accelerator Laboratory and is used for research and development (R&D) studies. It has two large clean rooms each of which is about 5000 ft².

Figure 6.5 shows the p-side of a wafer. A wafer has eight 2x8 sensors in the center; six 1x1 sensors around; four slim edge sensors, and a number of diodes and other structures. We used one of the clean rooms at SiDet to test silicon wafers. Our test setup consists of a Summit 12000 AP probe station. There are two needles and a movable chuck on this probe station. The wafer goes into the center of the probe station using the movable chuck. After this process, we let two needles contact the wafer's sensor, one on the active area of the sensor and another on the guardring. The connection between the wafer and needles measures the signal from the wafer. Figure 6.6 shows a picture of the test setup.



Figure 6.5: Sintef 2x8 sensor numbering (on the left). A picture of a wafer (on the right).

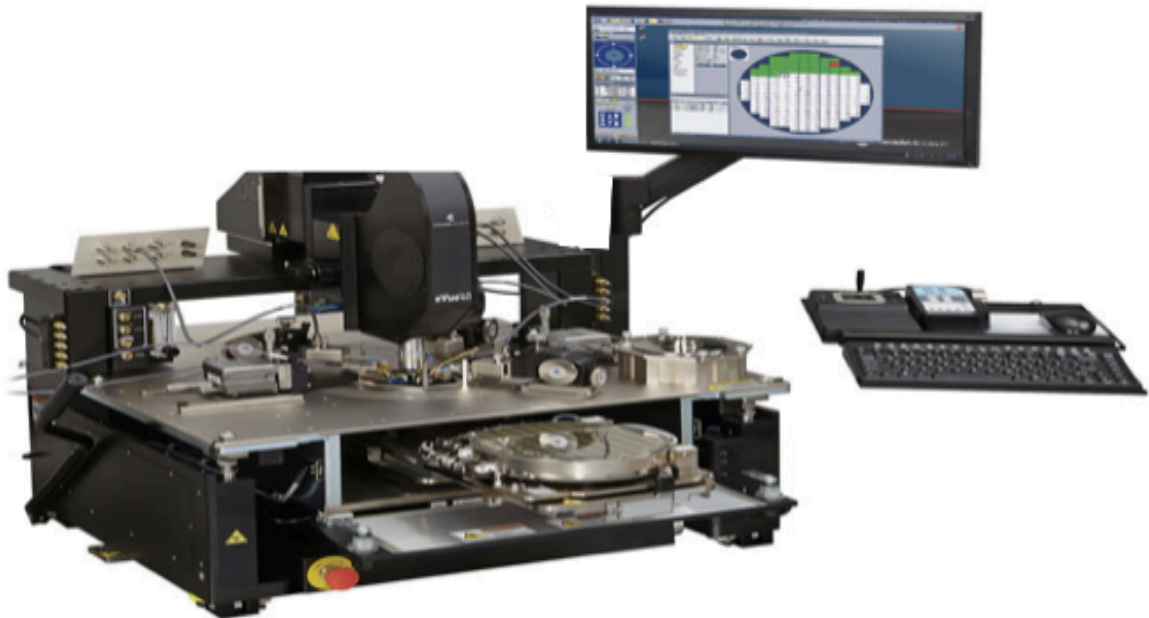


Figure 6.6: Wafer test setup. Probe station to test silicon wafers and computer to view IV and CV curves and control the probe station.

After the wafer is centered into the probe station, a contact check is done by the program. The Summit 12000 AP is connected to a computer that controls it, allows us to view IV and CV curves and records the results from the tests. The IV and CV curves are measured using two ammeters and a LCR capacitance meter; connections are shown in Figure 6.7. We are then ready to test the wafers.

We received about 20-30 wafers in each shipment from Sintef, with four shipments for a total of 120 wafers. Before testing, we did a visual inspection of the wafers and cleaned them. In order to minimize damage to the wafers, we chose only five wafers to test from each shipment. Sintef uses letters to specify batches and we convert these to numerical values as below:

- 9xx A batch (prototype wafers)

- 0xx B batch (production wafer)
- 1xx C batch (production wafers)
- 2xx D batch (production wafers)

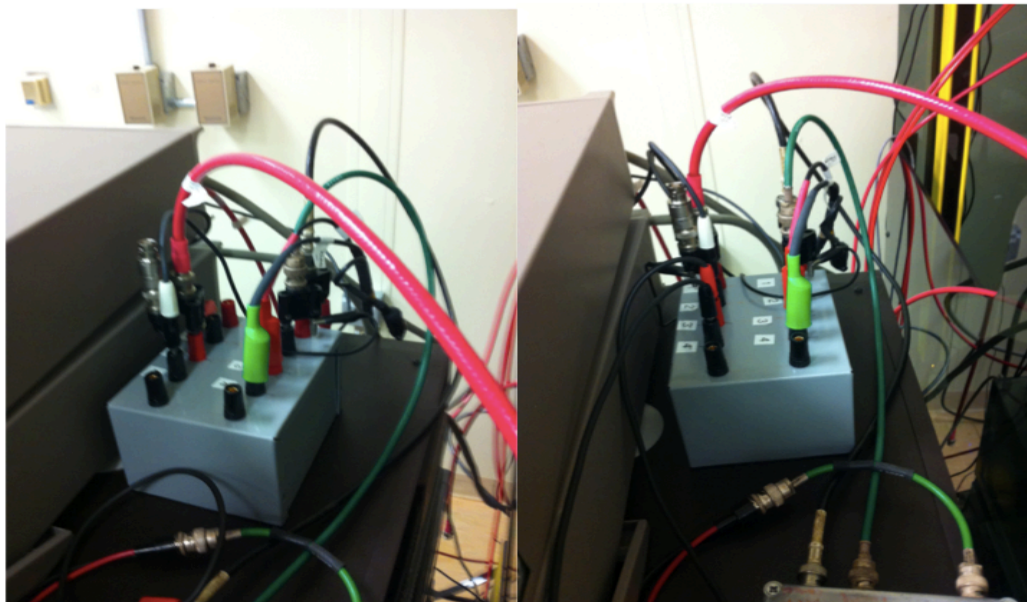


Figure 6.7: IV and CV connections to the probe station. (IV on the left and CV on the right).

On March 27th, 2015 we received the first production shipment of 21 B type production wafers. We did IV and CV measurements on five of these wafers in order to cross check the Sintef measurements. We checked all eight 2x8 sensors on these wafers. Then, we compared our results with Sintef results. Our criteria for a sensor to be considered good (useful for building modules) are as follows:

- I at 100 V must be smaller than $1 \mu A$.
- I at 150 V must be smaller than $2xI@100 V$

where I is total current (active area + guard ring currents).

We selected these criteria partly because we expect the full depletion voltage to be around 65 V before irradiation. As the sensors become irradiated the full depletion voltages will increase, but the breakdown point also tends to move to higher voltages.

Figure 6.8 shows the results of the IV measurement of wafer 002 from the first shipment where the dashed lines are Sintef results and the solid lines are FNAL results. As can be seen in the figure, the FNAL-measured depletion voltage is about 65 V. In addition, good sensors have about 6-7 nA/cm² leakage current when fully depleted. All the sensors on this wafer are consistent with the acceptance criteria. The difference between the two measurements may reflect slightly different room temperatures. In addition, we place the wafer directly on the chuck whereas Sintef uses a conductive rubber.

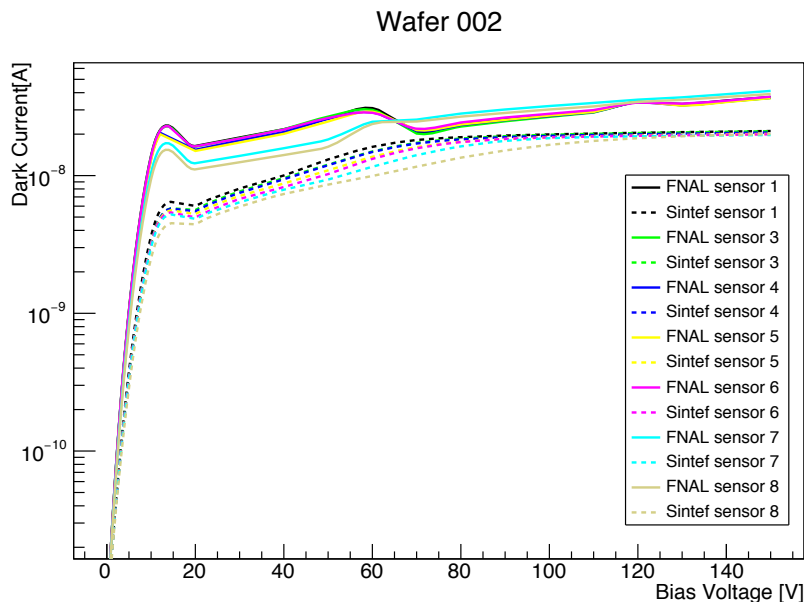


Figure 6.8: Wafer 002, sensors that are good both for FNAL and Sintef.

The IV curves for good sensors (according to both FNAL and Sintef) in this shipment are shown in Figure 6.9. As can be seen in the figure, the measurements for all sensors fit with our criteria and there is little difference between Sintef results and our results. We did find one sensor that passed Sintef test but failed by our criteria. As can be seen in Figure 6.10, this sensor passed the first test (I at 100 V is smaller than $1 \mu A$), but failed the second test (I at 150 V must be smaller than $2 \times I @ 100$ V). As shown in the figure, the slope is a little bit high between 100 V and 150 V. There are also some sensors that both FNAL and Sintef tests conclude are bad; there were 4 sensors found in the first set that cannot be used for building modules.

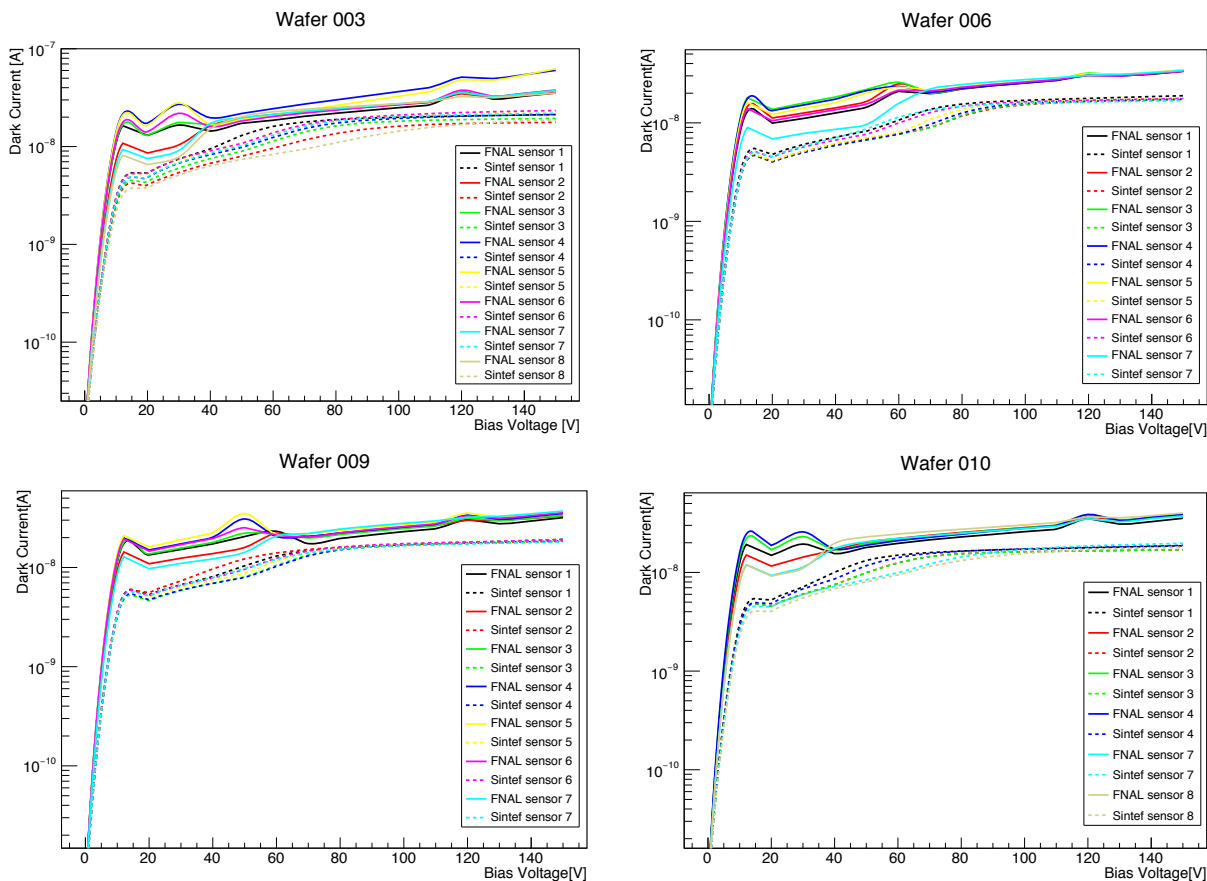


Figure 6.9: Wafers: 003,006,009,010, sensors that are good both for FNAL and Sintef.

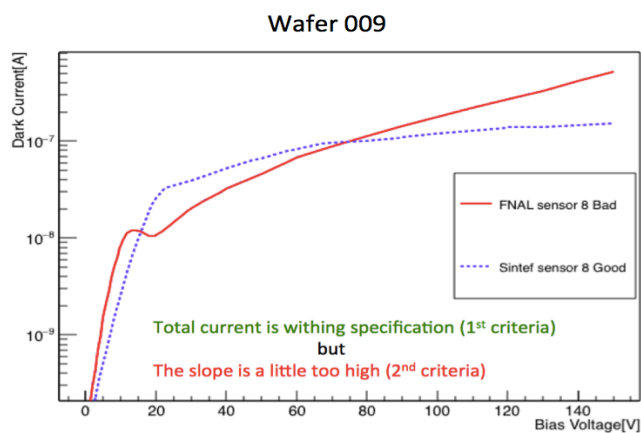


Figure 6.10: Sensor that fails FNAL testing, but pass Sintef testing.

In addition to IV measurements, we also did CV (capacitance-voltage) measurements on one diode and one sensor for each production wafer that we tested. The CV measurement also showed that the depletion voltage is what we expected (60-70 V). Figure 6.11 shows the CV measurement for wafer 009. In this figure, we normalized capacitance to 1 after full depletion and we saw that the depletion voltage was the same both for Sintef and FNAL results. Figure 6.12 shows the Fermilab CV measurements of the other wafers.

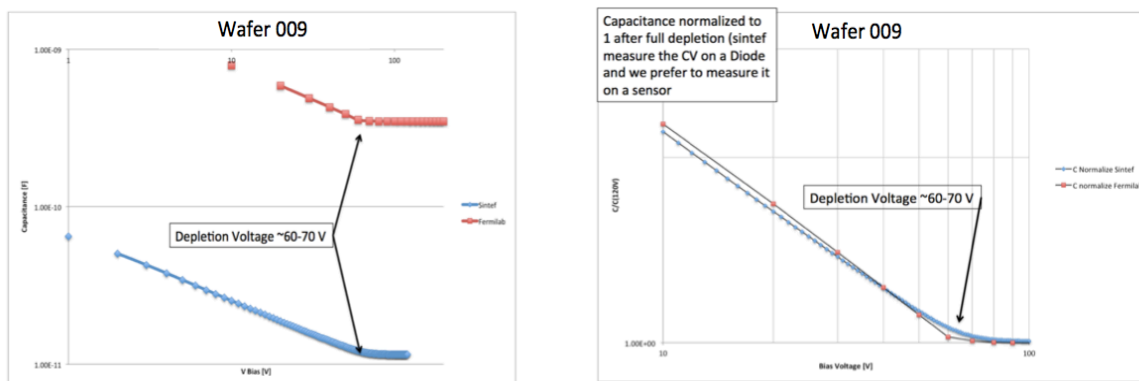


Figure 6.11: CV measurement on wafer 009 (on the left). CV measurement with capacitance normalized to 1 after full depletion (on the right).

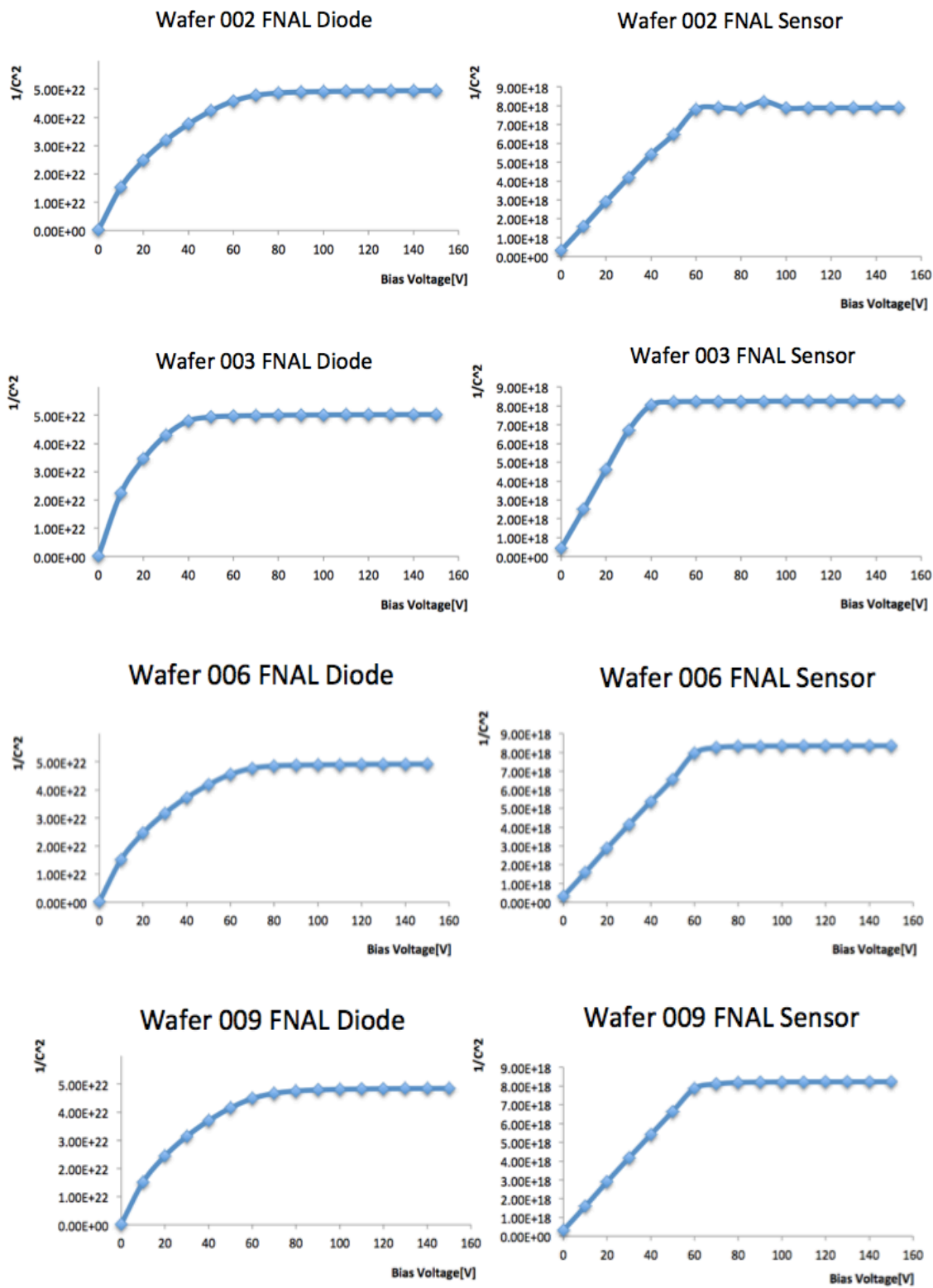


Figure 6.12: CV measurement on one diode (left) and one sensor (right) for FNAL tests.

In addition to the IV and CV curves, we also looked at breakdown voltage, which is the reverse bias voltage at the point which the currents start to rise rapidly. FNAL uses the voltage at $50 \mu A$ as the breakdown voltage although Sintef uses the voltage at $1 \mu A$ as the breakdown voltage. For a reasonable comparison, we preferred to take the voltage at $1 \mu A$ as the breakdown voltage for this set of production wafers. Figure 6.13 shows the breakdown voltage comparison between FNAL and Sintef.

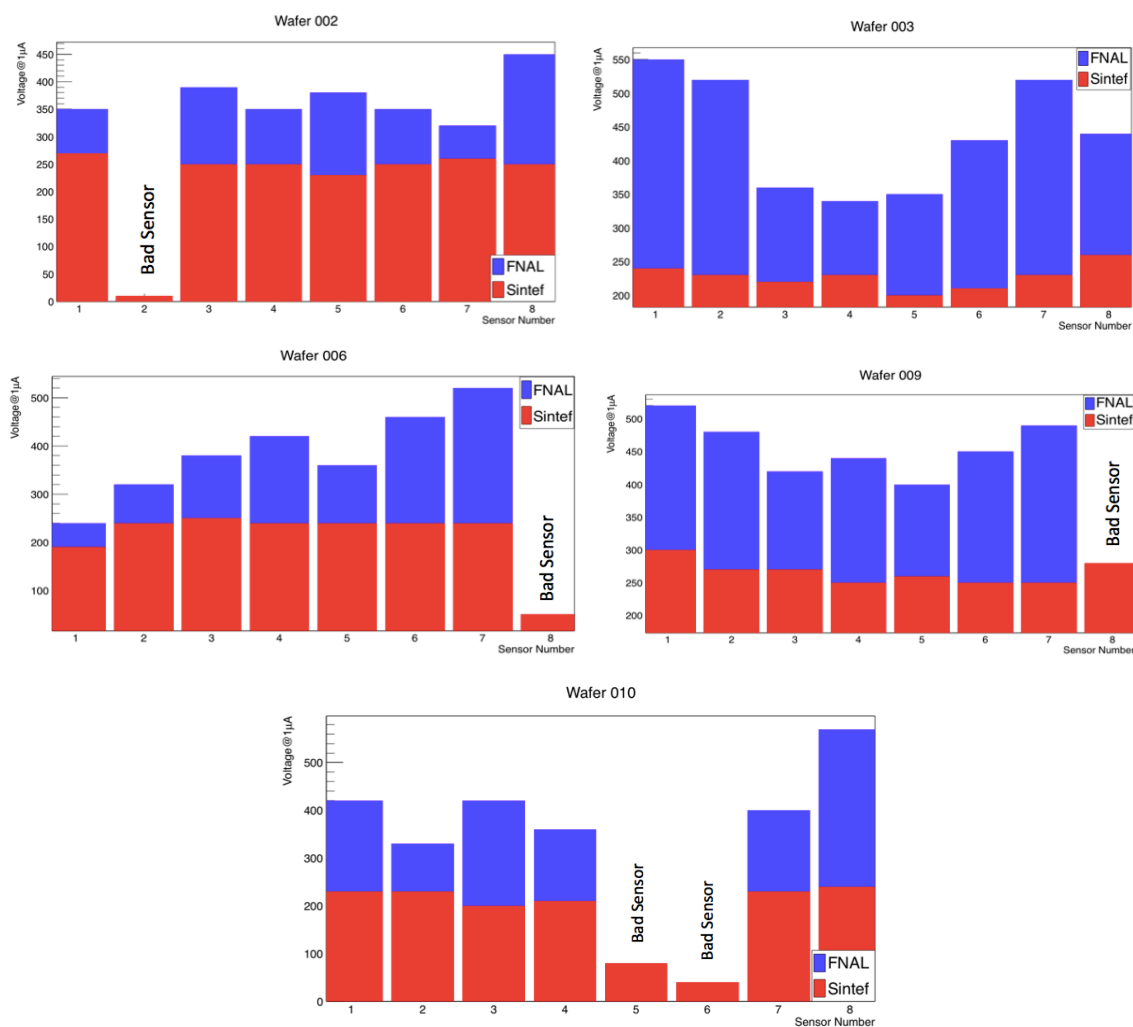


Figure 6.13: Comparison of breakdown voltages of sensors for FNAL and Sintef results.

We received 24 more B-type production wafers on May 29th, 2015 and made the same measurements as for the previous shipment. We chose five wafers based on the Sintef results. These were 014, 016, 018, 024 and 028. An IV measurement was done for all 40 sensors and CV measurements were made for the first sensor and one diode of each wafers. Figure 6.14 shows IV curves for the sensors that passed our criteria both for FNAL and Sintef.

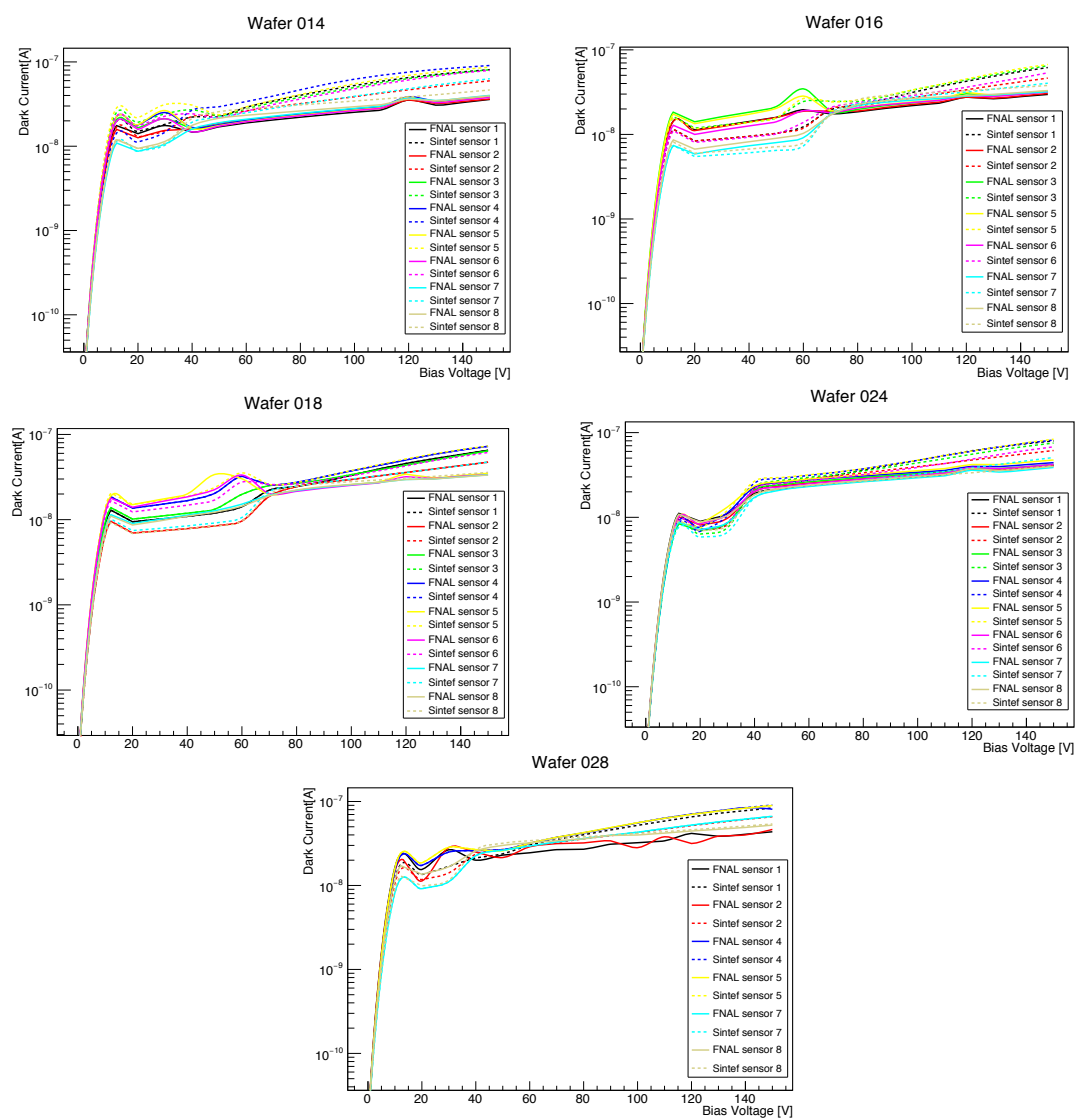


Figure 6.14: IV curves of the good sensors for the shipment on May 29th.

We found one production sensor that passed FNAL tests but failed by Sintef criteria; sensor 3 of wafer 028. Figure 6.15 shows the IV curve for this production sensor. As shown in the figure, the slope is a little steeper for Sintef's data between 100 V and 150 V. This shows that this sensor fulfills our first criteria ($I@100V < 1 \mu A$), but it is not consistent (according to Sintef data) with the second criteria ($I@150V < 2*(I@100V)$). In addition, the breakdown voltage for this sensor is 250 V ($I@50 \mu A$) for FNAL. However, it is 160 V ($I@1 \mu A$) for Sintef. Figure 6.16 shows the breakdown voltages of five production wafers for this shipment.

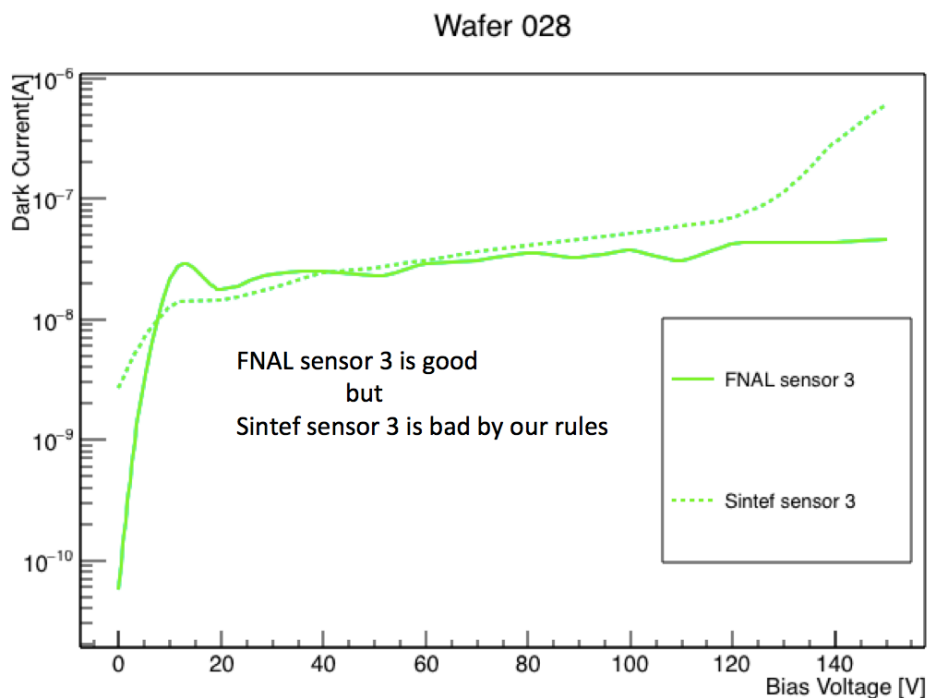


Figure 6.15: Inconsistent measurement between FNAL and Sintef. Sensor 3 is bad for Sintef, but it is good for FNAL by our criteria.

We also looked at the CV curve of these five wafers as we did for the previous shipment. We examined the CV curves of the first sensor of each wafer although Sintef only did the CV measurement of one diode for each wafer. As shown in Figure 6.17, the depletion voltage is around 60-70 V, which is as predicted. This result also shows that the depletion voltage is as expected for the diodes and sensors.

Our results for this shipment show only one bad sensor for the wafer we measured. Combining with the first set of measurements we have a 2.5% discrepancy with Sintef for this shipment. The leakage current at 150 V is also about 6-7 nA/cm².

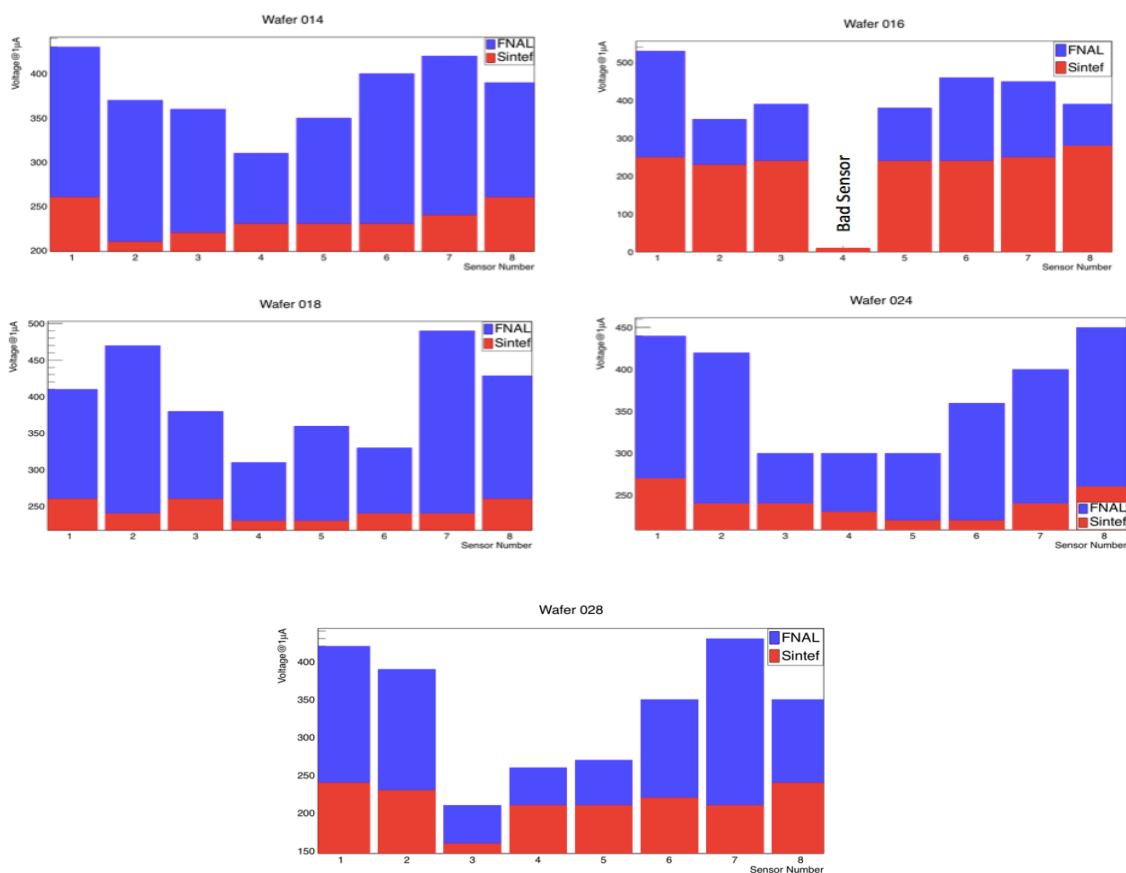


Figure 6.16: Breakdown voltage comparison for five production wafers from May 29th shipment.

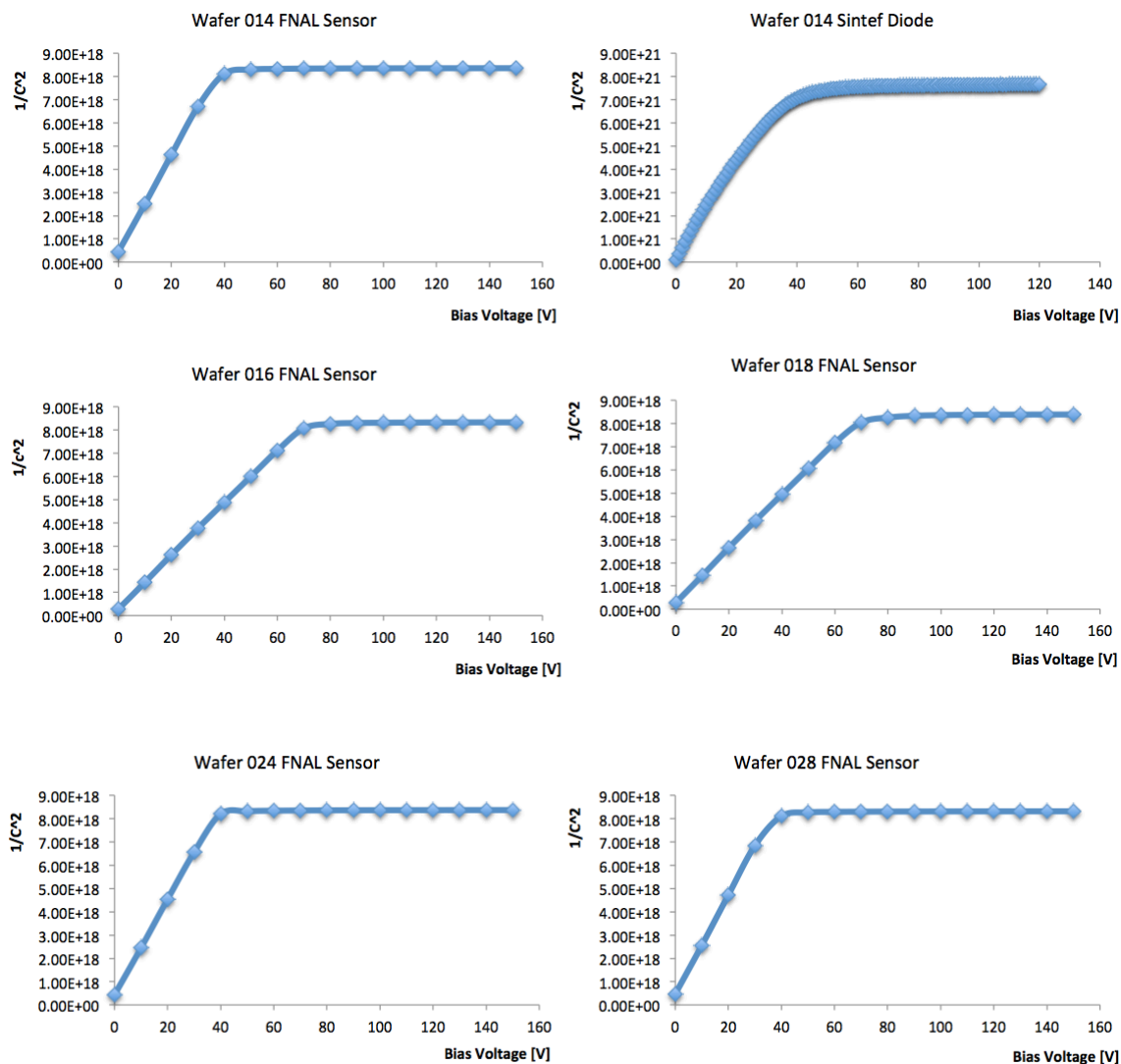


Figure 6.17: CV curves of FNAL and Sintef, Sintef measures CV on one diode and FNAL measures CV on the first sensor of each wafer.

In the second shipment, we chose five more wafers (10 in total) in order to fully test the quality of wafers type. These were 022, 106, 109, 120 and 139. As we described previously, the wafers that starts with 0 are B-batch wafers and the wafers that start with 1 are C-batch wafers. These are from two different production runs and there may be some differences between them. Therefore, this new selection includes both types for

comparison. Figure 6.18 shows the good sensors from the wafers in the B and C batches. As shown in the figure, all the sensors meet our criteria, and our results are close to the Sintef results. In addition, we agree on the 60-70 V full depletion voltage.

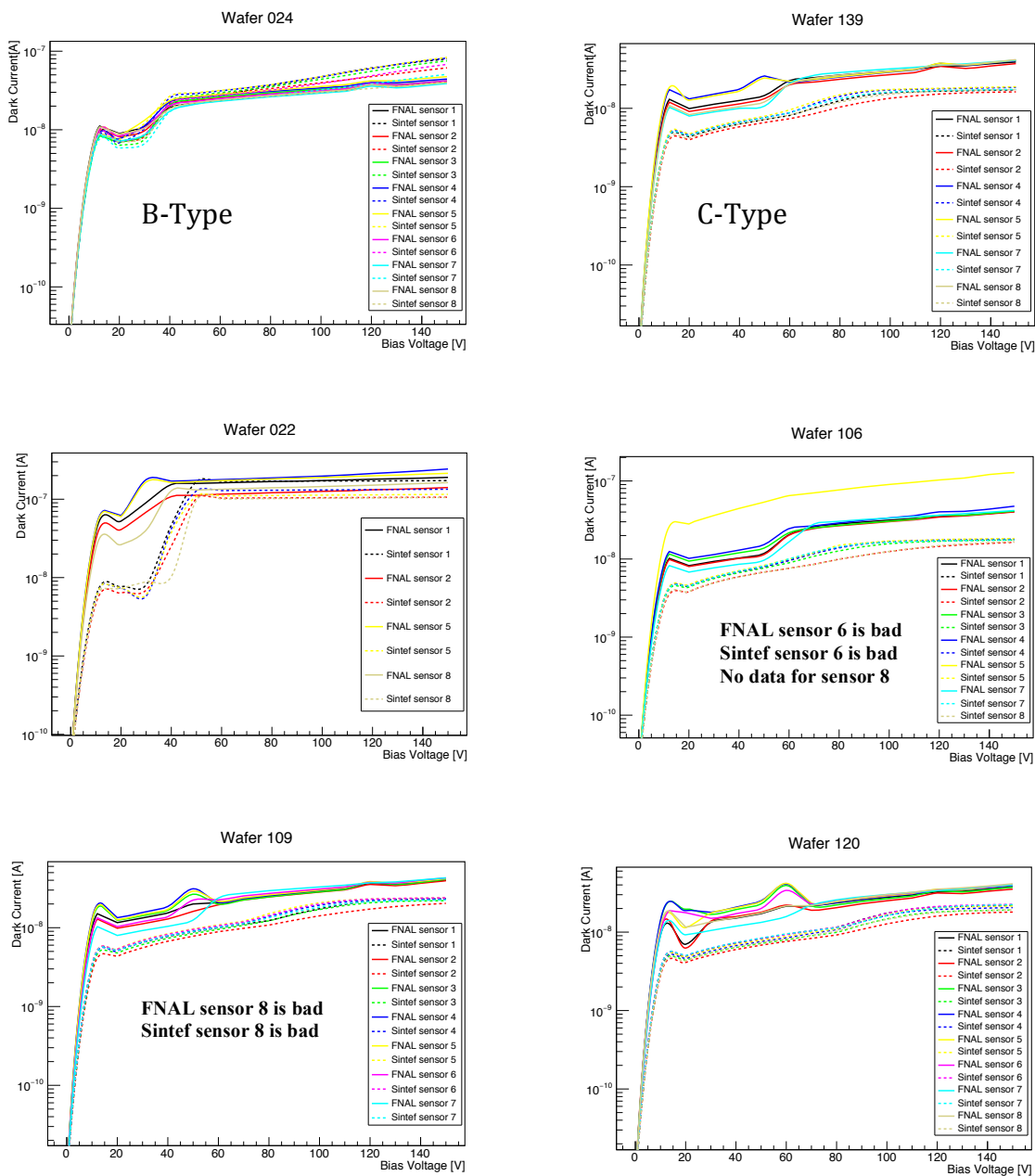


Figure 6.18: IV curves for good sensors of production wafers 022, 106, 109, 120 and 139. B-type and C-type comparison was made between wafers 024 and 139.

According to this measurement, there are also some sensors that passed FNAL criteria but failed Sintef test and conversely some sensors that failed the FNAL criteria but passed the Sintef test. Sensors 3 and 4 of wafer 022 failed by FNAL criteria but passed Sintef test. As shown in Figure 6.19 (left) both sensors are consistent with the first rule; however they disagree for the second rule. There is one sensor that passed the FNAL criteria but failed the Sintef test. This is sensor 7 of wafer 022, which is shown in Figure 6.19 (right).

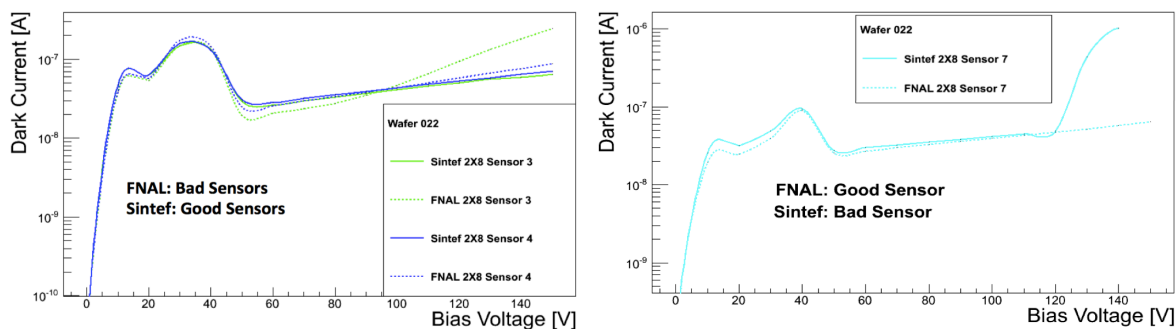


Figure 6.19: Sensors that are not consistent between FNAL and Sintef result. Sensors that are bad for FNAL but good for Sintef are on the left. Sensors that are good for FNAL but bad for Sintef are on the right.

The breakdown voltage comparison is shown in Figure 6.20. The average breakdown voltage of B wafers is about 213 V, while the breakdown voltage of C wafers is 245 V. This suggests that the C wafers are of higher quality than B wafers.

We looked at the CV curves of the production wafers 022, 106, 109, 120 and 139 and saw that the depletion voltage is about 100 V, which is a little bit higher than the expected result. Figure 6.21 shows CV curves for the first sensor of these production wafers.

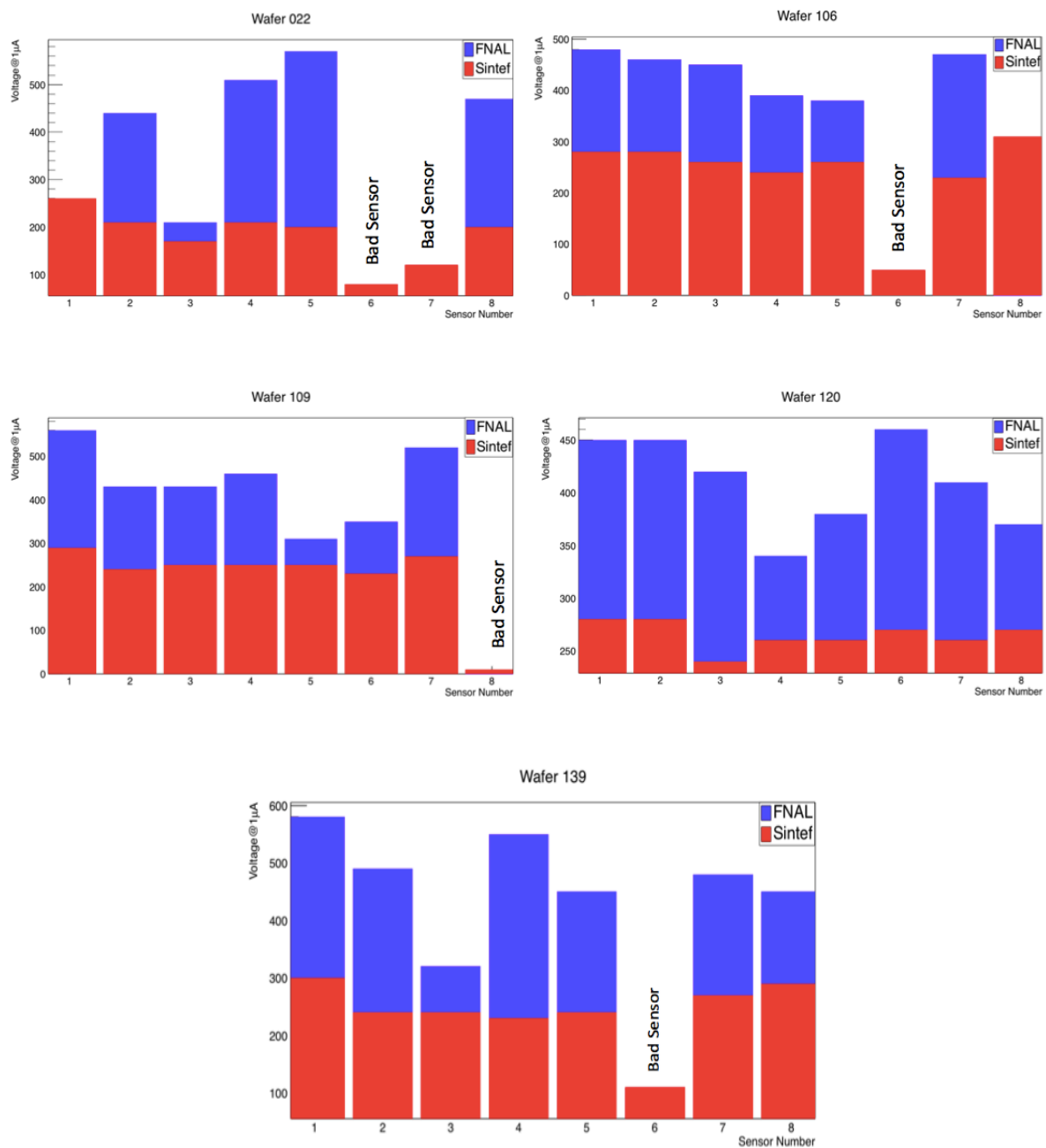


Figure 6.20: Breakdown voltage comparison of production wafers 022, 106, 109, 120 and 139 for FNAL and Sintef.

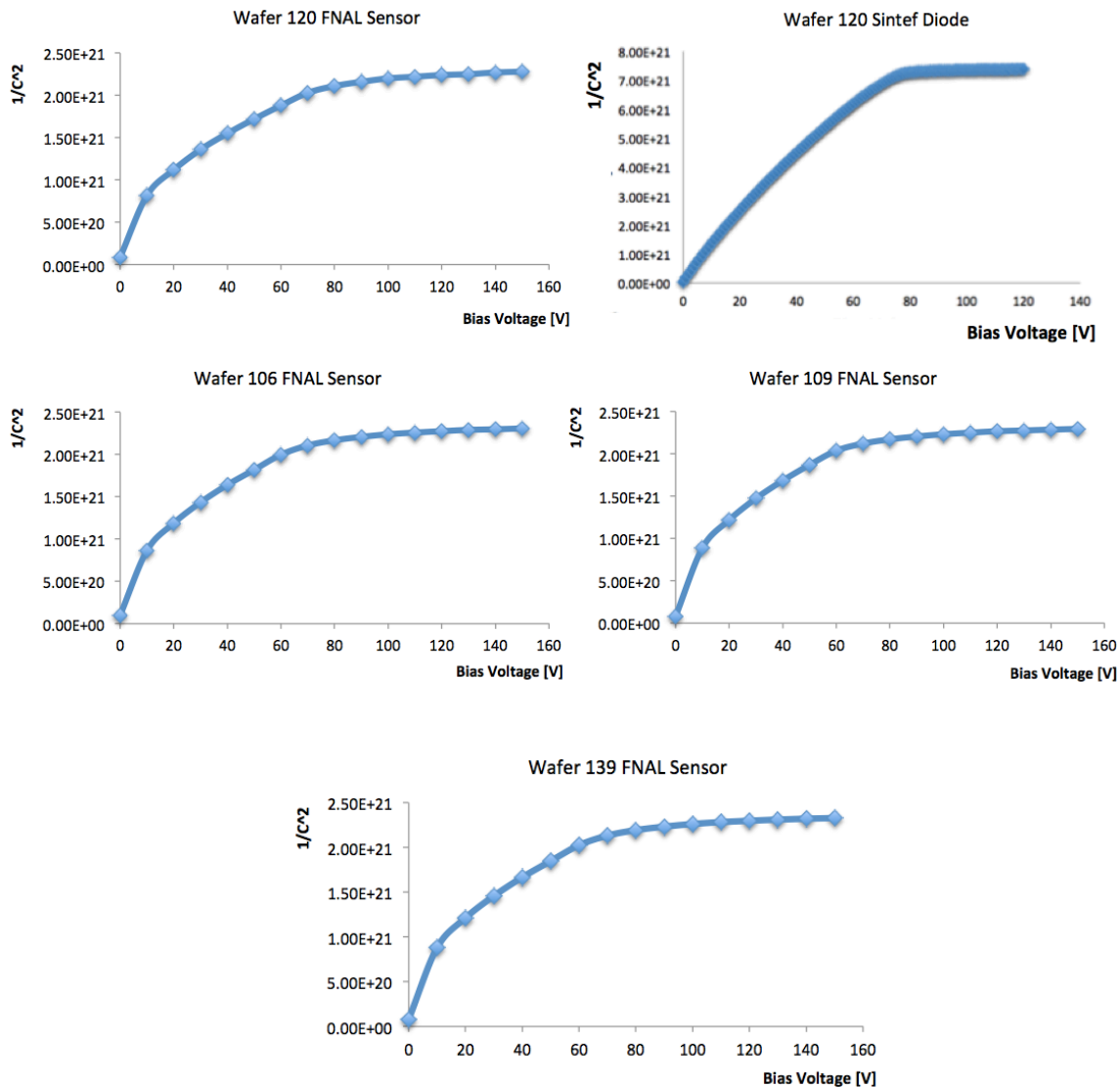


Figure 6.21: CV curves of the production wafers 106, 109, 120 and 139.

According to test results from the second group of five wafers, we found $\frac{3}{39} = 7.7\%$ discrepancy between the FNAL and the Sintef results. The leakage current was 6 - 7 nA/cm² at 150 V.

We received the third shipment of production wafers on June 4th, 2015. In this set of production batch, we received 38 production wafers, 5 B batch and 33 C batch wafers.

As in the previous tests, we chose five production wafers (1 B batch and 4 C batch) and tested them.

IV measurements of all 40 (2x8) sensors were made. We found that almost all sensors passed by our criteria and our results were close to the Sintef results. Figure 6.22 shows IV curves for all good sensors. In this figure, we compare FNAL and Sintef results for all 2x8 sensors. As can be seen, the full depletion voltage is around 80 V and FNAL and Sintef results are in good agreement.

According to this set of production batch, we found one sensor that passed by FNAL criteria, but failed by Sintef criteria. This was sensor 1 of wafer 020. As shown in Figure 6.23, there is a large difference between FNAL and Sintef results. In this figure, the dashed line indicates Sintef results, which are not consistent with the first criteria ($I@100V < 1 \mu A$). However, the FNAL result (solid line) is consistent with our criteria.

We plotted a comparison of the breakdown voltage for this set of production batch. According to this comparison, the average breakdown voltage of C wafers is 245 V and it is 213 V for B wafers. Figure 6.24 shows the comparison of the breakdown voltage for all 2x8 sensors.

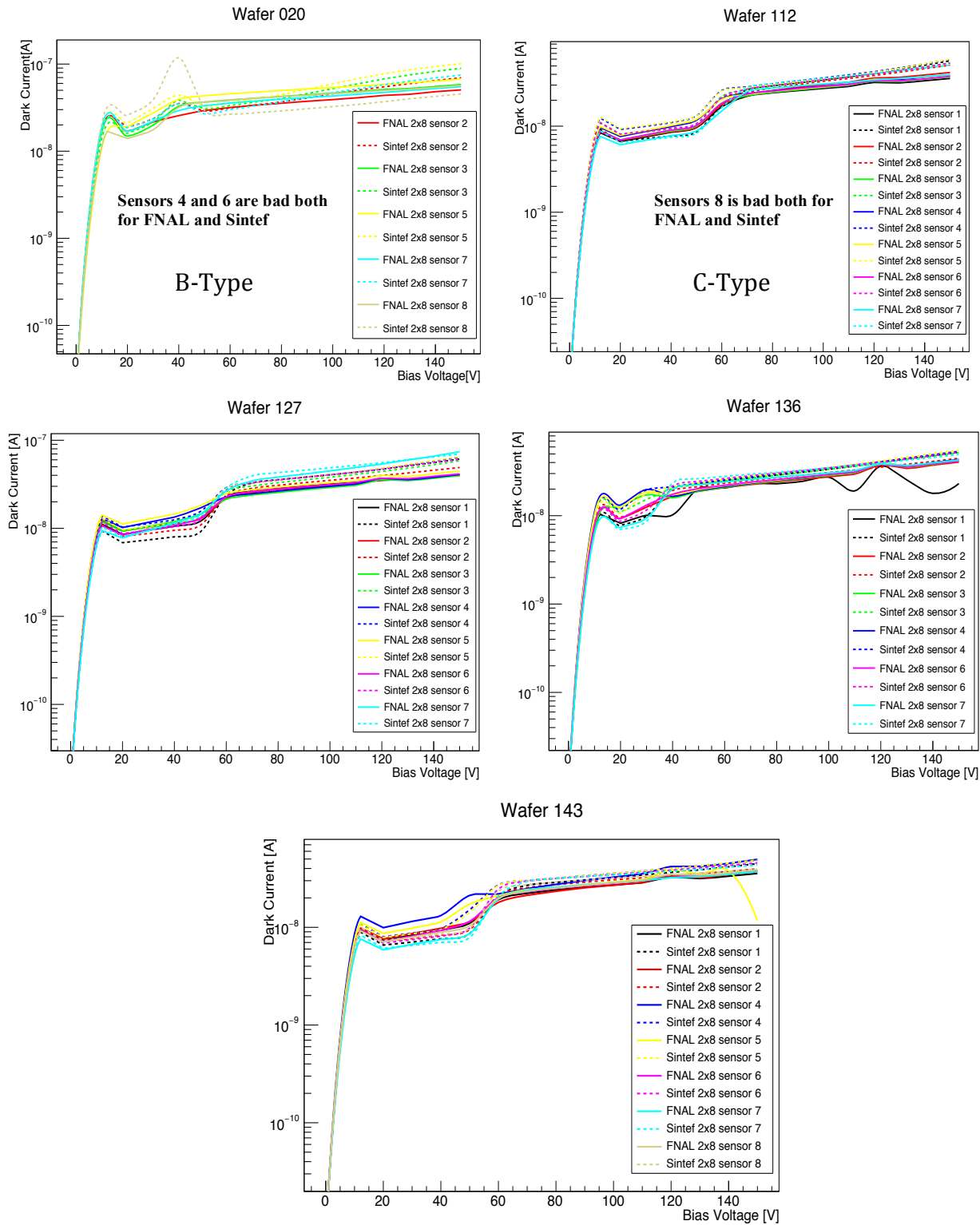


Figure 6.22: IV curves for good sensors of production wafers 020, 112,127, 136 and 143.

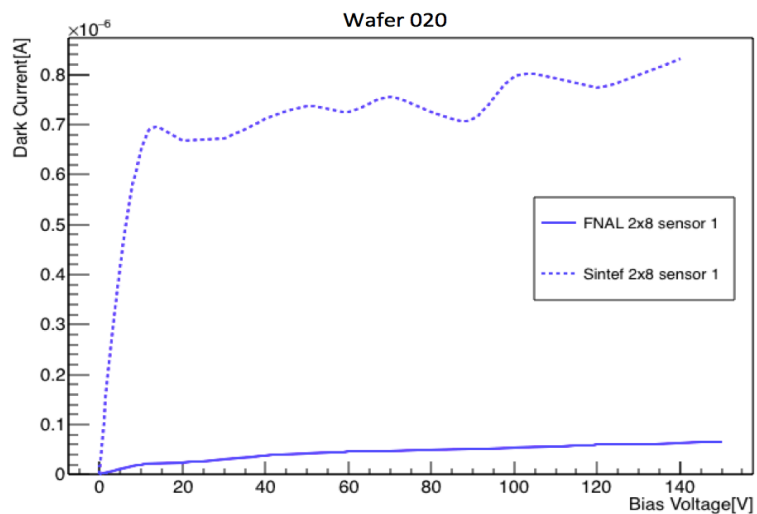


Figure 6.23: IV curve for the sensors that are good for FNAL but bad for Sintef in third production batch.

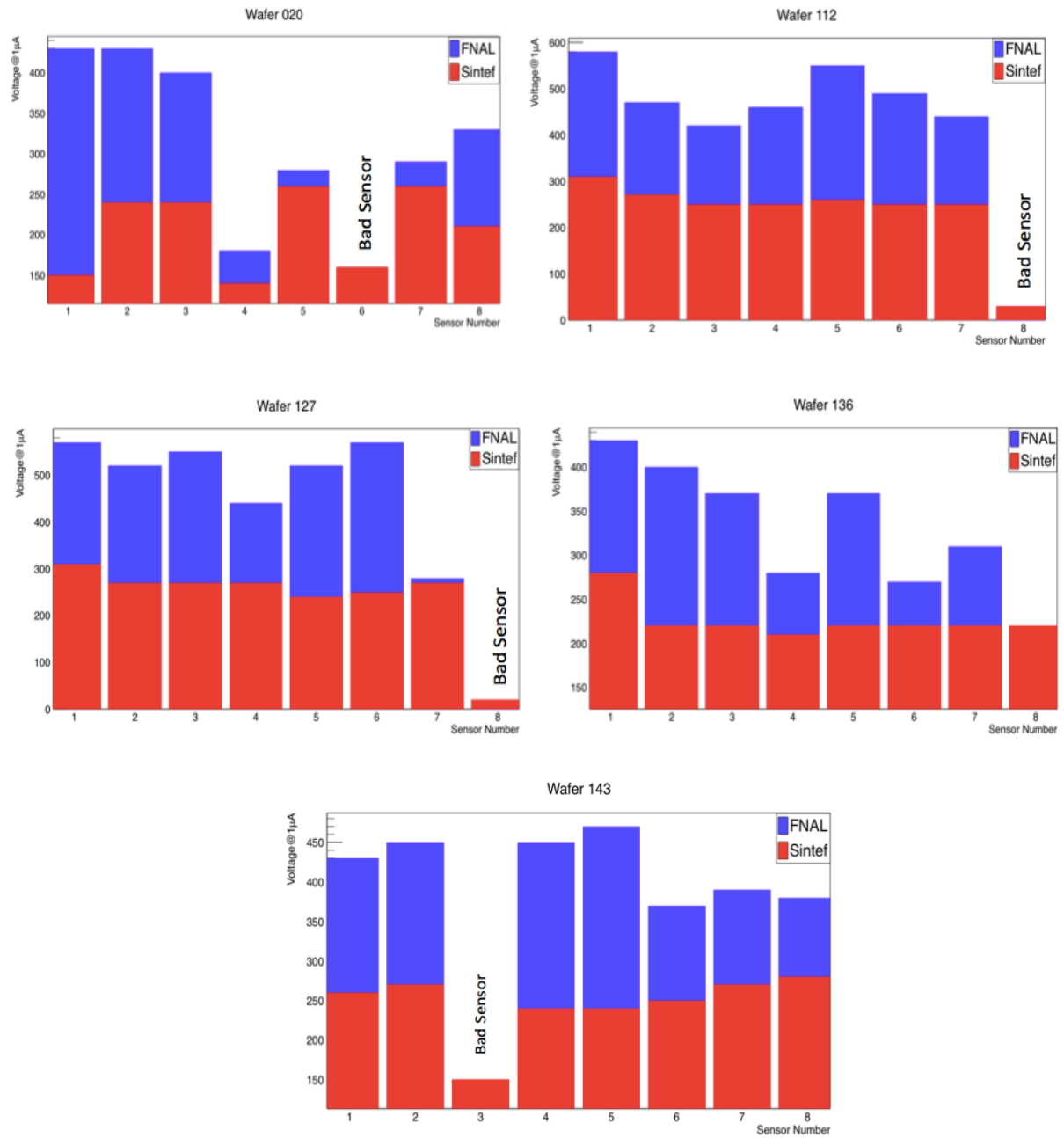


Figure 6.24: Breakdown voltage comparison for production wafers 020, 112, 127, 136 and 143.

For this production batch, we looked at the CV curve of one diode and one sensor for all wafers. Sintef prefers to measure CV on diode (WD_BR_020), but we prefer to measure CV on diode (WD_BL_020). We also looked at the CV curve for the first sensor of each wafer as we did before and we found that the depletion voltage is about 80 V. The CV curves of the diode and sensors are shown in Figure 6.25. The results of this production batch showed a 2.5% discrepancy between the FNAL and Sintef results. The leakage current is 6 - 7 nA/cm² at 150 V.

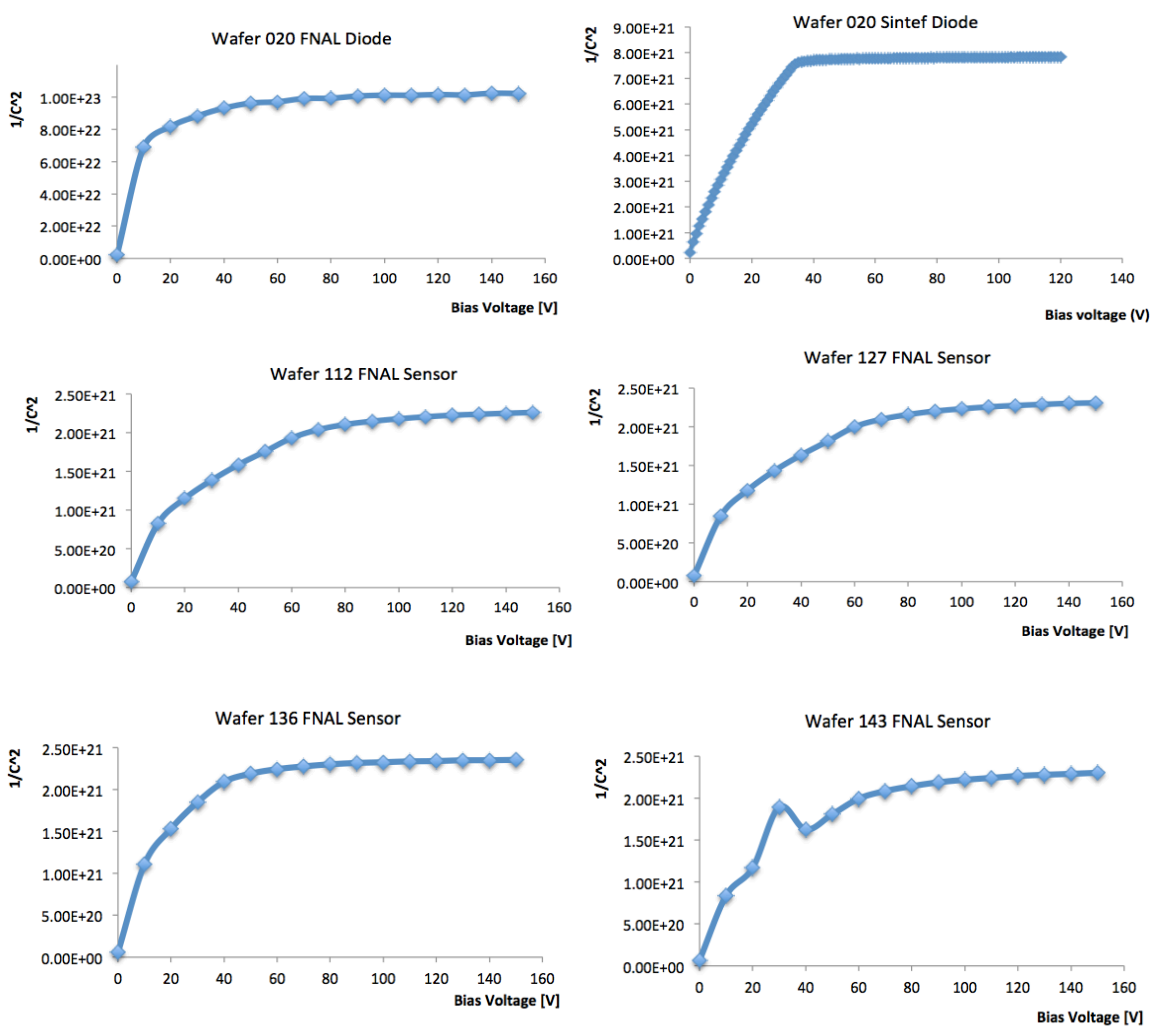


Figure 6.25: CV curves for production wafers 020, 112,127, 136 and 143.

We received the fourth shipment of production wafers on October 27th, 2015. In this set of production batch, we received 37 production wafers, all D type wafers. As in the previous tests, we chose five production wafers and did IV and CV measurements.

IV measurements of all 40 (2x8) sensors were made. We found that most of the sensors were consistent with our criteria and the results were close to Sintef results. Figure 6.26 shows IV curves for all good sensors. In this figure, we compare FNAL and Sintef results for all 2x8 sensors. As shown in the figure, the full depletion voltage is around 65 V.

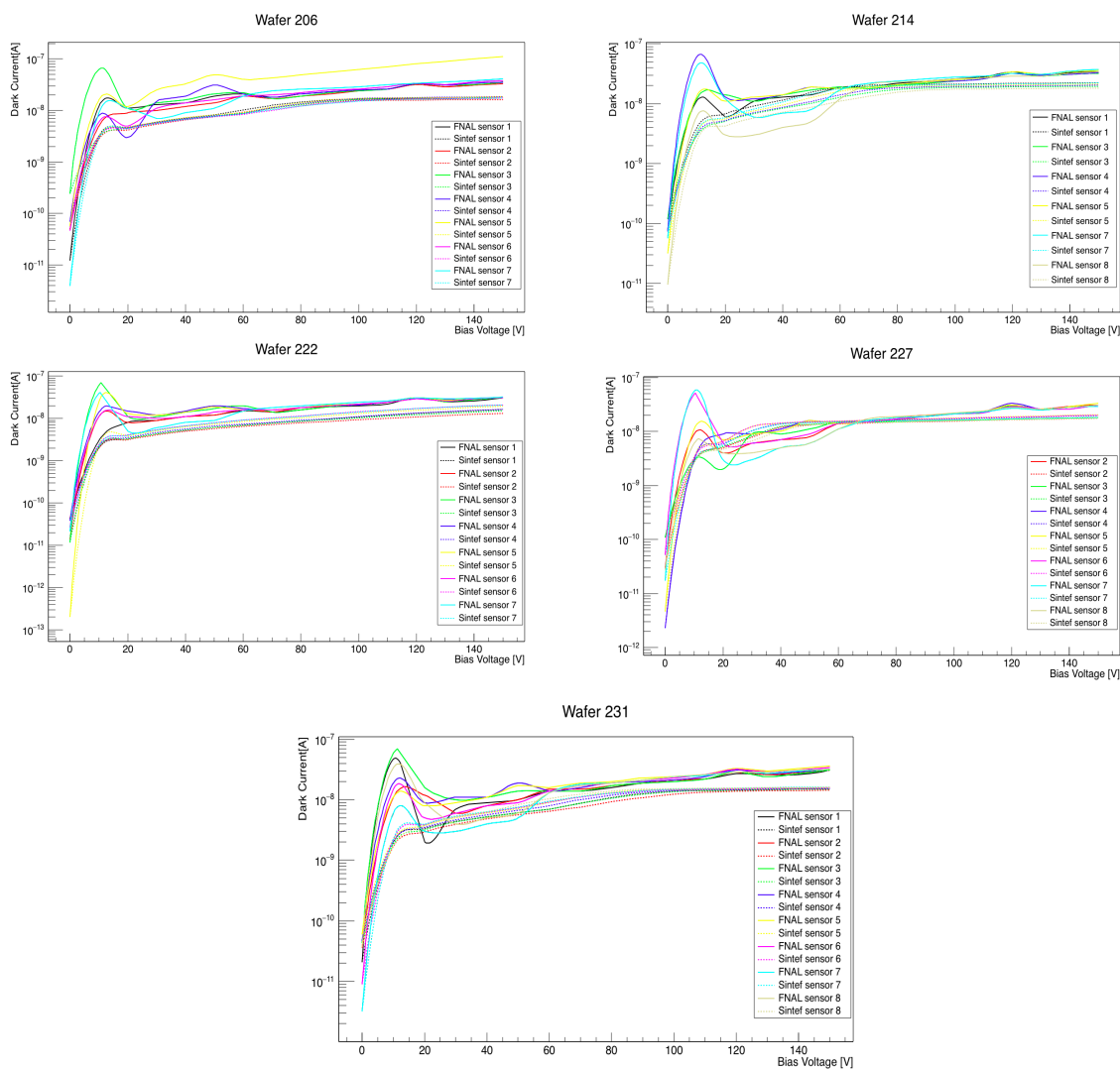


Figure 6.26: Sensors that are good for FNAL and Sintef for the fourth production batch. Wafers 206, 214, 222, 227 and 231.

We found one sensor that is good for Sintef by our criteria, but failed for FNAL criteria. As shown in Figure 6.27, the dark current is within the specification for sensor 8 on wafer 206 (first criteria, $I@100V < 1\mu A$). However, the slope is a little too high, so this is not consistent with the second criteria ($I@150V < 2 * I@100V$). Sintef determined that this sensor is good. Using Sintef data, this sensor is also good by the FNAL rules.

However, using the FNAL data, this sensor fails the FNAL second criteria ($I@150V < 2 * I@100V$).

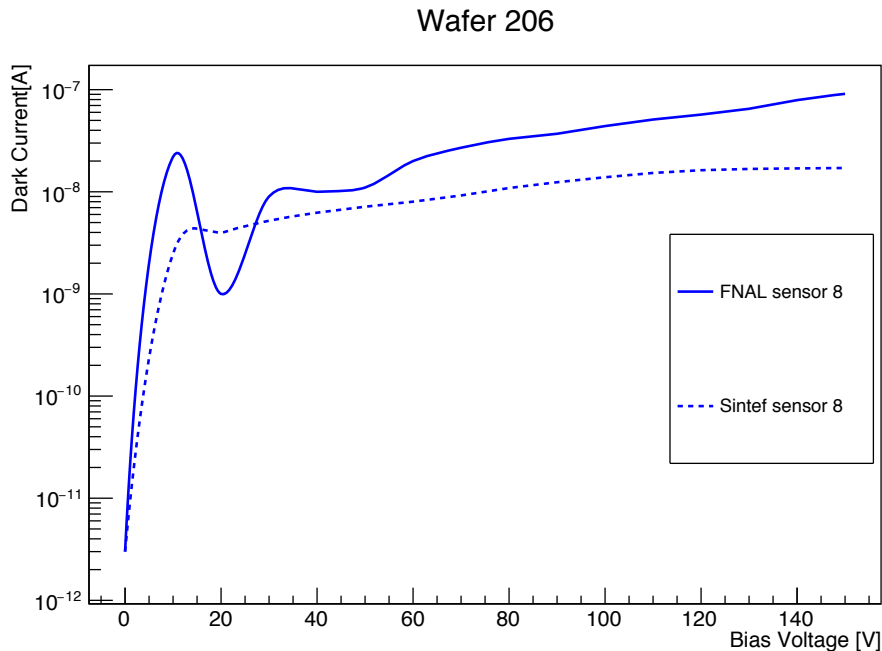


Figure 6.27: Sensors that are good for Sintef but bad for FNAL.

For this production batch we show the sensors that are bad for both Sintef and FNAL in Figure 6.28; sensor 8 on wafer 222, sensor 2 on wafer 214, and sensor 1 on wafer 227 are considered to be bad. For sensor 8 on wafer 222, the dark current is within specification ($I@100V < 1\mu A$). However, the slope is a little too high, so it is not consistent with second criteria ($I@150V < 2 * I@100V$). Wafer 214 sensor 2 is bad for FNAL because it is not consistent with first criteria ($I@100V < 1\mu A$). Wafer 227 sensor 1 is bad for FNAL because it is also not consistent with first criteria ($I@100V < 1\mu A$).

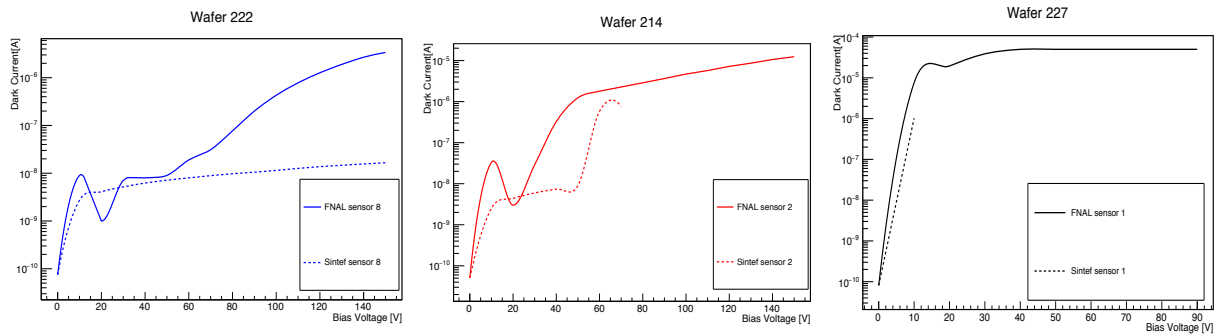


Figure 6.28: Sensors that are bad for both Sintef and FNAL. As can be seen, either they are not consistent with the first criteria ($I@100V < 1\mu A$) or they are not consistent with the second criteria ($I@150V < 2 * I@100V$).

We measured the breakdown voltage comparison for this set of production wafers as we did for the previous shipments. Figure 6.29 shows breakdown voltage comparison for wafers 206, 214, 222, 227 and 231. The FNAL compliance level is 50 nA. However, we used the voltage where the current is first above 1 nA to make a reasonable comparison with Sintef.

As we did for the previous shipments, we looked at the CV curves for this production batch. FNAL uses the first sensor of each wafer for the CV measurement whereas Sintef uses the second diode. Figure 6.30 shows the CV curves of one diode for the Sintef data and CV curves of one sensor for the FNAL data. As can be seen in the figure, the full depletion voltage is about 65 V. In the test of the fourth shipment, we found a 5% discrepancy between Sintef and FNAL results.

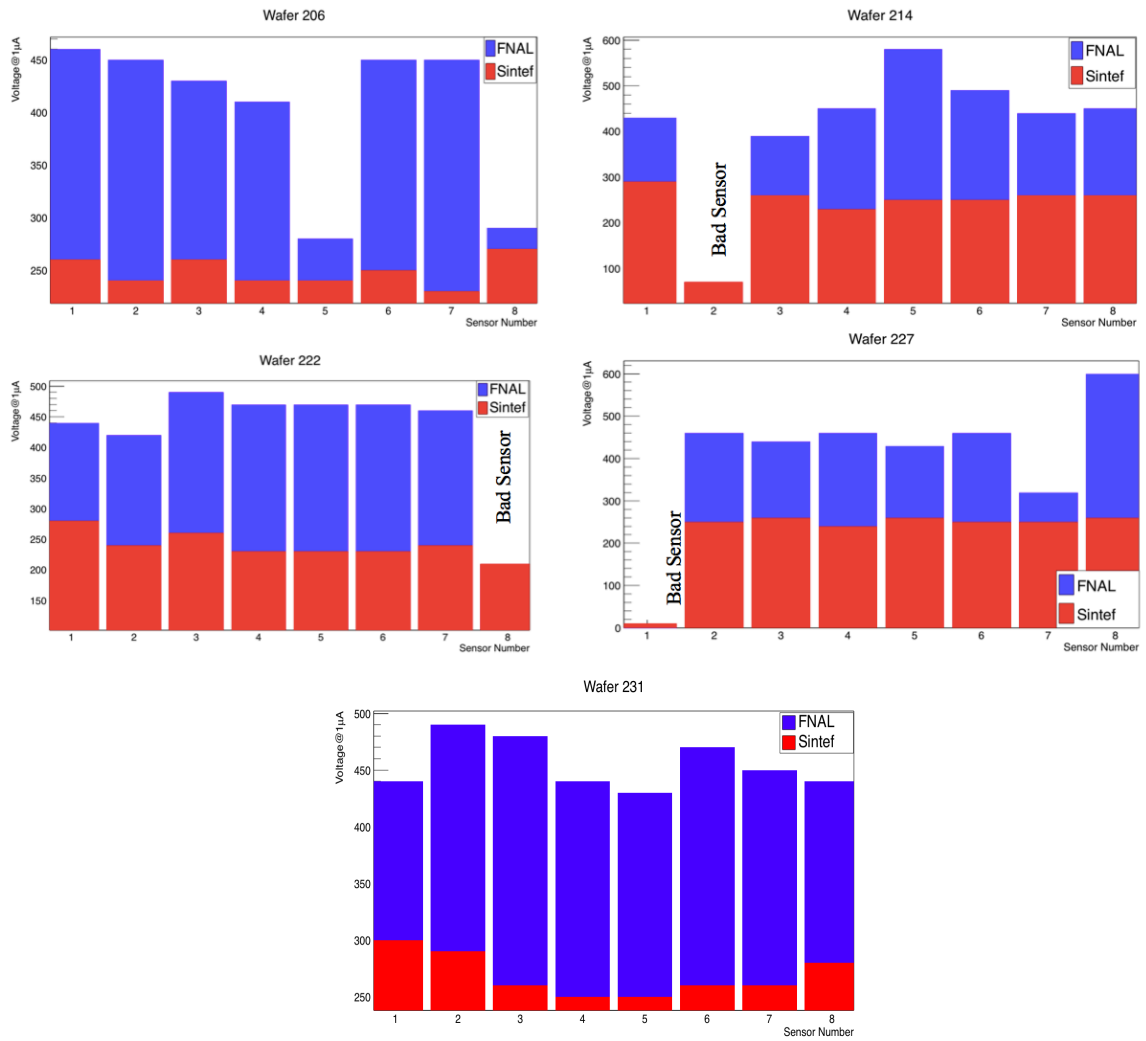


Figure 6.29: Breakdown voltage comparison for production wafers 206, 214, 222, 227 and 231.

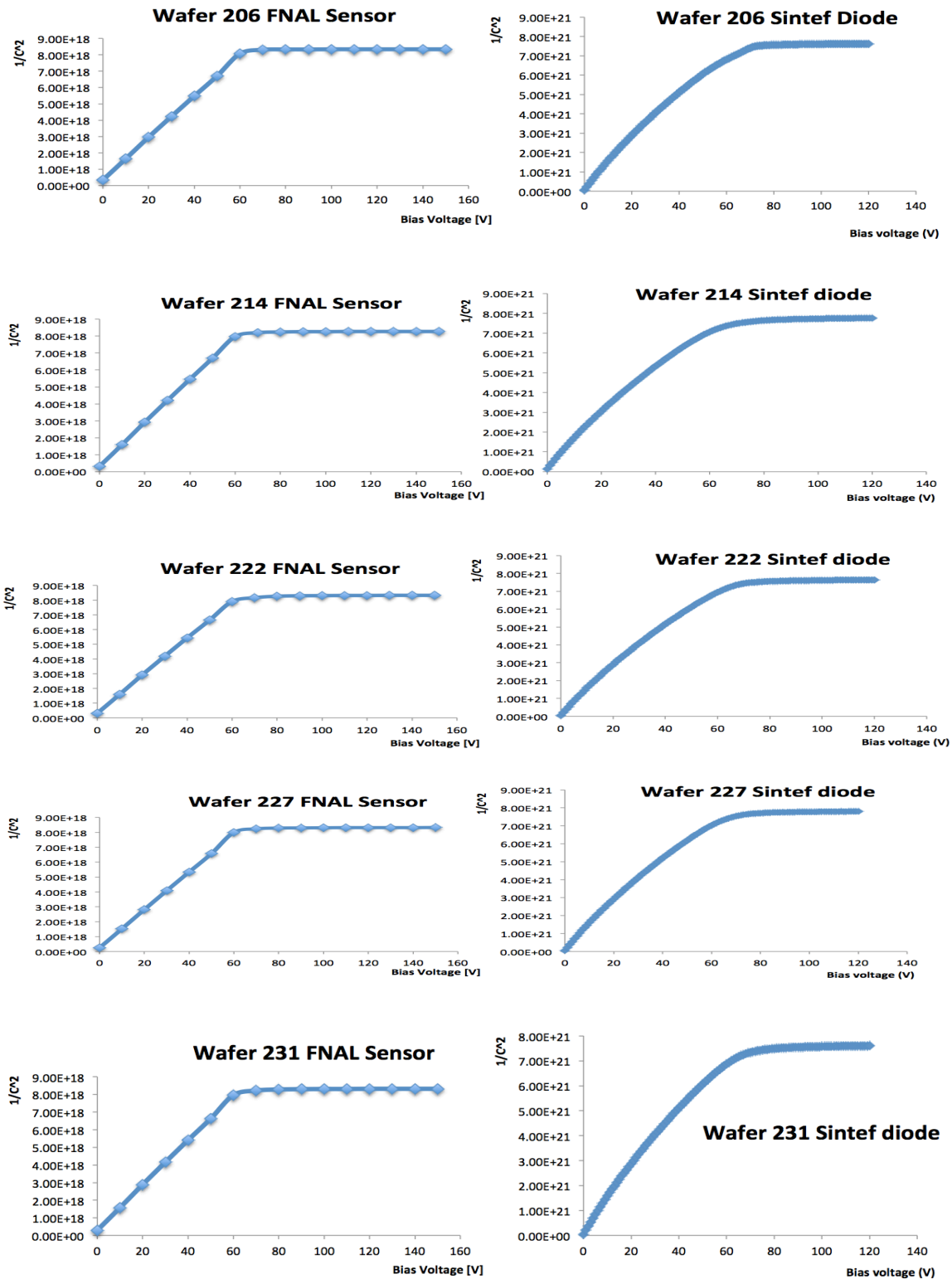


Figure 6.30: CV curves of one diode for the Sintef data and one sensor for the FNAL data.

6.3 Results

For quality control of the production wafers, we received 120 wafers from Sintef and tested all 2x8 sensors on 20 production wafers. We tabulated all of the production batches that we received in Table 6.1. Because the IV and CV curve tests are the most useful way to test the quality of the silicon detectors, we looked at the IV and CV curves of one diode and all 2x8 sensors. In order to assess the quality of a sensor, we used two criteria:

- I at 100 V must be smaller than $1 \mu A$.
- I at 150 V must be smaller than $2xI@100V$

We compared our test results with Sintef results and we did not see much differences. Over 199 sensors, we only found 8 sensors that had some disagreement between Sintef and FNAL (4% discrepancy). The yield is then 96% (191 good sensors). Sintef delivered 120 wafers, 960 sensors in total. There are 914 good sensors for a yield according to Sintef of 95.2%.

Table 6.1: Production batch wafers number that were shipped from Sintef.

	B	C	D	Total
27 March	21			21
29 May	3	21		24
29 May	5	33		38
27 October			37	37
Total	29	54	37	120

The expected depletion voltage for all production wafers is around 65 V. We found a depletion voltage of 65V in the first and fourth production batches, and the first

measurement of the second production batch. However, we found that the depletion voltage was about 100 V in the second measurement of the second production batch and 80 V in the third production batch. Although the last two results were not close to the expected value, they were within an acceptable range. In addition, there may be some unanticipated effects on the results such as needle quality, room temperature, and the chuck's flatness.

In addition to the IV and CV curves, we also looked at the breakdown voltage which is a high reverse voltage that is applied to the material. FNAL uses the voltage at $50 \mu A$ as the breakdown voltage although Sintef uses a voltage at $1 \mu A$ as the breakdown voltage. In order to have a reasonable comparison, we preferred to take the breakdown voltage at $1 \mu A$.

Sintef used a naming convention for the different type of wafers as A, B, C, D. We looked at the breakdown voltages to test the quality of different wafer types. A-type wafers were prototype wafers and we did not include their results in this dissertation since they are not going to be used for the CMS Phase I upgrade. We found that the average breakdown voltage is 213 V for B-type wafers and 245 V for C-type wafers. These results show that C-type wafers have somewhat higher quality than B-type wafers, although both are acceptable for use in the CMS detector.

The production sensors that were tested as good will be used to upgrade the CMS pixel detector in 2016-2017 (Phase I). To separate each sensor in a wafer, the wafers must be diced and good sensors bump bonded to read out charge. Therefore, tested wafers will be sent to RTI for dicing and bump bonding.

CHAPTER 7

R&D STUDY FOR SECONDARY EMISSION IONIZATION CALORIMETRY

7.1 Introduction to Secondary Emission Ionization Calorimetry

Secondary electron emission (SEE) is important for many areas of science and technology. Energetic particles passing through a material cause emission of new electrons from the surface of the material. This process is called secondary emission (SE) [55]. The active material is usually a metal oxide, which has low work function. In this process, a bunch of charged particles strike a metal oxide surface and knock out secondary electrons. In this study, we focus on Photomultiplier Tubes (PMTs) as a source of SE in extremely high radiation environments at particle accelerators.

A PMT is a small detector that is extremely sensitive to light. It consists of a photocathode, several dynodes and an anode. Due to the photoelectric effect, electrons are ejected from the photocathode of the PMT as photons transfer their energies to the active media. After the electrons are ejected, they are accelerated to dynodes where they eject more electrons and the number of electrons is multiplied. PMTs are widely used in many areas. They are used in industry such as in radiometry and optical fields [16]. They are also used in many areas of science such as medical physics, analytical chemistry, and high energy physics. In medical physics, PMTs are used for medical imaging and diagnostic purposes [56]. In analytical chemistry, PMTs are used for environmental measurements and spectrometers [56]. In high energy physics, PMTs are usually used for capturing photons from the particle interactions.

SE ionization calorimetry is a new technique for the energy measurements of energetic particles in very high radiation environments and it is an example of an experimental application of PMTs to develop a new type of detector [57]. Radiation hard detectors are in ever needed at particle accelerators due to increasing instantaneous luminosity and center of mass energy. The goal of this study is to develop a secondary emission ionization module from conventional PMTs. For this purpose, we tested 74 PMTs (Hamamatsu single anode R7761 and multi-anode R5900-00-M16) and characterized these PMTs for use in a secondary emission ionization calorimetry. In SE mode, the photocathode is simply deactivated and the first dynode is used as an active media.

7.2 Characterization of PMT and SE Modes

PMTs were tested at the University of Iowa PMT test station for mapping and response linearity among the anodes of Hamamatsu R5900-00-M16. A 337 nm nitrogen laser with a natural density filter is used. Using a wavelength shifting (WLS) optical fiber, the light is transmitted to the window of the PMT, which is located on computer controlled x-y scanner. The optical fiber doesn't move but only PMT is moved with the x-y scanner to right-left and up-down directions. So the light through the fiber hits a different cell on the surface of the PMT at a time. We used a Keithley-6485 pico-ammeter to read out the current from each anode of the PMTs.

As a first step, we characterized the Hamamatsu single anode R7761 and multi-anode R5900-00-M16 PMTs which we will use in SE mode. We have measured gain and dark current of all the PMTs at different voltages in both SE and PMT modes at the

University of Iowa PMT test station. This test station was built in 2001 to characterize PMTs for the Hadronic Forward (HF) calorimeter at CMS [58]. Over the years, this test station has been used for many purposes such as development of the CMS LED calibration system and upgrade studies for the CMS detector [58].

The tests are done in a light-tight dark box so as not to have ambient light exposure while testing PMTs. Figure 7.1 shows the light-tight box in which the PMTs were tested. This dark box is generally used for dark current, relative gain, and anode and cathode gain measurements. As shown in the figure, the dark box has a patch panel on the side of the box to provide the signal and high voltage cable connections. The experimental setup consists of a light source, a neutral density filter (NDF), an optical sensor, power supply, pico-ammeter, digital scope and a computer. PMTs were located inside the dark box and tested one by one. Then, anode and cathode currents were read out by using a pico-ammeter and GPIB-USB connected computer. All the tests were performed in both SE and conventional PMT modes.

Dark current is a relatively small current produced by a photomultiplier tube in the absence of light. It is measured to quantize the constant background current. Dark current is the background noise so it's an important factor to determine signal to noise ratio of the PMT. This background noise is different than statistical noise that is a systematic variation caused by photoemission or secondary emission process. The definition for the statistical noise is given by the following equation [59]:

$$\Delta I^2 = \frac{Ie}{\tau} \quad (32)$$

where:

- I: Current for cathode.

- e : electron charge.
- τ : Time period of the photons to reach the photo cathode.

At this study, the dark current is measured at various high voltage values for both PMT types and it was below 1 nA for all the PMTs. So, these PMTs are good candidates to work with as in SE and PMT mode.



Figure 7.1: Light-tight box located at the University of Iowa PMT test station.

The gain of a PMT is defined as the ratio of the anode current to cathode current. Basically, it shows how much the signal from photocathode is increased. Since we make two different measurements with two different bases and setups, the light intensity for anode would be different than the light intensity for cathode. So, the light intensity needs

to be taken into account to calculate gains correctly. The gain equation is given by the following [59]:

$$G = \left(\frac{I_a}{I_c}\right)\left(\frac{Li_c}{Li_a}\right) \quad (33)$$

where:

- I_a : Anode current.
- I_c : Cathode current.
- Li_c : Cathode light intensity.
- Li_a : Anode light intensity.

We haven't given the detailed information about the experimental setups for gain and dark current, which can be found in [59].

7.3 Baseboard Operation

David Southwick, an engineer in High Energy Physics (HEP) group at the University of Iowa, designed two different boards to test both Hamamatsu single anode and multi-anode PMTs at different voltages. The voltage dividers located on the board are designed based on the PMT characterization features. The PMTs were powered with negative high voltage because of divider's polarity, which is reversed to have a compatibility with readout electronics. The resistors on the board form a linear voltage divider. In addition to resistors, five capacitors were located on the final dynodes of the board to store charge. In order to decrease the noise from the high voltage supply, another resistor (R_i) was used on HV1, HV2 and GND.

These boards have been made to use in different modes. The designed modes on the board are normal divider operation (conventional PMT mode), and SE modes such as short-circuited between cathode and first dynode and cathode float. For the normal divider operation mode, the potential difference across the dynodes is the same, and it's doubled between the cathode and first dynode. For short-circuiting the cathode to first dynode mode, we simply used a jumper that causes zero potential across the cathode and first dynode. For the cathode float mode, the cathode was separated from the dynodes and the voltage is applied between the first dynode and anode.

Figure 7.2 shows the circuit design of the first board for single anode PMTs. As can be seen in the figure, the board was designed with 20 resistors, 19 dynodes, a cathode and an anode. Figure 7.3 shows a schematic view for the secondary emission board for multi anode R5900-00-M16 PMT. As can be seen, the capacitors have been located on each resistor of the circuit, which is different from Figure 7.2.

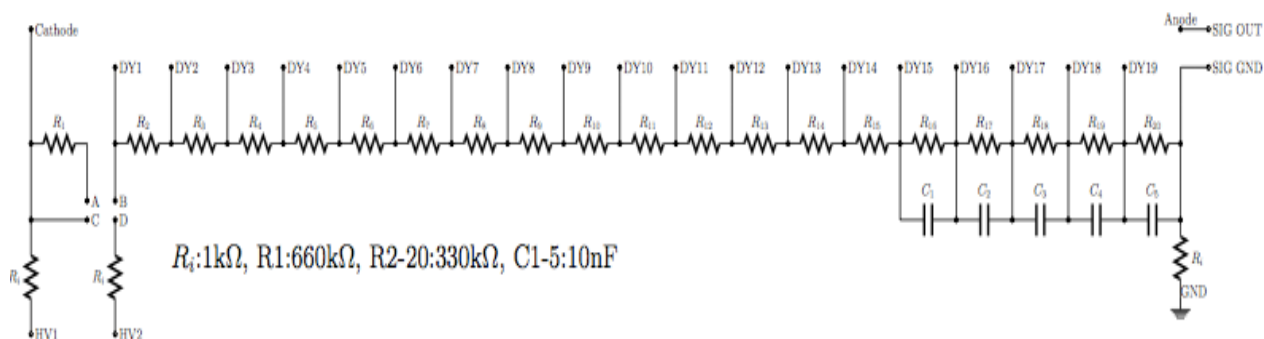


Figure 7.2: Schematic view of the board for Hamamatsu single anode R7761 PMT.

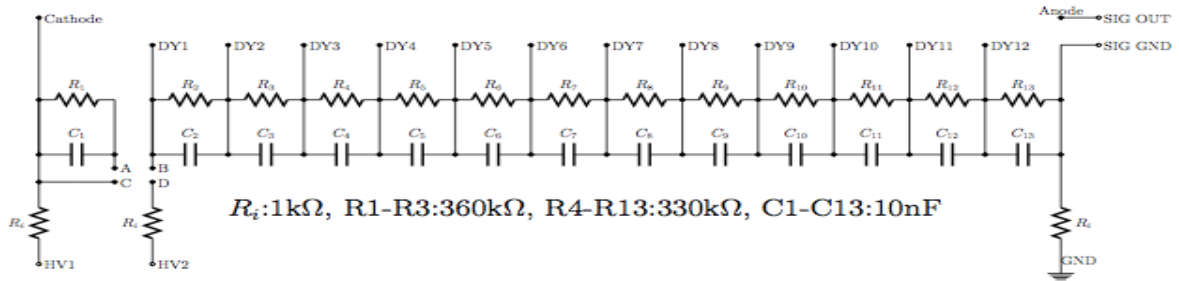


Figure 7.3: Schematic view of the board for Hamamatsu multi anode R5900-00-M16 PMT.

7.4 Results

Two different boards were designed to test both Hamamatsu single anode and multi-anode PMTs at different voltages. These boards were designed for a conventional PMT and SE modes. Using these boards, two types of PMTs (Hamamatsu single anode R7761 and multi anode R5900-00-M16) for both PMT and SE modes were tested and showed comparable performance.

The measured gain values for SE and PMT modes are close as shown in Figures 7.4, 7.5 and 7.6. It means the developed boards and modules for both types of PMTs, Hamamatsu single anode R7761 and multi-anode R5900-00-M16, are operating without any problem. As shown in Tables 7.1 and 7.2, the gain of the PMTs increased $10^{5(6)}$ times, which means the PMTs are good to be used in both modes.

These SE modules (tubes) are operating without any obstacles and they have relatively high gain and low dark current. So, these tubes will be used in a secondary emission calorimeter, which is a novel technique for extremely high-radiation environments. Once the SE calorimeter is designed, the calorimetric measurements will be made with minimum ionizing particle (MIP) and shower particle beams at Fermilab

Test Beam Facility (FTBF) or CERN Test Beam area. In the near future, we would like to take this SE calorimeter one step forward and have a better calorimetric design. In this regard, we are planning to fabricate compact, robust, radiation damage resistant and cost effective SE modules. Simulation studies and material investigations are still underway for this study.

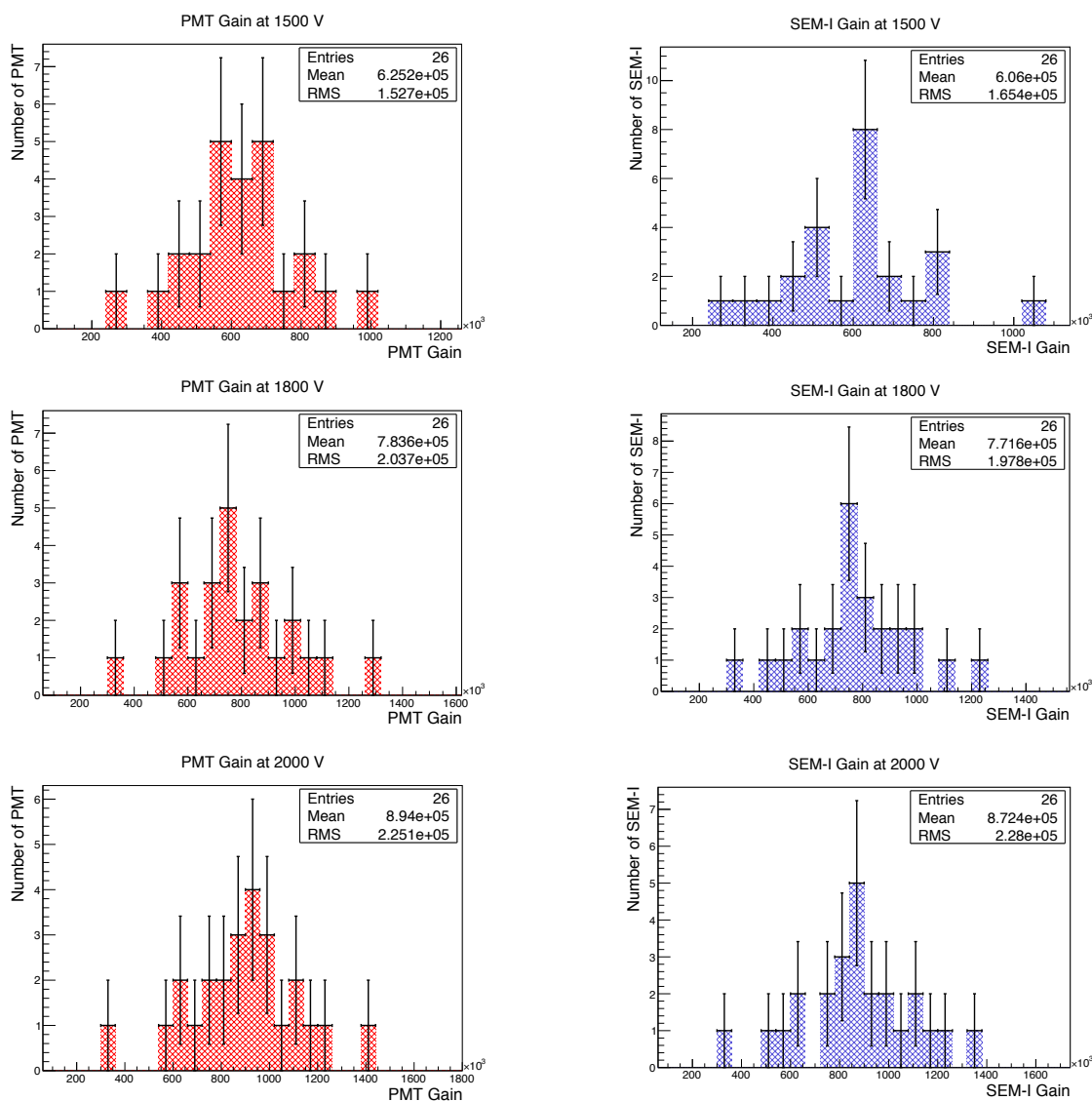


Figure 7.4: PMT and SE (cathode-first dynode shorted mode) gain distributions of Hamamatsu single anode R7761 PMTs at 1500, 1800, 2000 V.

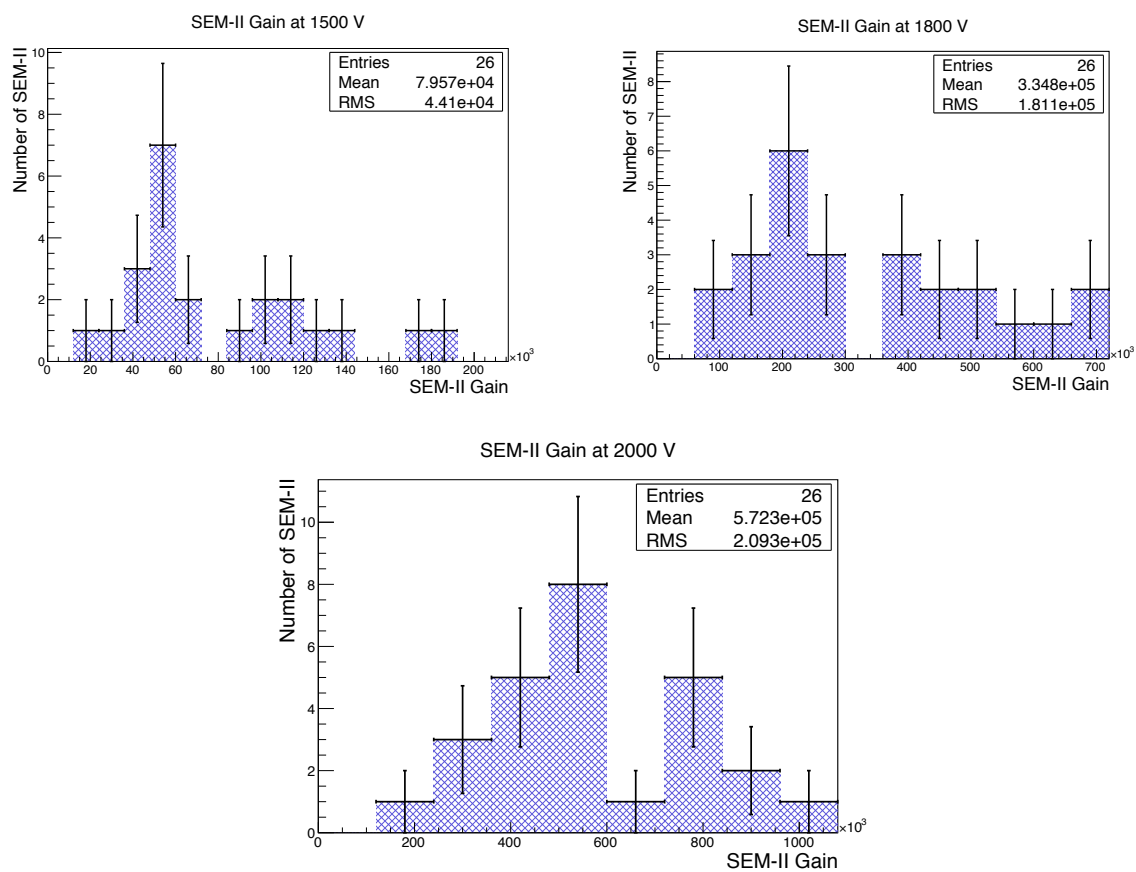


Figure 7.5: SE (cathode deactivated mode) gain distributions of Hamamatsu single anode R7761 PMTs at 1500, 1800, 2000 V.

Table 7.1: Mean and RMS gain values of R7761 PMTs in different modes.

	1500 V		1800 V		2000 V	
Gain ($\times 10^5$)	Mean	RMS	Mean	RMS	Mean	RMS
PMT Mode	6.25	1.53	7.84	2.04	8.94	2.25
SE-I Mode	6.06	1.65	7.72	1.98	8.72	2.28
SE-II Mode	0.80	0.44	3.35	1.81	5.72	2.09

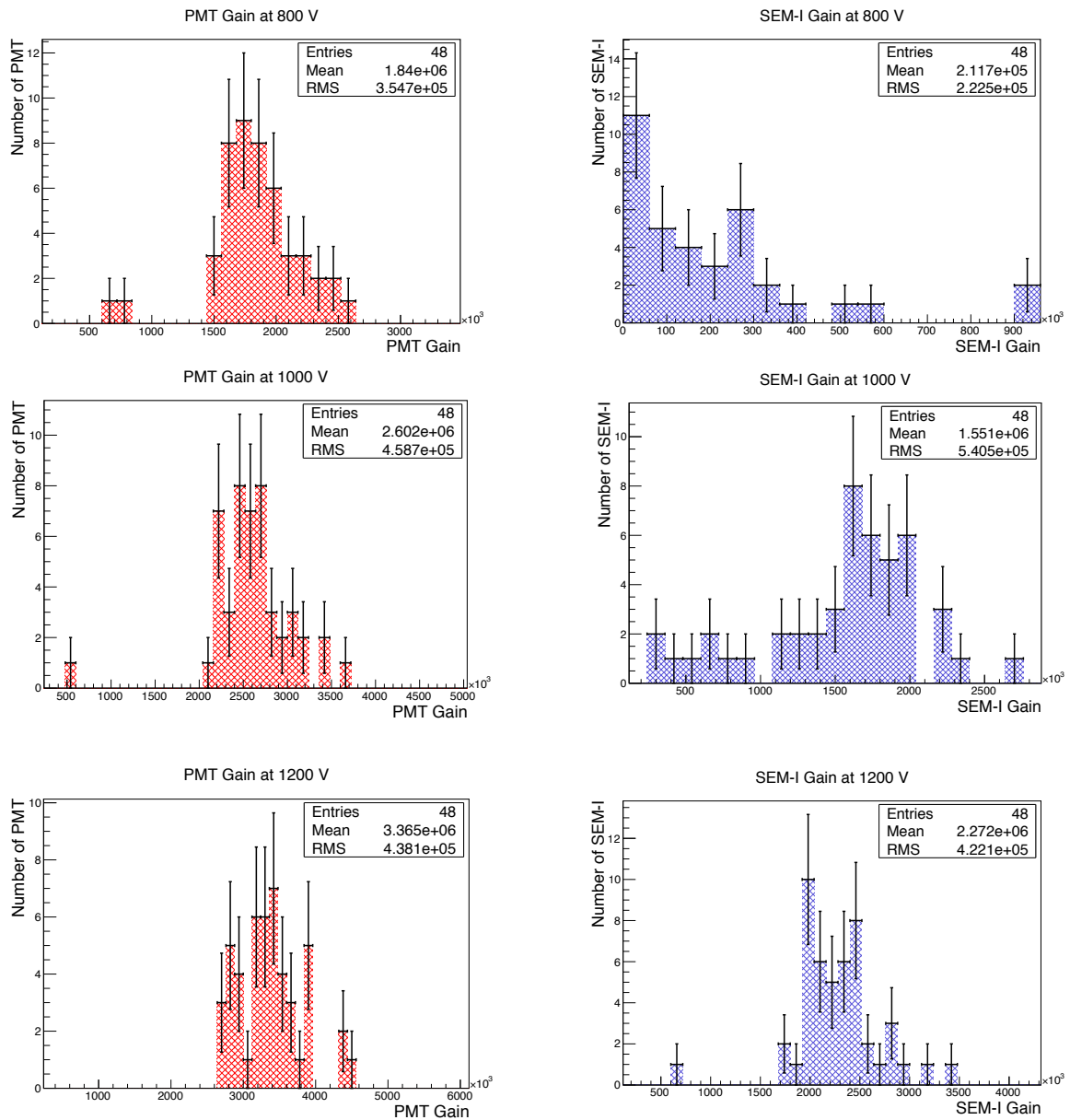


Figure 7.6: PMT and SE (cathode-first dynode shorted mode) gain distributions of Hamamatsu multi-anode R5900-00-M16 PMTs at 800, 1000, 1200 V.

Table 7.2: Mean and RMS gain values of R5900-00-M16 PMTs in different modes.

	800 V		1000 V		1200 V	
Gain ($\times 10^5$)	Mean	RMS	Mean	RMS	Mean	RMS
PMT Mode	18.4	3.55	26.02	4.59	33.7	4.38
SE Mode	2.12	2.23	15.51	5.41	22.72	4.22

CHAPTER 8

CONCLUSION

The analysis showed the result of measurement and cross section for simultaneously produced $Y(1S)$ and J/ψ mesons using the data collected by the CMS detector with an integrated luminosity of 20 fb^{-1} . Both mesons were fully reconstructed in their final states, $\mu^+\mu^-$. Due to the cylindrical shape of the CMS detector, an acceptance region was defined as $|y| < 2.0$, and transverse momentum requirements were varied for different rapidity regions for muons. Minimum transverse momentum on the J/ψ was varied from 4 GeV/c to 6.5 GeV/c at different rapidity ranges.

To estimate the signal acceptance, the Monte Carlo samples were generated using a Pythia6 Monte Carlo generator (particle gun) for muons, $Y(nS)$ and J/ψ . The shape of $Y(nS)$ and J/ψ were determined from the Monte Carlo samples. A two-dimensional extended maximum likelihood fit was used on the data to extract the number of $Y(1S) + J/\psi$ events. To understand the possibility of displaced J/ψ events from B decay, a three-dimensional extended maximum likelihood fit was used on the data.

The evidence for simultaneously produced $Y(1S)$ and J/ψ mesons was found for the first time with a statistical significance equal to 4.4σ . An event-by-event data embedding method was used for acceptance and efficiency corrections and the numerical values of corrected acceptance and efficiency were used to calculate the cross section. Assuming $Y(1S)$ and J/ψ candidates are un-polarized, the measured total cross section of simultaneously produced $Y(1S)$ and J/ψ mesons in the defined fiducial region ($|y| < 2.0$) is found to be $\sigma = 16.5 \pm 3.6(stat) \pm 2.6(syst)$ pb. The next steps for this analysis:

Tag and Probe study to cross check muon efficiency, creating DPS and SPS models for $Y(1S) + J/\psi$ at CMS and calculating differential cross section in bins of $|\Delta y|$.

For upgrade studies of the CMS pixel detector, IV and CV measurements have been performed for 199 production sensors, and the measured results were compared with Sintef results. There are 191 good sensors over 199 sensors giving a yield for good sensors of 96%. Sintef results showed that there are 914 good sensors over 960 sensors and the yield for good sensors is 95.2%. Comparing our results with Sintef results, we did not see much difference. Next, the production wafers will be shipped to RTI for metallization and bump bonding. The good sensors will be used in the CMS Pixel detector for period of accelerator operations (2016-2017).

For SE study, the gain values were measured for 74 PMTs at the University of Iowa High Energy Physics PMT Test Station, and measured gain results showed that the developed boards and modules for both types of PMTs, Hamamatsu single anode R7761 and multi-anode R5900-00-M16, are operating without any problem. Next, we plan to do test beam studies such as minimum ionizing particle tests and shower particle tests with the developed modules at the Fermilab Test Beam Facility (FTBF) or CERN H2 Test Beam area. We are planning to fabricate compact, robust, radiation damage resistant and cost-effective SE modules. Simulation studies and material investigations are still underway for this study.

REFERENCES

- [1] N.Parashar on Behalf of CMS Collaboration, CMS Pixel Detector Upgrade, “*Proceedings of the DPF-2011 Conference, Providence, RI*”, August 8-13, 2011.
- [2] NA3 Collaboration “Evidence for $\psi\psi$ Production in π Interactions at 150-GeV/c and 280-GeV/c”, *Phys. Lett.* **B114** (1982) 457, doi:10.1016/0370-2693(82)900910.
- [3] CERN, “LHC Machine”, *JINST 3 S08001*, 2008.
- [4] CMS Technical Design Report, “*The CMS Experiment at LCH*”, (2012).
- [5] CMS Collaboration, “The performance of the CMS muon detector in proton-proton collisions at $\sqrt{s} = 7$ TeV at the LHC” *JINST 8 (2013) P11002*, doi:10.1088/17480221/8/11/P11002, arXiv:1306.6905.
- [6] C. Wulz for CMS Collaboration, “*Study of the Inclusive Beauty Production at CMS and Construction and Commissioning of the CMS Pixel Barrel Detector*”, 2012. ISBN:978-642-24561-9.
- [7] S. Abdullin *et al.*, “Design, performance, and calibration of CMS hadron-barrel calorimeter wedges”, *Eur. Phys. J. C* **55 (2008) 159171**. Doi:10.1140/epic/s10052-008-0573-y.
- [8] CMS Collaboration, Detector Performance and Software-Physics Technical Design Report, CERN/LHCC 2006-001, 2006.
- [9] A. Penzo and Y. Onel (for the CMS collaboration), “The CMS-HF quartz fiber calorimeter”, *Journal of Physics*, Vol. 160, 2009.
- [10] S. Chatchyan *et al.* [CMS Collaboration], Performance of the CMS Level-1 Trigger during Commissioning with Cosmic Ray Muons, *JINST 5 (2010) T03002*.
- [11] CMS Collaboration, *Detector Performance and Software: Technical Design Report*, CERN/LHCC 2006-001, CMS TDR 8.1, (2 February 2006).
- [12] L. Taylor, “Cathode Strip Chambers”, 23 November 2011. [Online] Available: <http://cms.web.cern.ch/news/cathode-strip-chambers>.
- [13] L. Taylor, “Resistive Plate Chambers”, 23 November 2011. [Online] Available: <http://cms.web.cern.ch/news/resistive-plate-chambers>.
- [14] K. Klein, The CMS Project Strip Tracker-Overview and Status, “*Proceedings of Science*”, July 21st -27th 2005, arXiv:physics/0610259.

- [15] CMS: The Tracker Project Technical Design Report, CERN/LHCC, CMS TDR, 15 April 1998.
- [16] G. Bauer *et al.*, “The data-acquisition system of the CMS experiment at the LHC”, *Phys. Conf. Ser.* **331** (2011) 022021, doi:10.1088/1742-6596/331/2/022021.
- [17] D. Trocino, “The CMS High Level Trigger”, *J. Phys. Conf. Ser.* **513** (2014) 012036, doi:10.1088/1742-6596/513/1/012036.
- [18] C. Foudas, “The CMS Level-1 Trigger at LHC and Super-LHC”, in *Proceedings, 34th International Conference on High Energy Physics (ICHEP 2008)*. 2008 arXiv: 0810.4133.
- [19] D. Griffiths, “Introduction to Elementary Particles”, Wiley-VCH, 2009.
- [20] D0 Collaboration, “Search for Neutral Higgs Boson Decaying to Tau Pairs in ppbar Collisions at $\sqrt{s} = 1.96 \text{ TeV}$ ”, *Physical Review Letters*, vol 97, no. 12, pp.121802-121809, 2006.
- [21] CERN, “New results indicate that new particle is a Higgs boson”, CERN Accelerating Science, 14 March 2013. [Online]. Available <http://home.web.cern.ch/about/updates/2013/03/new-results-indicate-newparticle-higgs-boson>.
- [22] N. Filipovic on behalf of the CMS collaboration, “Bottomonium measurements in pp, pPb, PbPb using the CMS detector”, *Journal of Physics* 612 (2015) 012021, doi:10.1088/1742-6596/612/2/012021.
- [23] CMS Collaboration, “Observation of sequential Upsilon suppression in PbPb collisions”, *Phys. Rev. Lett.* **109** (2012) 222301, doi:10.1103/PhysRevLett.109.222301, arXiv:1208.2826.
- [24] J. J. Aubert *et al.*, *Phys. Rev. Lett.* 33 (1974) 1404.
- [25] T. Dahms, “Charmonium production measured in PbPb and pp collisions by CMS”, *J. Phys.* **G38** (2011) 124105, doi:10.1088/0954-3899/38/12/124105, arXiv:1107.0252.
- [26] CMS Collaboration, Measurement of charmonium production in PbPb collisions at $\sqrt{S_{NN}} = 2.76 \text{ TeV}$ with CMS”, *Nucl. Phys. A910-911 (2013) 215-218*, doi: 10.1016/j.nuclphysa.2012.12.067, arXiv: 1209.1084.
- [27] CMS Collaboration, “Search for a new bottomonium state decaying to $\Upsilon(1S)\pi^+\pi^-$ in pp collisions at $\sqrt{s} = 8 \text{ TeV}$ ”, *Phys. Lett B* 727 (2013) 57-76, doi: 10.1016/j.physletb.2013.10.016, arXiv: 1309.0250.

- [28] CMS Collaboration, “Charmonia in pp and PbPb with CMS”, *Nucl. Phys.* **A931** (2014) 586-590, doi:10.1016/j.nuclphysa.2014.09.012.
- [29] A. Manohar and W. Waalewijn, “What is Double Parton Scattering?”, *Phys. Lett.* **B713** (2012) 196-201, doi:10.1016/j.physletb.2012.05.044, arXiv:1202.5034.
- [30] E. Cazaroto *et al.*, “Heavy quark production and gluon saturation in double parton scattering at the LHC”, *Phys. Rev.* **D88** (2013), no. 3, 034005, doi:10.1103/PhysRevD.88.034005, arXiv:1306.4169.
- [31] A. Novoselov, “Double parton scattering as a source of quarkonia pairs in LHCb”, arXiv:1106.2184.
- [32] A. Likhoded *et al.*, “Simultaneous production of charmonium and bottomonium mesons at LHC”, arXiv:1503.00246.
- [33] C. Kom *et al.*, “Pair Production of Jpsi as a Probe Double Parton Scattering at LHCb”, *Phys. Rev. Lett.* **107** (2011) 082001, doi: 10.1103/PhysRevLett.107.082002, arXiv: 1105.4186.
- [34] P. Ko *et al.*, “Inclusive double-quarkonium production at the Large Hadron Collider”, *JHEP* **1101** (2011) 070, doi: 10.1007/JHEP01(2011)070, arXiv: 1007.3095.
- [35] CMS Collaboration, “Measurement of the Prompt Double Jpsi Production Cross Section in pp Collisions at $\sqrt{s} = 7 \text{ TeV}$ ”, CMS-AN-2012-22.
- [36] CMS Collaboration, “Measurement of prompt J/ψ pair production in pp collisions at $\sqrt{s} = 7 \text{ TeV}$ ”, *JHEP* **09** (2014) 094, doi:10.1007/JHEP09(2014)094, arXiv:1406.0484.
- [37] LHCb Collaboration, “Observation of J/ψ pair production in pp collisions at $\sqrt{s} = 7 \text{ TeV}$ ”, *Phys. Lett.* **B707** (2012) 52-59, doi:10.1016/j.physletb.2011.12.015, arXiv:1109.0963.
- [38] R. Brun *et al.*, “Root AN Object-Oriented Data Analysis Framework”, June 2008. Web. 31 March 2016. [Online]. Available: ftp://root.cern.ch/root/doc/Users_Guide_5_20.pdf.
- [39] W. Verkerke and D. Kirkby, “The RooFit toolkit for data modeling”, *eConf* **C0303241** (2003) MOLT007, arXiv:physics/0306116. [186(2003)].
- [40] C. Walck, “Hand book on Statistical distributions for experimentalists”, University of Stockholm, 10 September 2007. [Online}. Available: <http://www.stat.rice.edu/~dobelman/textfiles/DistributionsHandbook.pdf>.

- [41] S. Das, “A simple alternative to the Crystal Ball function”, arXiv:1603.08591.
- [42] Particle Data Group Collaboration, “Review of Particle Physics (RPP)”, *Phys. Rev. D* **86** (2012) 010001, doi:10.1103/PhysRevD.86.010001.
- [43] S. Wilks, “The large-sample distribution of the likelihood ratio for testing composite hypotheses, *Ann. Math. Statist.*” 9(1938) 60-2.
- [44] CMS Collaboration, “CMS Luminosity Based on Pixel Cluster Counting-Summer 2013 Update”, Technical Report CMS-PAS-LUM-13-001, CERN, Geneva 2013.
- [45] CMS Collaboration, “Measurement of the prompt J/ψ and $\psi(2S)$ polarizations in pp collisions $\sqrt{s} = 7 \text{ TeV}$ ”, *Phys. Lett.* **B727** (2013) 381-402, doi:10.1016/j.physletb.110.081802, arXiv:1209.2922.
- [46] CMS Collaboration, “Measurement of the $Y(1S)$, $Y(2S)$ and $Y(3S)$ polarizations in pp collisions at $\sqrt{s} = 7 \text{ TeV}$ ”, *Phys. Rev. Lett.* 110(2013), no:8081802. doi: 10.1103/PhysRevLett.110.081802, arXiv:1209.2922.
- [47] CMS Collaboration, “Measurement of the $Y(1S)$, $Y(2S)$ and $Y(3S)$ cross sections in pp collisions at $\sqrt{s} = 7 \text{ TeV}$ ”, *Phys. Lett.* **B727** (2013) 101-125, doi: 10.1016/j.physletb.2013.10.033, arXiv:1303.5900.
- [48] CMS Collaboration, “Prompt and non-prompt J/ψ production in pp collisions at $\sqrt{s} = 7 \text{ TeV}$ ”, *Eur. Phys. J.* **C71** (2011) 1575, doi:10.1140/epjc/s10052-011-1575-8, arXiv:1011.4193.
- [49] D. d’Enterria and A. Snigirev, “Pair production of quarkonia and electroweak bosons from double parton scatterings in nuclear collisions at the LHC”, *Nucl Phys.* **A931** (2014) 303-308, doi:10.1016/j.nuclphysa.2014.09.089, arXiv:1408.5172.
- [50] M. Grundmann, “The Physics of Semiconductors”, Second Edition, Springer, 11 November 2010.
- [51] M. Krammer, “Silicon Detectors”, Institute of High Energy Physics, Vienna, Austria. November 2010. [Online]. Available: http://www.hephy.at/fileadmin/user_upload/Halbleiterdetektoren.pdf.
- [52] T. Rohe, “Sensor Concepts for Pixel Detectors in High Energy Physics”, Paul Scherrer Institute, Switzerland. 2 April 2016. [Online]. Available: <http://www.slac.stanford.edu/econf/C020909/trpaper.pdf>.

- [53] M. Vignali, “Silicon Sensors for the Upgrades of the CMS Pixel Detector”, Ph.D. Thesis, University of Hamburg, Hamburg, 2015. [Online]. Available: <https://inspirehep.net/record/1409615/files/thesis.pdf>.
- [54] A. Dorokhov, “Performance of Radiation Hard Pixel Sensors for the CMS Experiment”, Ph.D. Thesis, University of Zurich, Zurich, 2005. [Online]. Available: <http://unizh.web.cern.ch/unizh/Publications/Articles/Dorokhov.pdf>.
- [55] J. J Scholtz *et al.*, Philips J. Res 50, 375-389, 1996.
- [56] Hamamatsu, “*Photo Multiplier Tubes*”, [Online] Available: https://www.hamamatsu.com/resources/pdf/etd/PMT_handbook_v3aE.pdf.
- [57] D. Winn and Y. Onel, Secondary Emission Calorimeter Sensor Development, “*Journal of Physics Conference*” 404 (2012) 012021. doi:10.1088/1742-6596/404/1/012021.
- [58] U. Akgun *et al.*, Characterization of 1800 Hamamatsu R7600-M4 PMTs for CMS HF Calorimeter upgrade, *JINST* 9, T06005 (2014).
- [59] E.Tiras, “Characterization of 900 four-anode photomultiplier tubes for use in 2013 hadronic forward calorimeter upgrade”, M.S Thesis, University of Iowa, 2013.[Online].Available:<http://ir.uiowa.edu/cgi/viewcontent.cgi?article=3337&context=etd>.